The co-evolution of life and the nitrogen cycle on the early Earth

Matthew C. Koehler

A dissertation

submitted in partial fulfillment of the

requirements for the degree of

Doctor of Philosophy

University of Washington

2018

Reading Committee:

Roger Buick, Ph.D., Chair

David Catling, Ph.D.

Eric Steig, Ph.D.

Program Authorized to Offer Degree:

Earth and Space Sciences & Astrobiology

University of Washington

Abstract

The co-evolution of life and the nitrogen cycle on the early Earth

Matthew C. Koehler

Chair of the Supervisory Committee:
Roger Buick, Ph.D.
Earth and Spaces Sciences & Astrobiology

Nitrogen is an essential element for all life as we know it. Its abundance and speciation in the atmosphere and ocean has been dynamic through Earth's history. The dynamic nature of nitrogen cycling is invariably linked to the dynamic nature of oxygenation on the early Earth, and the evolution of these two biogeochemical cycles influenced biological evolution and diversification. Exploration of the mode, tempo, and scale of such changes will add to our mechanistic understanding of these components of the inhabited Earth-system and should provide insight into how these cycles might operate on an alien planet that is different from our own. Here, I explore four critical points in Earth's redox and biological evolution: Chapter 2 – The dominantly anoxic world of the Mesoarchean, when aerobic nitrogen metabolisms did not exist, and bioavailable nitrogen could only be obtained through biological nitrogen fixation or remineralized

ammonium. Biological nitrogen fixation by the Mo-nitrogenase dominated. Chapter 3 – Incipient oxygenation ~300 Myr before the great oxidation event. We start to characterize the mode, tempo, and scale of these transient oxygenation events, and provide the oldest evidence of aerobic nitrogen cycling 2.66 Gyr ago. Chapter 4 – The state of nitrogen cycling during the Mesoproterozoic. We find further evidence that the Mesoproterozoic was characterized by an oceanic nitrate minimum, and that this nitrate scarcity could have prevented the radiation of early eukaryotes until the end of the Proterozoic. Chapter 5 – Nitrogen cycling across the Hirnantian glaciation and end Ordovician mass extinction event. We find that oceans during this period were characterized by widespread ocean anoxia that led to a scarcity in nitrate much like in the Mesoproterozoic. Nitrate scarcity was temporarily alleviated in near-shore settings during glaciation. Much like in the Pacific Ocean during the Last Glacial Maximum, the carbonate compensation depth at multiple sites seems to have deepened substantially during peak Hirnantian glaciation. These results highlight the relationship between ecology, evolution, nitrogen speciation/abundance, and surface oxygen.

TABLE OF CONTENTS

LIST OF FIGURES

LIST OF TABLES

ACKNOWLEDGEMENTS

I am extremely fortunate to have had Roger as an advisor. His creativity and near encyclopedic knowledge of early Earth geology and biogeochemistry are admirable, but equally admirable is his professionalism and character. He is incredibly reasonable, easy to work with, easy get along with, and his door has always been open. Not to mention his sense of humor is right up my alley. Being a great scientist means little if you're not a great person. Roger is most definitely both. If I become a scientist when I grow up, he is the kind I want to be.

My time at UW is sprinkled with inspirational people who have helped me develop academically and personally. Particularly I have admired the passion Jody B. and Charlotte S. (AKA the Empress of Evaporites) have demonstrated in their works, and I have learned so much from them. They have both been exceedingly kind to me, and are both forces of nature. David C. has also been kind to me, and his sense of humor is also something I always appreciate. I am very glad he is on my committee. Eric S. and Sharon D. have also been exceptional committee members, and I am grateful for their comments and guidance. Eavesdropping on Eric super passionately talking about isotopes in the isolab always put a smile on my face. Fangzhen T. is a great teacher and has always been a pleasure to talk to. He has shown real interest and enthusiasm in my academic pursuits, and he too has a fantastic sense of humor. Lab members Mike K., Jana M., Eric G., and Owen L. have been a great support system. I am certain they are going to make up the next generation of super-scientists, if that is what they want! Me? It might be nice to open up a tavern… am I rambling?

None of my work, or any other light-stable isotope work in UW ESS would be possible without Andy Schauer. He is… the best. As an engineer, as a scientist, and as an occasionally grumpy but still humorous person. Sorry I still haven't paid for stuff…

DEDICATION

To the poor souls who read this entire thing

And to my friends and family who know better

I love you all

Chapter 1: INTRODUCTION

The six most important bioessential elements for life as we know it are carbon, hydrogen, oxygen, nitrogen, phosphorus, and sulfur. Five of these elements are in the top ten most abundant elements in the universe. Planetary bodies both inside and outside of the Solar System likely harbor these elements in different forms, potentially in varying phases and redox states on their surfaces where life is more likely to emerge and proliferate. It makes sense, then, to use Earth's biochemistry as an analog for other life in the universe. This assumes that extraterrestrial life would utilize similar nutrients and energy sources as our own. If we believe that these assumptions are our best anchor for the search for signs of life on other planetary bodies, then the natural prerequisite to this search is to examine how life and these elements co-evolved through Earth's history. Understanding how the abundance and speciation of these elements have changed in Earth's atmosphere and oceans through time provides a mechanistic foundation for exploring biogeochemical evolution on other worlds that may be different from ours. This is the astrobiological foundation for the following dissertation that focuses on the co-evolution of life and the nitrogen cycle on early Earth.

The earliest signs of life on Earth come from equivocal trace fossils and organic matter from ~4.1 to ~3.8 Ga. The abundance and speciation of nitrogen in the atmosphere and ocean during this time is relatively unknown. Before the evolution of biological nitrogen fixation[1], fluxes of nitrogen from the atmosphere to the ocean were dominated by NO_x species produced from atmospheric N_2 by lightning and bolide impact plumes. Importantly, these abiotic fixation fluxes would have been at least an order of magnitude less than modern biological nitrogen fixation

[1] The biologically-mediated conversion of N_2 gas to bioavailable nitrogen.

(Stüeken E.E., Kipp M.A., **Koehler M.C.**, Buick R., 2016). Biological utilization of this NO_3^-/NO_2^- could have supported a proportionally smaller ancient biosphere before the evolution of biological nitrogen fixation. There is firm isotopic evidence that biological nitrogen fixation by the Mo-nitrogenase evolved before 3.2 Ga (Stüeken E.E., Buick R., Guy B.M., **Koehler M.C.**, 2015; **Koehler M.C.**, Buick R., Barley M.E., in review), but ubiquitous alteration of older sedimentary rocks inhibits extending this isotopic record further back in time. Still, with this finding we know that the biosphere had a first-order control on the nitrogen cycle since the Mesoarchean. Until the evolution of denitrification[2], the nitrogen cycle would be missing a significant return flux to the atmosphere, and so fixed nitrogen could have possibly accumulate in the oceans, sediments, and crust. A growing body of evidence points to substantially lower atmospheric pressure in the Neoarchean, mainly due to a lower partial pressure of nitrogen. A modelling study suggests that a relatively high biomass burial rate in the Archean could have resulted in a drawdown of atmospheric N_2 to less than half of modern levels (Stüeken E.E., Kipp M.A., **Koehler M.C.**, Schwieterman E.W., Johnson B., Buick R., 2016).

The first strong evidence for denitrification is from the Neoarchean, over 250 Myr before the Great Oxidation Event[3] (GOE; **Koehler M.C.**, Buick R., Kipp M.A., Stüeken E.E., Zaloumis J., In Press). Interestingly, the available evidence suggests there was at least a 500 Myr gap between the evolution of nitrogen fixation and denitrification. These early signs of denitrification before the GOE are associated with transient "whiffs" of oxygen in the surface ocean and atmosphere. Enhanced oxidative weathering due to increases in atmospheric oxygen may have caused a rebound in atmospheric N_2 by shortening the residence time of crustal nitrogen. After the

[2] The biologically-mediated reduction of oxidized nitrogen species (nitrate, nitrite) to N_2 gas.
[3] The Great Oxidation Event is characterized by the increase of atmospheric oxygen over 10^{-5} present atmospheric levels. It is dated to ~2.33 Ga.

GOE, nitrogen isotopes indicate a globally significant increase in oceanic nitrate and aerobic nitrogen cycling, almost reminiscent of the modern ocean. This period is often described as an "oxygen overshoot". Whether or not the oxygen overshoot was a period when surface oxygen approached modern levels, it represents a temporary maximum in ocean oxygenation and nitrate levels.

Towards the end of the Paleoproterozoic and through the Mesoproterozoic, the nitrogen isotope record indicates a decrease in oceanic nitrate, particularly in offshore environments (**Koehler M.C.**, Stüeken E.E., Kipp M.A., Buick R., 2017). This is coincident with the appearance of eukaryotic microfossils in the geologic record. Eukaryotic microfossils primarily rely on nitrate as a nitrogen source, because they are unable to fix atmospheric N_2 and do not compete well against prokaryotic organisms for NH_4^+. The onshore-offshore gradient in oceanic nitrate correlates with an onshore-offshore decrease in the richness and abundance of eukaryotic microfossils. It thus appears that low Mesoproterozoic nitrate levels, likely caused by a decrease in surface oxygen levels, resulted in the restriction of eukaryotes to nearshore environments, potentially delaying their proliferation and rise to ecological dominance until ocean and atmospheric oxygen levels increased in the Neoproterozoic/Paleozoic.

While surface oxygenation was originally thought to have risen sharply in the Neoproterozoic, new ocean redox data suggests that deep-sea oxygenation was probably protracted through the Paleozoic. Indeed, nitrogen isotopes across the Ordovician-Silurian boundary are reminiscent of the Mesoproterozoic, suggesting low oceanic nitrate levels and a scarcity of fixed nitrogen, particularly in offshore environments (**Koehler M.C.**, Stüeken E.E., Prave A.R., in prep). It is possible that full ocean oxygenation and a rise to near-modern nitrate levels did not occur until the rise of land plants in the Devonian. Even so, ocean anoxic events associated with mass

extinctions through the Phanerozoic periodically decreased ocean nitrate to levels similar to those in the Mesoproterozoic.

As alluded to above, the four chapters in this dissertation examine the co-evolution of nitrogen cycling, surface oxygen, and life at critical times on the ancient Earth. The first explores the Mesoarchean redox and nitrogen cycle landscape at relatively high temporal resolution. This was apparently before the advent of aerobic nitrogen cycling. The second chapter looks for the oldest signs of aerobic nitrogen cycling in the Neoarchean, and explores the mode, tempo, and scope of transient oxygenation events before the GOE. The third chapter deals with oceanic nitrate availability in the Mesoproterozoic, and how it related to eukaryotic evolution. The last chapter focuses on nitrogen cycling, carbon cycling, and the redox landscape in the Paleozoic; specifically across the Ordovician-Silurian boundary. This period hosts the first major glaciation of the Phanerozoic, and one of the five big mass extinction events. By enhancing our understanding of how nitrogen, oxygen, and life evolved on the early Earth, the chapters in this dissertation add to the astrobiological exploration of how biogeochemical cycles may evolve on strange new worlds, and how this may affect habitability and the evolution of extraterrestrial life.

My role in the projects discussed in this dissertation are as follows: Roger Buick and I devised chapter 2, I conducted all analyses, Roger Buick and I interpreted the results and wrote the manuscript. Samples were provided by Mark Barley. Chapter 3 was devised by Roger Buick. All nitrogen and carbon analyses were performed by me. Selenium analyses were performed by Michael Kipp, Eva Stüeken, Jon Zaloumis, and myself. Roger Buick and I performed the petrographic work. Myself, Roger Buick, Michael Kipp, and Eva Stüeken interpreted the results and wrote the manuscript. Samples were provided by Roger Buick and the Agouron Institute Drilling Project. Chapter 4 was devised by myself, Roger Buick, and Eva Stüeken. Analyses were

performed by primarily by myself, with help from Eva Stüeken and Michael Kipp. All authors contributed to data interpretation and writing the manuscript. Samples were provided by Roger Buick and Andy Knoll. Chapter 5 was devised by myself and Eva Stüeken. I collected the samples with help from Tony Prave and Eva Stüeken. I carried out all the analyses, and largely interpreted the result with help from Eva Stüeken. I wrote the manuscript.

Chapter 2: NITROGEN ISOTOPE EVIDENCE FOR ANOXIC DEEP MARINE ENVIRONMENTS FROM THE MESOARCHEAN MOSQUITO CREEK FORMATION, AUSTRALIA

This manuscript has been submitted to the journal *Precambrian Research*
Co-authored by Matthew C. Koehler, Roger Buick, and Mark E. Barley

2.1 *Abstract*

Recent evidence suggests that oxygenated environments in the Mesoarchean were limited to the shallowest marine and fluvio-lacustrine settings. It is becoming increasingly clear that during the Neoarchean oxidizing conditions spread to the photic zone of deeper shelf and basinal depositional environments. Here we present nitrogen and carbon isotope ratios from the Mosquito Creek Formation of the Nullagine Group (~2.9 Ga) to further explore the Mesoarchean redox landscape. The $\delta^{15}N$ and $\delta^{13}C_{org}$ values are invariant and suggest an ecosystem dominated by nitrogen fixers (anaerobic nitrogen cycling) and CO_2 fixation by the Calvin Cycle. These data (i) support the apparent Mesoarchean trends of decreasing oxidant availability and methane cycling from onshore to offshore depositional environments, (ii) provide further evidence that the Mosquito Creek Formation was deposited in a deep marine setting, and (iii) contain $\delta^{15}N$ values that highlight the persistence of nitrogen fixation by Mo-nitrogenase and the dearth of aerobic nitrogen metabolisms in the Mesoarchean.

2.2 *Introduction*

It has been argued, based on sulfur isotope evidence, that Earth's atmosphere was persistently oxygenated throughout the Archean era (1). Now, this is distinctly a minority view,

with abundant evidence contradicting it from samples collected at high stratigraphic resolution and analyzed for quadruple sulfur isotopes (2), nitrogen isotopes (3, 4), selenium isotopes (5) and trace metal abundances and isotopes (6–11). These indicate instead that the lower atmosphere during the Neoarchean was generally anoxic except for a few transient "whiffs" of oxygen (e.g. 6). However, few relevant studies have been done to determine if this pattern extends back into the Mesoarchean. The emerging view is that free O_2 in the Mesoarchean was limited to localized production in the shallowest marine (12–15), and perhaps fluvial-lacustrine-terrestrial environments (16, 17). Apart from a single study (18) of Mo and Cr isotopes, which have complex fractionation pathways and thus lesser redox sensitivity, distal-marine rocks have not been examined using other redox proxies to further explore the Mesoarchean redox landscape. Here, we analyze nitrogen and carbon isotope ratios in rocks of the Mosquito Creek Formation from the same ABDP #5 drill-core that was studied to formulate the provocative oxic Archean atmosphere hypothesis (1). Our data are consistent with (i) anoxic waters in distal-marine settings, (ii) the apparent ecological irrelevance of nitrification-denitrification metabolisms before the start of the Neoarchean, and (iii) a facies-dependent trend of more depleted $\delta^{13}C$ values in fluvial-lacustrine-proximal marine environments compared to more distal marine settings in the Mesoarchean.

2.3 *Geologic Setting*

The samples analyzed here came from the Nullagine Group, which is located in the southeastern corner of the Pilbara Craton in northwestern Australia (Figure 2.1). This unit has been subdivided into the underlying Coondamar Formation and the upper Mosquito Creek Formation, with our samples all coming from the latter. The samples are predominantly kerogenous shales and siltstones from the finer-grained D and E portions of graded turbidites deposited distally in

subaqueous fans formed beneath subaerial fan-deltas (Figure 2.2, Figure 2.3) (19, 20). The tectonic setting of the basin in which these turbidities were deposited is controversial. It was initially interpreted as a fore-arc basin facing an open ocean to the south (19) based on facies and provenance analysis. Alternatively, deposition of the Mosquito Creek basin along a passive continental margin was proposed based on a geochemical discriminant factor analysis (21), also in a setting with an open connection to the ocean but in this case to the west. By contrast, Nijman and colleagues (20) advocated deposition in an intracontinental intermontane basin that may or may not have been marine, based on the fining-upward style of sedimentation and overall underfilling of the basin. Our data may help to partially resolve this controversy.

Our samples, 47 in total, were obtained at roughly meter-scale resolution from the drill-core ABDP #5 which was collared at Lat. 21° 41' 53.7"S, Long. 120° 37' 14.5"E in the Eastern Creek gold-mining area ~55 km to the northeast of the town of Nullagine (1). These rocks have been metamorphosed from sub- to lower-greenschist facies (1, 22) and have been strongly deformed multiple times resulting in tight folding, thrust faulting and a variably developed schistosity (21). Their depositional age is constrained between a maximum detrital zircon U/Pb date of 2971 ± 15 Ma from near the base of the ~5 km thick Mosquito Creek Formation (21) and a minimum Pb-Pb model age from galena in cross-cutting lode gold mineralization of 2905 ± 9 Ma (Thorpe et al., 1992).

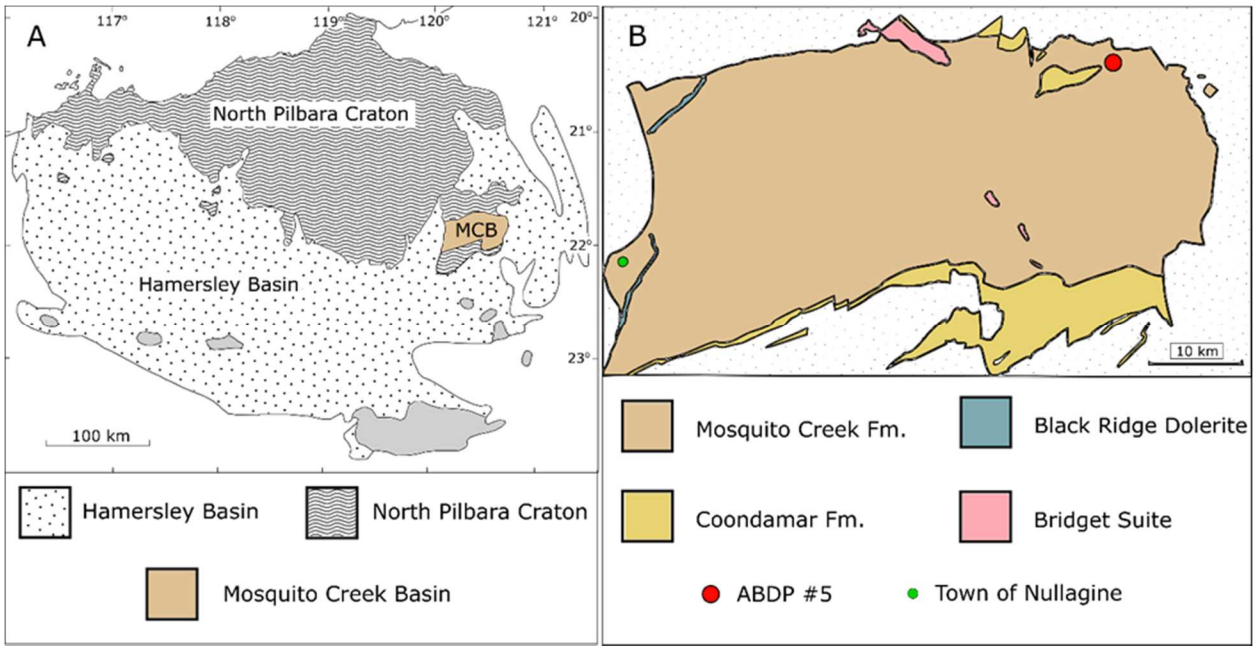

Figure 2.1**. Location map modeled after (21) showing A) a simplified map of the Pilbara Craton, B) a simplified map of the Mosquito Creek Basin highlighted in "A".**

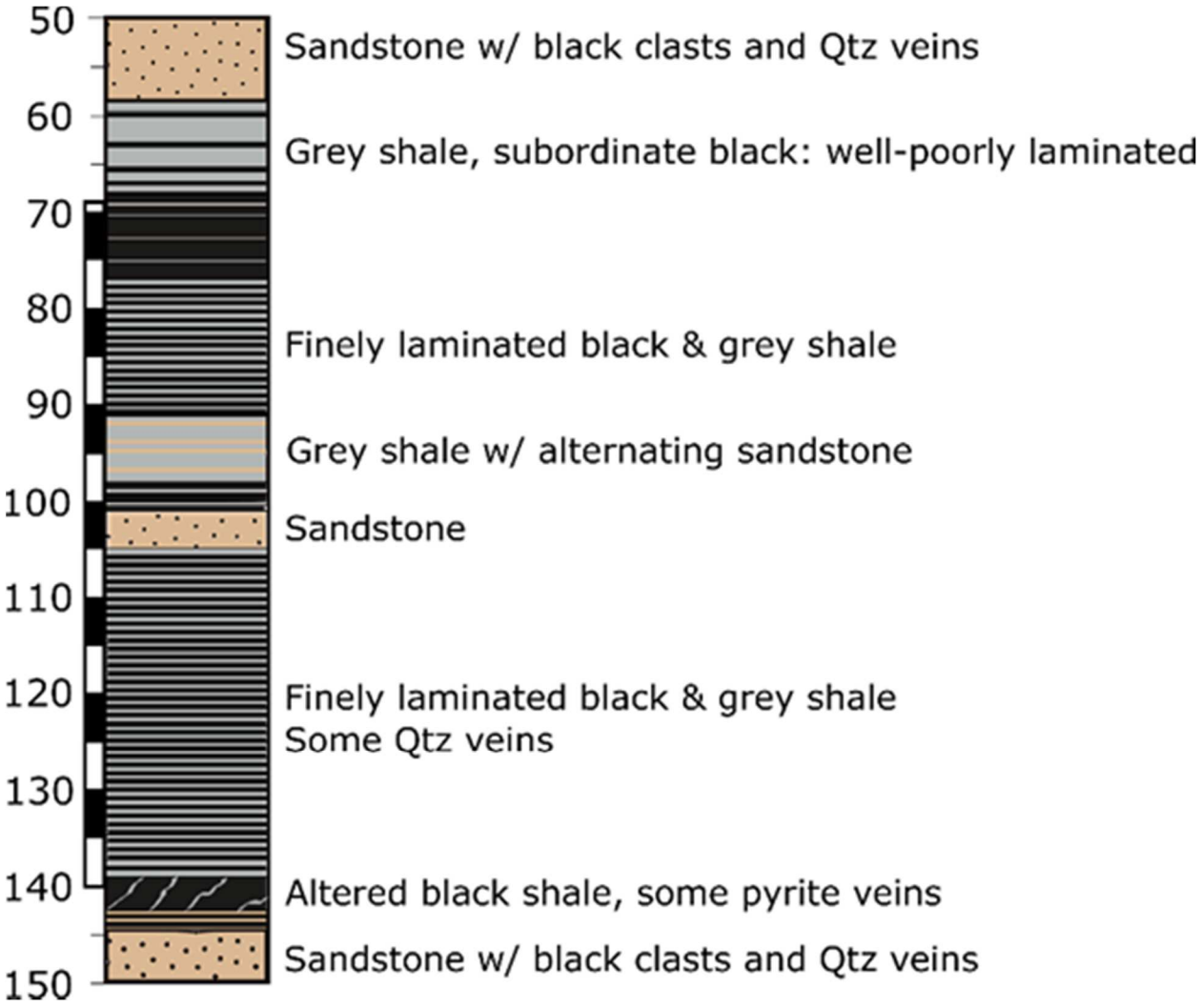

Figure 2.2**. ABDP #5 stratigraphy from 50m to 150m depth**. The section analyzed in this study is indicated by the black and white striped bar. Modified from (1).

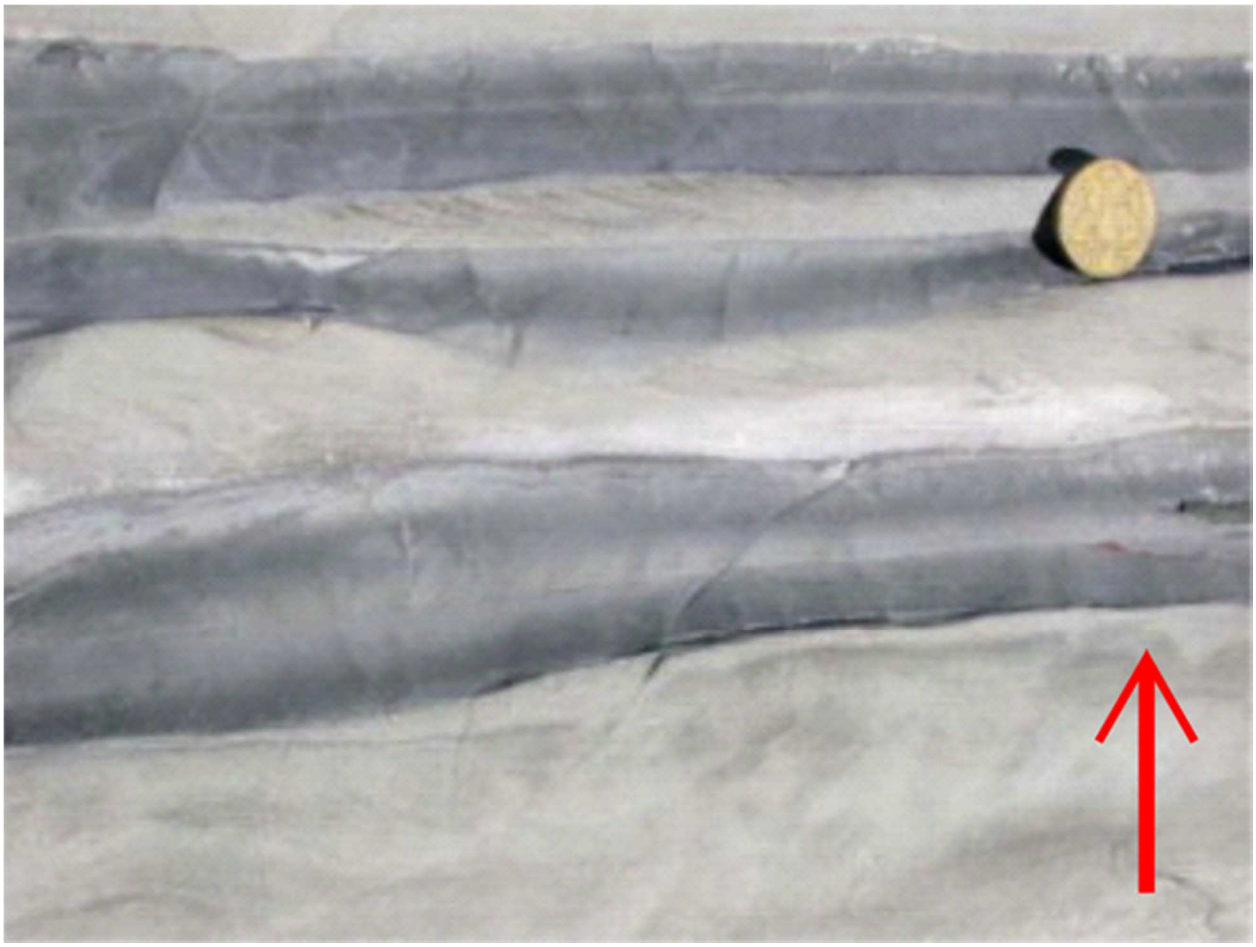

Figure 2.3**. Field photo of rippled sandy C, silty D and shaley E turbidite facies of the Mosquito Creek Formation (modified from (21))**. Red arrow indicates stratigraphic up. The samples studied here predominately came from D and E facies. The coin for scale is 25 mm in diameter.

2.4 *Methods*

Samples for bulk nitrogen and carbon analyses were prepared using standard methods that have been utilized successfully in previous studies (23, 24). All glassware and the silica sand used for cleaning were combusted in a muffle furnace at 500°C overnight to remove organic contaminants. All chemicals used were reagent-grade. Rock samples from ABDP #5 were cut into ~3 x 3 x 2 cm chips, and all surfaces were shaved with a diamond-tipped rock saw to minimize modern contamination. Chips were then manually crushed between a large mortar and steel plate, each wrapped in clean aluminum foil to reduce contamination. The aluminum foil was changed between each sample. The resulting smaller ($\leq$ 1 cm^3) chips were then transferred to small, clean glass beakers. Each sample was then sonicated with ethanol for ~2 minutes, decanted, and then with 2N HCl for ~20 seconds to further remove modern contaminants. After decanting the HCl, samples were rinsed 3 times with 18MΩ milli-Q water and left covered in a 60°C ventilated drying oven until completely dry. Samples were then pulverized using an aluminum oxide puck mill that was cleaned with ethanol, 18MΩ milli-Q water, and silica-sand between each sample. The resulting sample powders were stored in glass scintillation vials.

Powder aliquots of about ~0.5 grams were weighed into glass centrifuge tubes and were acidified in three iterations with 6N HCl. For each iteration, the acid was left to digest the sample, covered, in a 60°C ventilated oven overnight (~24 hours). After decanting the acid from the last iteration, the samples were washed three times with 18MΩ milli-Q water to remove the HCl. The water from the last rinse was then decanted and covered samples were left to dry in a 60°C ventilated oven for two days. After drying, samples were weighed again to determine sample carbonate concentrations gravimetrically.

Kerogen was extracted from a subset of samples, again using standard methods (23, 24) adapted from (25). 3-4 grams of powder were weighed in 250ml Teflon bottles and acidified with 100ml of 50% v/v hydrofluoric acid (HF) in a warm shaking water bath (55^{o}C) overnight to dissolve the silicate matrix. Because fluoride precipitates can form during this process, the samples were then reacted with 100ml of saturated boric acid in 50% v/v HF to remove them. Samples were then washed thoroughly in three iterations with 200ml of 18MΩ milli-Q water. Kerogen was then transferred from the Teflon bottles to glass scintillation vials with 10ml of 18MΩ milli-Q water and subsequently frozen. Samples were then freeze-dried for two days.

Total organic carbon (TOC), $\delta^{13}C_{org}$, total nitrogen (TN), $\delta^{15}N_{bulk}$, and $\delta^{15}N_{kerogen}$ values were measured using a Costech ECS 4010 Elemental Analyzer coupled to a Thermo Finnigan MAT253 continuous-flow isotope-ratio mass spectrometer. Samples were bracketed by three in-house standards (calibrated to reference materials USGS40 and USGS41;(26)) to calibrate sample analyses and monitor accuracy. Each run also contained two analyses of a fourth rock-standard "UW McRae" to monitor long-term precision. Average analytical accuracy and precision for $\delta^{15}N$ measurements were 0.15 ± 0.11‰, and 0.15‰ respectively. Average analytical accuracy and precision for $\delta^{13}C$ measurements were 0.1 ± 0.06‰, and 0.08‰ respectively. Nitrogen and carbon isotope values are presented in standard delta notation relative to air and VPDB respectively.

2.5 *Results*

The most notable aspect of the Mosquito Creek nitrogen and carbon data is how invariant it is through the section (Figure 2.4). $\delta^{15}N_{bulk}$ values average -1.8‰ ± 0.29‰ (1σ), where the standard deviation among the samples is less than the average standard deviation of sample replicates (0.33‰ 1σ). $\delta^{13}C_{org}$ values average -32.3‰ ± 0.41‰ (1σ), with close to half of the variability (0.16‰) coming from the four sandstone samples. This is greater than the average standard deviation among sample replicates (0.09‰ 1σ). Total nitrogen abundances of 0.009 ± 0.002 [%], total organic carbon levels of 0.34 ± 0.1 [%], total inorganic carbon values of 24 ± 3.6 [%], and C_{org}/N_{bulk} atomic ratios of 42 ± 8.9 all have standard deviations (1σ) that are below 30% of the average.

$\delta^{15}N_{kerogen}$ values are slightly more depleted and variable than $\delta^{15}N_{bulk}$ values of the same sample set, averaging -2.5‰ ± 0.64‰ (1σ). The average standard deviation for sample replicates is 0.22‰ (1σ). In contrast, $\delta^{13}C_{kerogen}$ values are almost identical to the corresponding bulk-rock $\delta^{13}C_{org}$ ratios (Figure 2.4). $C_{org}/N_{kerogen}$ atomic ratios average 360 ± 46.5, and the fraction of total nitrogen in a bulk sample that is bound into kerogen is 0.11 ± 0.016.

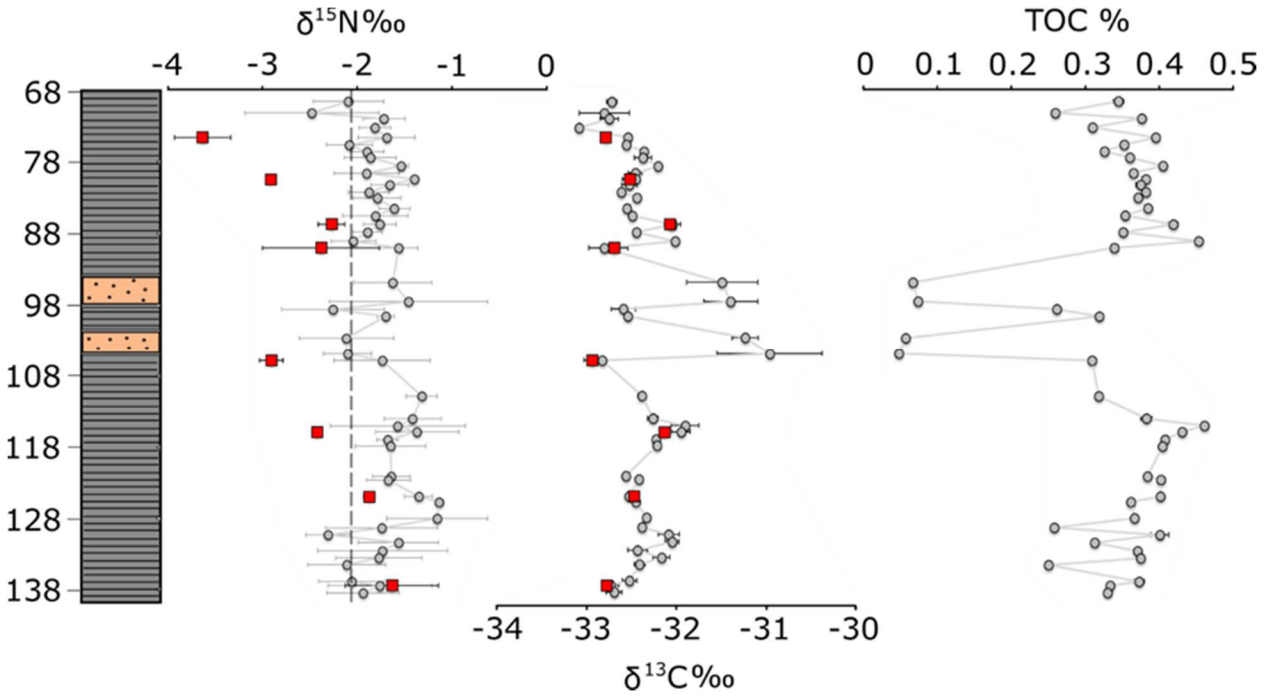

Figure 2.4**. Simplified stratigraphic section with $\delta^{13}C_{org}$, $\delta^{15}N_{bulk}$, $\delta^{15}N_{kerogen}$, TOC%**. Grey circles are from bulk measurements and red squares represent kerogen measurements.

2.6 *Discussion*

2.6.1 *Isotopic fidelity*

Because the metamorphic grade of the Mosquito Creek Formation is no higher than lower greenschist facies, post-depositional thermal alteration of the primary nitrogen and carbon isotopic signal has likely been less than 2‰ (28–30). Indications that these isotopic systems have been significantly thermally altered, such as a positive correlation between $\delta^{15}N$ values and C/N ratios or a large disparity between $\delta^{15}N_{kerogen}$ and $\delta^{15}N_{bulk}$ values, are not present in our dataset (Figure 2.4, Figure 2.5). Post-depositional diagenetic alteration can lead to an increase of the primary $\delta^{15}N$ signal by up to 4‰ under oxic conditions through preferential deamination of ^{14}N from organic matter followed by nitrification of this isotopically light NH_4^+ and loss from the system (31–34). However, the absence of bioturbation in the Mesoarchean would have likely left sediments anoxic regardless of overlying water redox conditions so this diagenetic process would have been inoperative. Diagenetic alteration under anoxic conditions can potentially lead to a decrease in the primary $\delta^{15}N$ value of organic matter if there is significant *in situ* growth of $\delta^{15}N$-depleted nitrogen-fixing bacteria among sedimentary organic matter with positive $\delta^{15}N$ values, or if there is preferential deamination of ^{15}N-rich compounds such as proteins (32, 35, 36). However, the consistently low $\delta^{15}N$ values throughout the section suggest that *in situ* growth of N-fixing bacteria or deamination of ^{15}N-rich compounds during diagenesis was unlikely to have affected the primary isotopic composition by more than a couple of per mil. Thus, the original $\delta^{15}N$ of the sedimentary organic matter was probably close to what it is now.

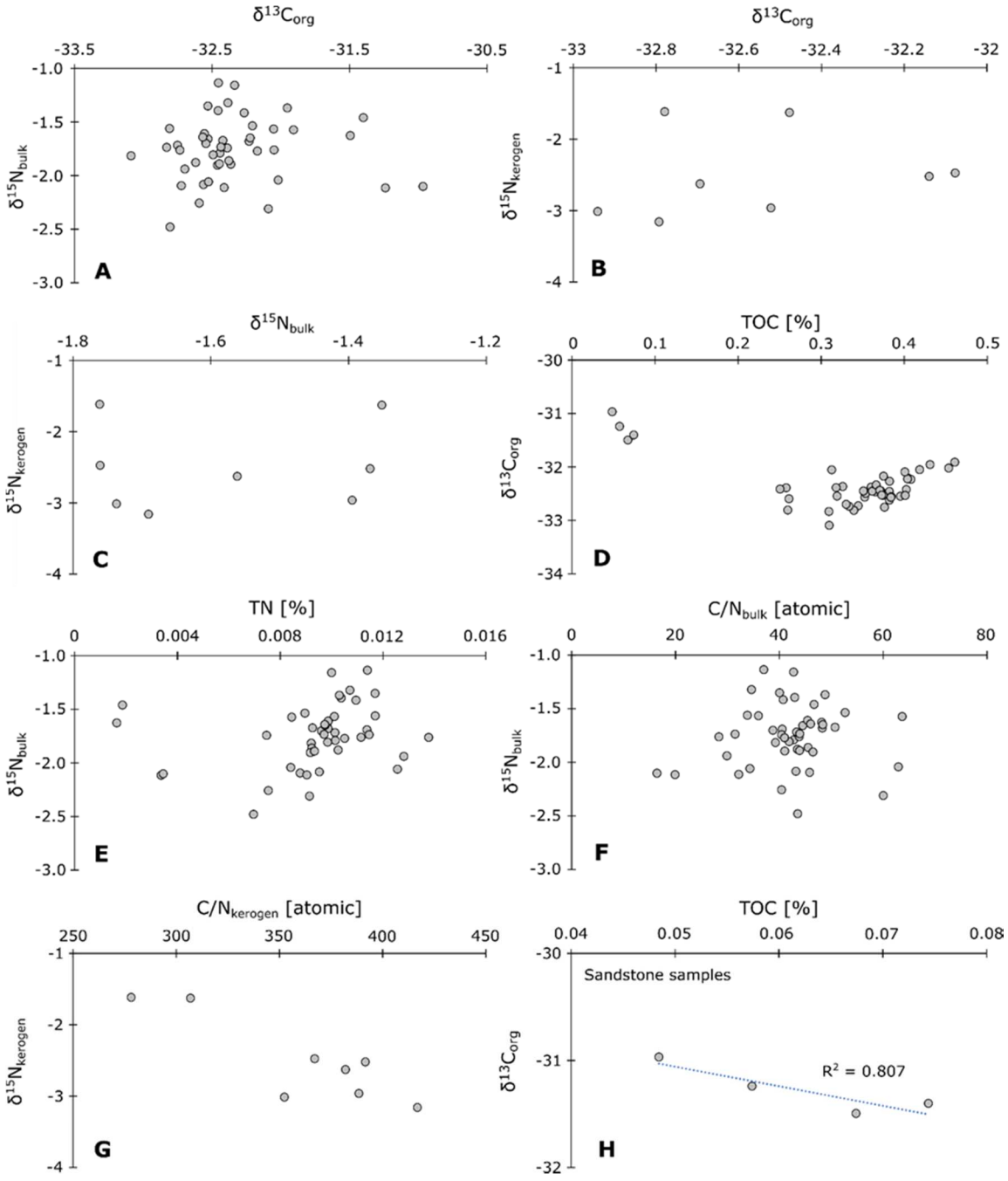

Figure 2.5**. Cross-plots of carbon and nitrogen isotope/abundance measurements**. A) $\delta^{15}N_{bulk}$ vs. $\delta^{13}C_{org}$, B) $\delta^{15}N_{kerogen}$ vs. $\delta^{13}C_{org}$, C) $\delta^{15}N_{kerogen}$ vs. $\delta^{15}N_{bulk}$, D) $\delta^{13}C_{org}$ vs. TOC, E) $\delta^{15}N_{bulk}$ vs. TN, F) $\delta^{15}N_{bulk}$ vs. C/N_{bulk}, G) $\delta^{15}N_{kerogen}$ vs. $C/N_{kerogen}$, H) $\delta^{13}C_{org}$ vs. TOC for sandstone samples. TOC – Total organic carbon; TN – Total nitrogen. Note all isotope measurements are expressed in parts per thousand and C/N ratios are atomic ratios.

2.6.2 *Redox and paleoecology*

The nitrogen isotopic values of almost all samples (both bulk and kerogen measurements) are between -3‰ to -1‰, suggesting an ecosystem dominated by nitrogen fixation using the molybdenum nitrogenase (37), with no signs of any aerobic nitrogen cycling utilizing NO_3^-. Partial nitrification of ammonium followed by quantitative denitrification, or quantitative nitrification followed by partial denitrification, would preferentially remove ^{14}N from the system as N_2 and increase the residual $\delta^{15}N$ values preserved in the rock record (28, 38). These scenarios require free O_2 and are inconsistent with our data. Redox data from the literature suggests that the Mesoarchean was an era where only the shallowest marine and fluvial-lacustrine environments had appreciable oxidants (12–16) for metabolisms such as non-quantitative sulfate reduction (12) and perhaps anaerobic oxidation of methane (17). Together with studies of hydrothermally influenced banded iron formations (39) and distal marine shale/mudstones (40, 41), our data from the deep-water Mosquito Creek Fm. further support this paleogeographic redox trend, showing that oxidants were limited or absent in offshore settings. Such a trend could have resulted from (i) lower concentrations of oxygen sinks such as organic matter, Fe(II), and reduced sulfur species onshore (e.g. 12), and/or (ii) greater local oxygen production due to greater nutrient availability (e.g. 15) in shallow marine and terrestrial environments.

The Mosquito Creek carbon isotope data (average -32‰) can be explained by an ecosystem dominated by CO_2 fixation using the Calvin Cycle, but do not preclude a subordinate role for chemosynthetic organisms. Lacking distinct evidence for dissolved O_2 and oxygenic photosynthesis, it is more likely that ecological dominance of anoxygenic photosynthesizers are responsible for the measured $\delta^{13}C_{org}$ values. The $\delta^{13}C_{org}$ of the four sandstone samples are enriched compared to the shale samples by an average of 1‰. This enrichment is coupled to lower TOC

concentrations. Within the sandstone samples there is a negative correlation between TOC and $\delta^{13}C_{org}$, which could be explained by the progressive dilution of heavier carbon through the addition of lighter carbon. This could arise when enriched detrital carbon was progressively diluted with the more depleted carbon source responsible for the $\delta^{13}C_{org}$ of the shale samples. It could also reflect differences in diagenesis associated with the lithologic change from shale to sandstone with light carbon being preferentially removed by migrating fluid phases in sands with higher porosity and permeability. Regardless, this small difference of ~1‰ does not affect our overall interpretation of the carbon data.

Interestingly, both the Mesoarchean (17) and Neoarchean (42) are characterized by environmental gradients in $\delta^{13}C_{org}$ values with fluvial-lacustrine settings being the most depleted, consistent with a larger role of methanogens/methanotrophs. Though both the Mesoarchean and Neoarchean are characterized by this facies-dependent trend in local carbon-fixing ecologies, the carbon isotope record suggests more vigorous methanogenesis/methanotrophy in all Neoarchean environments, even in offshore settings. So, while the golden age of methanogenesis/methanotrophy is attributed to the Neoarchean (42), when evidence of oxygenation extends to deeper marine environments, our data support the idea that methane cycling in the Mesoarchean seems to have been restricted to lakes, rivers, and shallow marine settings (17). Non-marine carbon isotope measurements from the Mesoarchean range from 28‰ to 47‰, while marine measurements range from 27‰ to 33‰. These ranges suggest a more diverse carbon fixation ecology, that included methanogens, in non-marine environments. The tight grouping of marine $\delta^{13}C$ values from this and previous studies indicate more homogenous and less diverse carbon fixation strategies in offshore environments.

The relationship between oxidant availability, methanogenesis, and methanotrophy is complex. It is likely that increasingly depleted $\delta^{13}C$ values correspond to greater oxidant availability and a coincident rising role of methanotrophs from the Mesoarchean to the Neoarchean as combined carbon isotope and redox data would suggest. This scenario would require greater rates of biogenic methane production than oxidant consumption, such that anaerobic and/or aerobic methane oxidation rates would increase with oxidant supply (Figure 2.6, scenario #1). Importantly, this would not require any change in methane production across the Meso/Neoarchean boundary. However, once the oxidant flux overwhelms the biogenic methane flux and their respiratory consumption starts competing with methanogenesis for reduced substrates, the inverse relationship would be true. In such a case progressively lighter $\delta^{13}C$ values would result from a decreasing oxidant flux, less competition for organic carbon and H_2 between methanogens and organisms that use anaerobic respiration, and so perhaps the proliferation of methanogens (Figure 2.6, scenario #2). Therefore a more quantitative understanding of the relationship between oxidants and methane during the Precambrian is critical when interpreting local carbon isotope records (42–44).

2.6.3 *Marine or non-marine?*

These data help to resolve the controversy over the depositional setting of the Mosquito Creek basin. Though they cannot inform about its tectonic style, they can illuminate whether it was marine (19, 21) or potentially non-marine, as in the intermontane basin model (20). Comparison of the $\delta^{15}N$ and $\delta^{13}C$ values of the Mosquito Creek rocks with near-contemporary units of known marine or non-marine origin (Figure 2.7) allows environmental discrimination. In carbon-nitrogen isotope space, the Mosquito Creek data most closely resemble the marine Witwatersrand (~2.9 Ga) and Soanesville (~3.19 Ga) samples (Figure 2.7A and Figure 0.2).

However, they differ markedly from most Mesoarchean and Neoarchean non-marine samples and Neoarchean marine samples (Figure 2.7B, **Error! Reference source not found.**, Figure 0.2, and Figure 0.3), with only the Lalla Rookh (~3.0 Ga) data plotting anywhere nearby. However, the Lalla

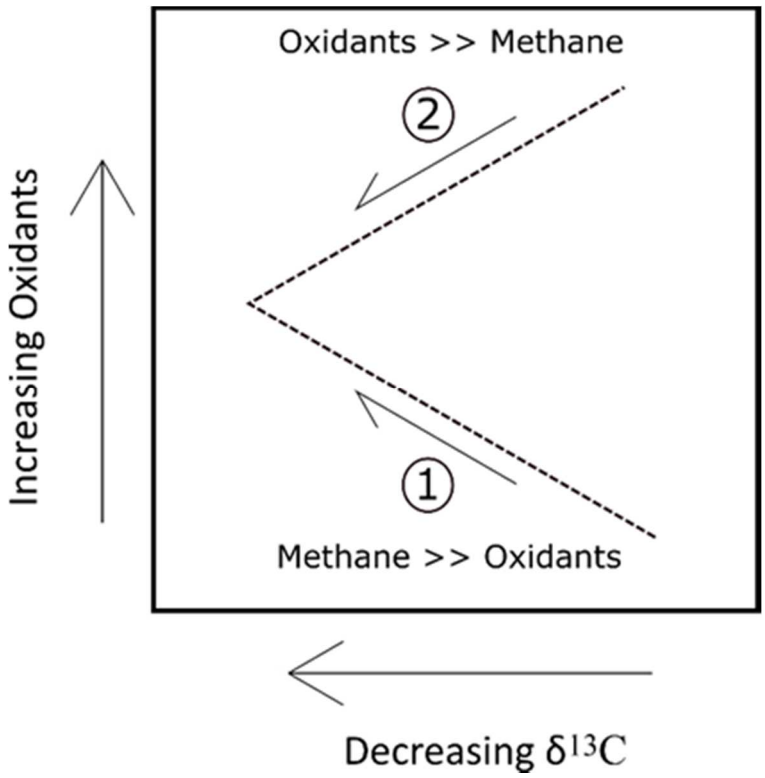

Figure 2.6**. Schematic of the relationship between $\delta^{13}C_{org}$ values and oxidant availability**. Scenarios 1 and 2 are described in section 2.6.2.

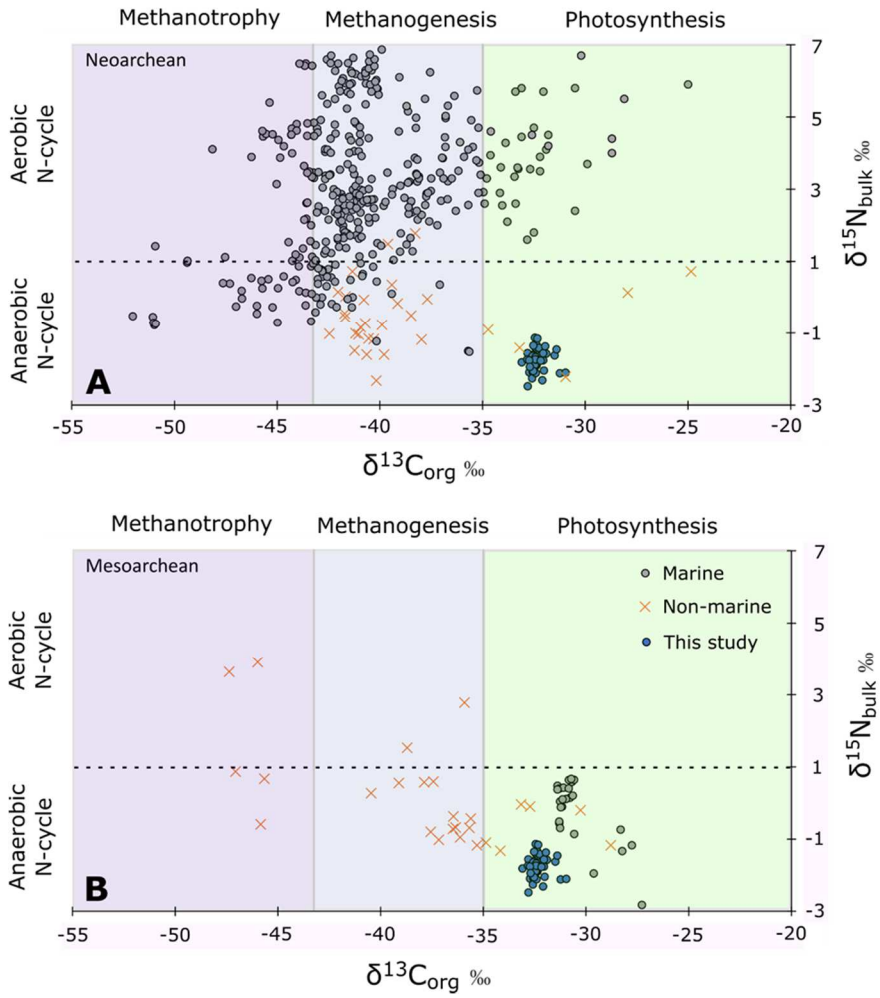

Figure 2.7. **Cross-plots of $\delta^{13}C_{org}$ vs. $\delta^{15}N_{bulk}$ for the (A) Mesoarchean, and (B) Neoarchean**. Grey circles are marine data, orange X's are non-marine data, blue circles are from this study. Horizontal dashed line separates $\delta^{15}N_{bulk}$ values consistent with nitrogen fixation by the Mo-nitrogenase (below) from $\delta^{15}N_{bulk}$ values consistent with some degree of aerobic nitrogen cycling (above). Shaded colors represent the following: Green - $\delta^{13}C_{org}$ values consistent with carbon fixation using the Calvin Cycle; Blue - $\delta^{13}C_{org}$ values consistent with carbon fixation using the Wood-Ljungdahl pathway; Purple - $\delta^{13}C_{org}$ values consistent with methanotrophic carbon cycling. Only least-altered data from the Archean were included, and were taken from a compilation in (38), with added data from (17, 45). While there are more $\delta^{15}N$ values from the Archean not shown here, the fidelity of those measurements based on potential alteration and/or large analytical uncertainly (see supplementary materials of (41)) have been excluded.

Rookh samples have distinctly lighter $\delta^{13}C_{org}$ values with a greater spread than the tightly clustered Mosquito Creek data, suggesting a more variable environment and microbiota than the homogeneous setting implied by the low Mosquito Creek variance. Thus, this strongly supports the idea that the Mosquito Creek basin was marine (19, 21) rather than deposited in an intracontinental intermontane basin (20)

2.6.4 *Implications for microbial evolution*

Data from the Archean suggest that nitrogen fixation by the molybdenum nitrogenase had evolved by 3.2 Ga (41), was widespread by ~2.9 Ga ((41); this study), and that nitrification and denitrification did not become significant metabolisms in the oceans until ~2.65 Ga (4). Given the evidence suggesting some *in situ* oxygen production in the shallowest marine and fluvial-lacustrine environments as far back as 3 Ga (12–17), it is possible that the nitrification and denitrification evolved before evidence for their ecological significance first appeared in the Neoarchean. However high-resolution exploration of older sections have yielded no strong evidence for aerobic nitrogen cycling ((41); this study), suggesting that nitrification and denitrification only became ecologically relevant with the later expansion of oxygenated surface waters.

2.7 *Acknowledgements*

This study was funded by NASA grant NNX16AI37G and NSF FESD grant 338810 to R.B. and U.W. ESS Departmental Awards to M.C.K. We thank the U.W. Isolab and Andy Schauer for technical support and we are particularly indebted to Sarah Barley for facilitating this research and for reviewing the manuscript.

Chapter 3: TRANSIENT SURFACE OCEAN OXYGENATION RECORDED IN THE ~2.66 GA JEERINAH FORMATION, AUSTRALIA

This manuscript has been submitted to the journal *Proceedings of the National Academy of Sciences*
Co-authored by Matthew C. Koehler, Roger Buick, Michael A. Kipp, Eva E. Stüeken, and Jonathan Zaloumis

3.1 *Abstract*

Many paleoredox proxies indicate low-level and dynamic incipient oxygenation of Earth's surface environments during the Neoarchean (2.8-2.5 Ga) prior to the Great Oxidation Event (GOE) at ~2.4 Ga. The mode, tempo, and scale of these redox changes are poorly understood because data from various locations and ages suggest both protracted and transient oxygenation. Here we present bulk-rock and kerogen-bound nitrogen isotope ratios as well as bulk-rock selenium abundances and isotope ratios from drill-cores sampled at high stratigraphic resolution through the Jeerinah Formation (~2.66 Ga; Fortescue Group, Western Australia) to test for changes in the redox state of the surface environment. We find that both shallow and deep depositional facies in the Jeerinah Fm display episodes of positive primary $\delta^{15}N$ values ranging from +4 to +6‰, recording aerobic nitrogen cycling that requires free O_2 in the upper water column. Moderate selenium enrichments up to 5.4 ppm in the nearer-shore core may indicate coincident oxidative weathering of sulfide minerals on land, though not to the extent seen in the younger Mt. McRae Shale that records a well-documented 'whiff' of atmospheric oxygen at 2.5 Ga. Unlike the Mt. McRae Shale, Jeerinah selenium isotopes do not show a significant excursion concurrent with the positive $\delta^{15}N$ values. Our data are thus most parsimoniously interpreted as evidence for transient

surface ocean oxygenation lasting less than 50 Myr, extending over hundreds of kilometers, and occuring well before the GOE. The nitrogen isotope data clearly record nitrification and denitrification, providing the oldest firm evidence for these microbial metabolisms.

3.2 *Introduction*

Despite widespread agreement about general trends (46), our understanding of the mode and tempo of Earth's oxygenation still suffers from considerable uncertainties. Among the more salient features of this record is a proposed "whiff" of oxygen in surface environments at 2.5 Ga - well before the onset of the Great Oxidation Event (GOE) at ~2.3-2.4 Ga (47, 48) - which has been identified using combined trace metal and nitrogen isotope datasets collected at high stratigraphic resolution (3, 5, 6). Exploration of other Meso- and Neoarchean records has revealed dynamic evolution of surface ocean redox conditions and oxidative continental weathering leading up to the permanent establishment of oxidizing conditions at Earth's surface (8, 10, 12–16, 44, 49–55). To further elucidate the dynamic redox landscape in the Neoarchean, we conducted a coupled survey of nitrogen and selenium isotopes and abundances at high stratigraphic resolution in two drill cores spanning a near shore-offshore transect across the ~2.66 Ga Jeerinah Formation in Western Australia. These complementary proxies allow us to assess the relative magnitude and spatial extent of redox fluctuations.

Nitrogen is essential for life as we know it and its biogeochemical behavior is highly redox-sensitive. Since at least 3.2 Ga, it is evident that the biosphere has exerted the primary control on Earth's surface nitrogen fluxes, regulating nitrogen availability and speciation in the ocean and atmosphere (28, 41). Metabolisms that drive nitrogen speciation in the ocean (transition of nitrogen among different redox states) can use a variety of electron donors for reduction such as organic

matter, Fe^{2+}, and sulfide, but for oxidation are primarily reliant on dissolved O_2 as an electron acceptor due to the high Eh of nitrate (38). Ammonium oxidation to nitrate can occur down to low nM oxygen concentrations (56, 57), which is a fraction of a percent of modern well-oxygenated ocean waters typically of 300 μM dissolved O_2. Thus, a significant pool of nitrate in an ancient ocean would suggest that at least minor amounts of oxygen were freely available to allow for nitrification: the biologically mediated conversion of ammonium to nitrite/nitrate.

Modern microbial metabolisms are known to have a diverse range of effects on the relative abundances of the nitrogen isotopes ^{14}N and ^{15}N (summarized in Table 1 of ref 38, 58, 59). For example, N_2 fixation using Mo-nitrogenase causes an insignificant isotopic fractionation during the conversion of N_2 to organic-bound nitrogen, but biological denitrification of NO_3^- to N_2 strongly prefers ^{14}N, producing isotopically light N_2 gas and an isotopically heavy residual dissolved NO_3^- pool. Hence nitrogen isotopes in ancient sedimentary rocks have allowed paleo-ecological interpretations of nitrogen metabolisms in ancient ecosystems. These interpretations are only semi-quantitative due to overlapping fractionation factors for different metabolic pathways and because of the potential for isotopic resetting by post-depositional alteration. Still, the presence of nitrate in concentrations high enough for significant bio-assimilation can be distinguished isotopically from anaerobic settings that are dominated by nitrogen fixation followed by proximal re-assimilation of liberated ammonium (3, 4, 23, 24, e.g. 28, 38, 41).

We also studied the behavior of selenium (Se) – a redox-sensitive element whose oxyanions are stable at similar redox potentials to nitrogen oxyanions – to determine whether changes in marine nitrogen cycling were concurrent with changes in weathering dynamics on land. Unlike nitrate, which is primarily produced during biomass remineralization and nitrification in the water column, Se oxyanions are mainly sourced from oxidative weathering on land (60).

Additionally, if Se fluxes are sufficiently large and oxygenated waters sufficiently widespread, Se isotopes can become fractionated during incomplete reduction of Se oxyanions (61). The nitrogen and selenium proxies combined can thus inform us about the loci of oxygenation.

3.3 *Geologic Setting*

As part of the Agouron Institute Drilling Project in 2012, two ultra-clean diamond drill cores AIDP-2 and AIDP-3 were sampled across the boundary between the Hamersley and Fortescue Groups in Western Australia. These holes were collared at 21°16'51"S 120°50'02"E (AIDP-2) and 21°46'32"S 117°34'11"E (AIDP-3) across a basinal depth gradient with AIDP-2 intersecting shallower near-shore facies and AIDP-3 deeper offshore facies. AIDP-2 consists of ~158 meters of the Carawine Dolomite that for this study was sampled at low stratigraphic resolution (SI Appendix, Figure 0.4), and ~128 meters of predominantly black shales from the Jeerinah Formation that were sampled at one-meter resolution. AIDP-3 is ~138 meters deep, capped by the basal Marra Mamba Iron Formation but with samples taken exclusively from the underlying Jeerinah Formation at one-meter resolution. The shallower depositional environment of AIDP-2 is indicated by the stromatolitic carbonates of Carawine Dolomite (62) and by the shoreface setting of the basal Woodiana Member of the Jeerinah Formation which consists of occasionally stromatolitic orthoquartzites (63). In contrast, AIDP-3 transects only a basinal banded iron formation and sulfidic kerogenous shales. The two holes can be stratigraphically correlated using a horizon of meteorite impact spherules (64), which occurs in a ~20 meter thick megabreccia towards the bottom of the Carawine Dolomite in AIDP-2 and in a 1 centimeter thick graded spherule layer in the upper Jeerinah Formation in AIDP-3 (SI Appendix, Figure 0.5). Rocks from both AIDP-2 and AIDP-3 are generally thought to be within the prehnite-pumpellyite metamorphic

facies (65) but an alternative upper greenschist facies interpretation exists (66). However, this latter interpretation is inconsistent with the pelitic mineralogy of the AIDP shales as key index minerals of upper greenschist conditions (e.g. biotite, chloritoid) are absent. Also, it depends upon a chlorite geothermometer (67) that (i) unjustifiably assumes all iron in the chlorite is Fe^{2+}, which can lead to temperature overestimations (68), and (ii) yields infeasibly broad temperature ranges (>140ºC) for samples in close stratigraphic proximity. Hence we favor the prehnite-pumpellyite metamorphic facies assignment (addressed further in the SI Appendix).

3.4 *Results*

Se abundances are tightly scattered around an average of 1.2 ± 1.1 ppm throughout both cores but a moderate excursion up to 5.4 ppm occurs around 363 m in AIDP-2. After normalizing the data to Al, TOC, and total sulfur (TS), the Se excursion in AIDP-2 still appears statistically significant (Figure 3.1B,C,D, and SI Appendix, Figure 0.6 and Figure 0.7). Multiple regression confirms this inference, showing that less than half of the observed Se enrichment can be explained by lithological variability (R^2 = 0.49; Figure 3.1B,C,D). $\delta^{82/78}$Se shows no systematic trend across either of the two cores (average +0.3 ± 0.3 ‰). In contrast, δ^{15}N displays a large range from -2‰ to +14‰ with systematic shifts detected by our linear regression model. This identified three distinct stages (I to III from oldest to youngest) in each core (Table 3.1). The only exception to the model boundary placement is the boundary between stage *I* and *II* in AIDP-3, where the boundary position was handpicked based on marked changes in TOC [%], TN [%], and C/N ratios [atomic]. Importantly, this boundary still falls within the range of stratigraphic positions where the model predicts a significant change in $\delta^{15}N_{bulk}$ values.

Table 3.1. **Stratigraphic stages of AIDP-2 and AIDP-3 with associated nitrogen and carbon measurements.** Stratigraphic stage boundaries were determined using the linear regression model described above. *C/N ratios are given as atomic ratios.

AIDP-2

Stage	Strat. [meters]	$\delta^{15}N_{bulk}$ [‰]	$\delta^{13}C_{org}$ [‰]	TN [%]	TOC [%]	C/N*	TIC [%]
III	344.18 - 278.75	+0.38 ± 0.61	-43.2 ± 2.5	0.08 ± 0.03	4.8 ± 2.3	81 ± 39	11.4 ± 4.4
II	377.89 - 344.99	+4.33 ± 0.53	-43.0 ± 1.9	0.12 ± 0.02	7.7 ± 2.4	74 ± 17	9.5 ± 2.5
I	428.16 - 380.37	+2.76 ± 0.71	-42.0 ± 1.5	0.04 ± 0.01	2.8 ± 0.8	95 ± 24	16.3 ± 4.9

AIDP-3

Stage	Strat. [meters]	$\delta^{15}N_{bulk}$ [‰]	$\delta^{13}C_{org}$ [‰]	TN [%]	TOC [%]	C/N*	TIC [%]
III	127.83 - 66.03	+2.39 ± 0.86	-41.7 ± 1.5	0.06 ± 0.02	5.8 ± 2.4	109 ± 32	12.1 ± 8.6
II	155.75 - 129.65	+6.07 ± 0.36	-41.7 ± 1.0	0.06 ± 0.01	4.7 ± 0.7	85 ± 14	15.0 ± 3.0
I	204.37 - 156.89	+10.2 ± 2.14	-44.2 ± 0.9	0.02 ± 0.02	2.4 ± 2.1	156 ± 63	14.7 ± 2.9

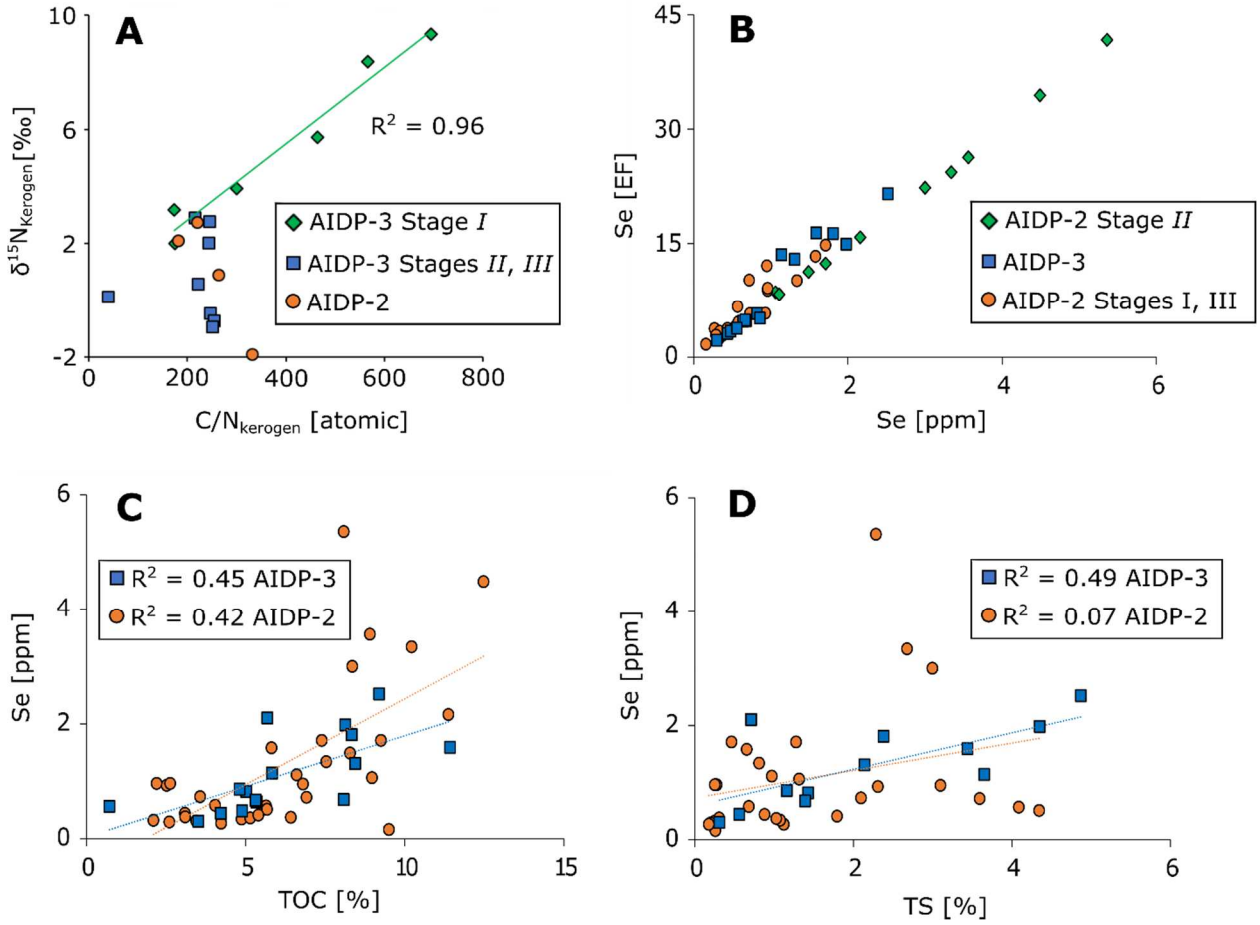

Figure 3.1**. Crossplots of A) $\delta^{15}N_{kerogen}$ values and C/N ratios, B) Se enrichment factor [EF] and Se [ppm], C) Se [ppm] and TOC [%], and D) Se [ppm] and total sulfur [TS %].** For (A) Note the linear covariance in AIDP-3 stage *I* compared to the rest of the core. Samples from AIDP-2 come from all stages. For (B) the procedure for calculating EF is described in the SI Appendix. Note the particularly strong enrichments in AIDP-2 Stage *II*. Samples from AIDP-3 come from all stages. For (C and D) Note the weaker correlations in AIDP-2 compared to AIDP-3. The variation (and so the increase) in selenium abundance in AIDP-2 cannot be explained through variations in TOC and TS. Conversely, much of the variation in selenium abundance in AIDP-3 can be explained by variations in TOC and TS. This suggests the increase in Se during stage *II* of AIDP-2 is likely caused by an increased flux of Se to the basin.

3.4.1 *AIDP-2*

Stage *I* in AIDP-2 is characterized by the most variable $\delta^{15}N_{bulk}$ values in the core, averaging around +2.8‰. In this stage TOC [%] and TN [%] are at their lowest. From stage *I* to stage *II* $\delta^{15}N_{bulk}$ suddenly increase by an average of ~1.5‰ to the highest values recorded in the core (+5.43‰) and become less variable. This rise in $\delta^{15}N_{bulk}$ values is associated with increases in both TOC [%] and TN [%] by about a factor of 3. From stage *II* to stage *III* $\delta^{15}N_{bulk}$ values decrease by 4‰ on average to a minimum of -0.71‰. TOC [%] and TN [%] also decrease across this transition, but not to levels as low as in stage *I*. $\delta^{15}N_{kerogen}$ values are systematically lower than $\delta^{15}N_{bulk}$ measurements throughout the core by an average of 1.6‰ ± 0.9‰, and so show the same general trend as $\delta^{15}N_{bulk}$ values across all three stages (Figure 3.2).

3.4.2 *AIDP-3*

Stage *I* in AIDP-3 has the most positive and variable $\delta^{15}N_{bulk}$ values and C/N [atomic] ratios in either core, averaging +11.0‰ and 174 respectively. Notably, in this same stage, TOC [%] and TN [%] averages are the lowest in either core. Across the boundary between stages *I* and *II*, $\delta^{15}N_{bulk}$ values decrease by 5‰ on average (Figure 3.3). TOC [%] and TN [%] values both increase by over a factor of 3, and C/N [atomic] ratios decrease to an average similar to all stages apart from stage *I* of AIDP-3. The transition from stage *II* to stage *III* is defined by another decrease in $\delta^{15}N_{bulk}$ of about 4‰ on average, similar to the stage *II-III* transition in AIDP-2. TOC [%], TN [%], and C/N ratios [atomic] do not change significantly from stage *II* to stage *III*.

Like AIDP-2, in AIDP-3 $\delta^{15}N_{kerogen}$ values are systematically lower than $\delta^{15}N_{bulk}$. Whereas the average difference between the two measurements is consistent throughout AIDP-2, in AIDP-3 it varies in a stepwise fashion throughout the core; the smallest differences are in stage *III* and

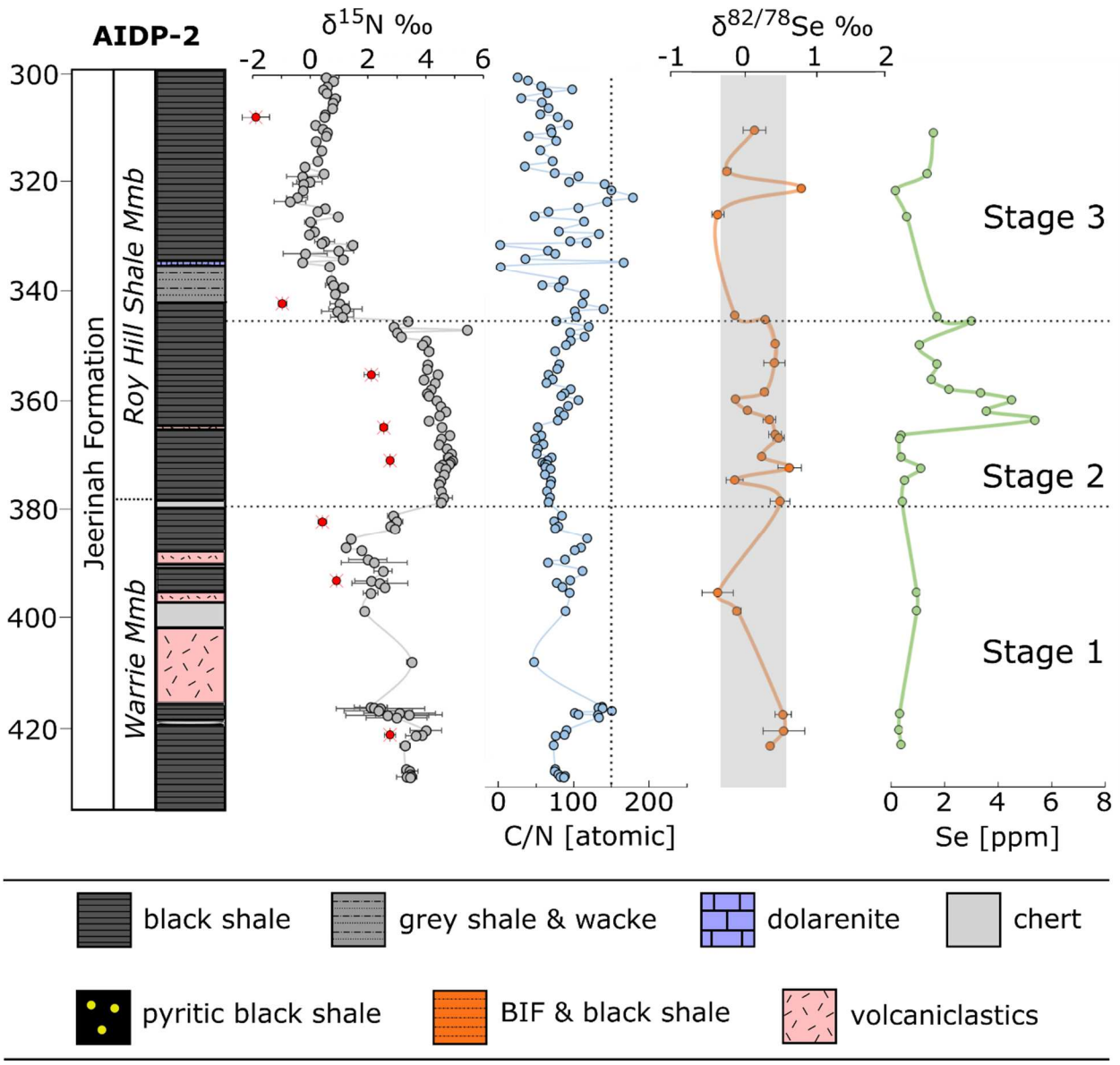

Figure 3.2**. Chemostratigraphy of AIDP-2 showing $\delta^{15}N_{bulk}$ (grey dots), $\delta^{15}N_{kerogen}$ (red dots), C/N ratios, $\delta^{82/78}Se$, and Se concentrations.** Stages are delineated by horizontal dotted lines. Shaded area for $\delta^{82/78}Se$ represents crustal values. Down-core depth is given in meters.

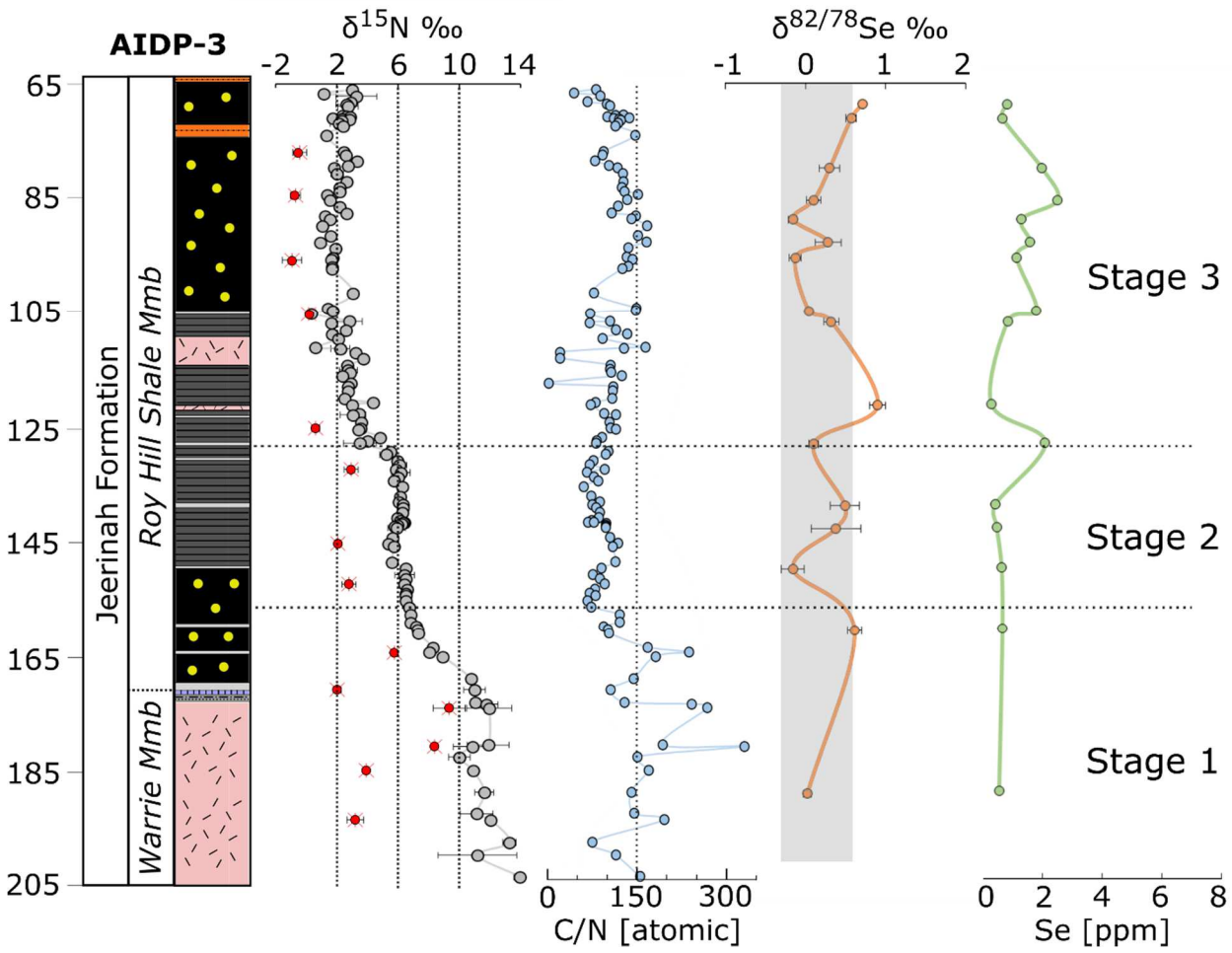

Figure 3.3. **Chemostratigraphy of AIDP-3 showing $\delta^{15}N_{bulk}$ (grey dots), $\delta^{15}N_{kerogen}$ (red dots), C/N ratios, $\delta^{82/78}Se$, and Se concentrations.** Stages are delineated by horizontal dotted lines. Lithological symbols follow the Figure 3.2 legend. Note the different $\delta^{15}N$ and C/N scales between AIDP-2 and AIDP-3, required to accommodate Stage I of AIDP-3. Shaded area for $\delta^{82/78}Se$ represents crustal values. Down-core depth is given in meters.

the largest are in stage *I*. A noteworthy relationship in stage *I* is that $\delta^{15}N_{kerogen}$ values correlate strongly with atomic $C/N_{kerogen}$ and C/N_{bulk} ratios (Figure 3.1A). This is not the case in stages *II* and *III*, and all of AIDP-2.

3.5 *Discussion*

3.5.1 *Proxy Alteration*

Post-depositional processes such as diagenesis and metamorphism have the potential to alter the primary nitrogen and Se isotopic signals preserved in sedimentary rocks. For example, Se isotope fractionation could potentially occur during diagenetic oxyanion reduction. However, this would require the presence of a stable Se oxyanion reservoir in the overlying water column, which would in turn imply oxic conditions. Such diagenetic Se reactions would therefore strengthen environmental redox signals. During metamorphism, Se is fairly immobile (69), and so its isotopic ratios are unlikely to be altered. Nitrogen isotopes, on the other hand, can undergo more significant alteration during diagenesis and metamorphism (29). The $\delta^{15}N$ of sinking and sediment biomass can increase during early diagenesis under oxic conditions through the preferential remineralization, oxidation, and loss of ^{14}N (common in modern marine settings), but is less susceptible to alteration under the mainly anoxic bottom waters/sediments (31, 33, 34) characteristic of the Neoarchean. It is possible that for samples with initially positive $\delta^{15}N_{bulk}$ values, early diagenesis under anoxic conditions can decrease $\delta^{15}N_{bulk}$ values by the addition of isotopically light ($\delta^{15}N$ of -2‰ to +1‰) biomass via the in-situ growth of nitrogen-fixing bacteria; samples that have a primary $\delta^{15}N_{bulk}$ signal around 0‰ would not be significantly affected by this mechanism (32, 35, 36). Primary $\delta^{15}N$ values may also decrease by the preferential deamination of ^{15}N-enriched organic compounds such as proteins (32). Even if more relevant in the Neoarchean,

neither of these mechanisms can fully account for the shifts in $\delta^{15}N_{bulk}$ values of up to 4‰ between stages in both cores, nor would they affect our interpretations regarding episodes of enriched $\delta^{15}N$ values.

Anoxic diagenesis may lead to small isotopic differences between the kerogen and silicate nitrogen fractions and even smaller isotopic changes in bulk rock measurements, but metamorphism/metasomatism can lead to greater isotopic disparity and changes that are not always predictable (e.g. 70, 71). Below greenschist facies, such thermal effects can lead to changes in the primary nitrogen isotopic signal of bulk rocks by 1-2‰ (29). As previously mentioned, the Carawine Dolomite and Jeerinah Formation were likely metamorphosed to prehnite-pumpellyite grade (65), and so may have been subject to these small changes to the primary $\delta^{15}N$ values. As metamorphic grade and metasomatic alteration increases, so does the difference in $\delta^{15}N$ between bulk rock and kerogen fractions, which may reach up to 13‰ (72).

To test if metamorphism/metasomatism has affected our samples, we considered the relationship between $\delta^{15}N$ values and C/N ratios, as well as the difference in $\delta^{15}N$ values between the two nitrogen fractions (kerogen and silicate). If thermal processes have significantly affected our samples, increasing $\delta^{15}N$ values should correspond to increasing C/N ratios as nitrogen is more mobile than carbon and ^{14}N is more mobile than ^{15}N under such conditions. The only samples that show this relationship come from stage 1 in AIDP-3 (Figure 3.1A). This is also the stage where the differences in $\delta^{15}N$ values between the two nitrogen fractions are the greatest and most variable. Because of this, stage 1 of AIDP-3 evidently displays a secondary isotopic signal due to thermal alteration. This most likely had a metasomatic component, as the kerogen samples are not persistently more altered (higher C/N and $\delta^{15}N$) with stratigraphic depth but show local variability that could have resulted from focused fluid-rock interactions. This is consistent with previous

observations that underlying basalt units locally experienced metasomatic alteration (73). Indeed, the basalt underlying the Jeerinah Fm in AIDP-3 has metamorphic/metasomatic textures including zones of K-feldspar spherulites, veins and amygdales filled with chlorite, calcite, silica, and patches of sericitization, all indicating multiple periods of metasomatic alteration (SI Appendix, Figure 0.8a-h). Because all samples from AIDP-2 and from stages II and III of AIDP-3 lack petrographic and geochemical signs of significant thermal alteration, the $\delta^{15}N$ values from these stages are interpreted to be close to primary compositions.

3.5.2 *Interpretation of nitrogen isotopic data*

$\delta^{15}N$ values between -2‰ and +1‰, as seen in AIDP-2 Stage III, are generally interpreted to reflect marine nitrogen cycling dominated by nitrogen fixation using Mo-nitrogenase (37). Elevated $\delta^{15}N$ values >+1‰, as in all other stages, can be interpreted in one of three ways (e.g. 23, 24) (SI Appendix, Figure 0.9): (i) Partial bio-assimilation from a dissolved NH_4^+ pool that would preferentially remove ^{14}N, locally creating isotopically light biomass and an isotopically heavy residual NH_4^+ pool. If this heavy residual pool were transported to another location in the basin, it could be fully assimilated and biomass there would record isotopically heavy $\delta^{15}N$ values (74). However, because AIDP-2 (shallow) and AIDP-3 (deep) represent a broad cross-basinal transect and no corresponding isotopically light values (<-2‰) were encountered anywhere, there is no evidence to suggest that this process was responsible for the heavy $\delta^{15}N$ values in either core. (ii) Partial nitrification of an ammonium pool that preferentially selected ^{14}N followed by quantitative denitrification of the resulting nitrate would leave the residual ammonium isotopically heavy. Bio-assimilation from this ammonium pool would result in isotopically heavy biomass (75). (iii) Quantitative nitrification of an ammonium pool followed by partial denitrification of the resulting

nitrate pool that preferentially removed ^{14}N would leave residual nitrate isotopically enriched in ^{15}N (3, 4). Assimilation of this heavy nitrate pool would yield $\delta^{15}N$-enriched biomass. This mechanism is largely responsible for the enriched $\delta^{15}N$ values of nitrate in the modern deep ocean that are spatially heterogeneous (ranging from +2‰ to +20‰) but show an average around +5‰ (76). The lack of very light $\delta^{15}N$ values suggests that mechanisms (ii) or (iii), both requiring free O_2 for nitrification, best explain our data. Mechanism (ii) should yield highly variable $\delta^{15}N$ values because it lacks an isotopically heavy nitrogen sink from the ocean (24), but such variability is not seen in most of the AIDP stages. We thus propose that mechanism (iii) probably prevailed. In either case, the isotopically enriched nitrogen data require oxic conditions in marine surface waters.

3.5.3 *Interpretation of selenium concentrations and isotopic ratios*

The extent of oxygenation can be further elucidated using Se isotopes and abundances. The peak in Se abundances during Stage II of the AIDP-2 core may reflect (i) enhanced oxidative terrestrial weathering, or (ii) enhanced delivery of volcanically derived SeO_2. We cannot definitively rule out a volcanic Se source for the Se enrichment in AIDP-2, as the volcanic flux of Se to marine environments may have been comparable to, or greater than, the Se flux from oxidative weathering under low O_2 conditions (60). We would, however, expect that such an event should have been more uniformly distributed across the basin and recorded in AIDP-3. As AIDP-3 does not show any significant Se enrichment, our data are perhaps more consistent with a small fluvial Se influx that was sequestered near-shore under dominantly anoxic bottom waters. In any case, the <6 ppm Se enrichment is noticeably smaller than that during the 2.50 Ga "whiff" of oxygen recorded in the Mt McRae Shale (5), where Se abundances reach 20 ppm. This difference

suggests that the Se flux to the ocean was considerably less during the Jeerinah oxygenation event. This conclusion is further supported by the Jeerinah Se isotopic data which nearly all fall within the crustal range (-0.3 to +0.6‰; ref 77) indicating that any Se oxyanion reservoir was small and nearly quantitatively sequestered in near-shore environments, unlike the Mt McRae Shale which shows a marked positive excursion in $\delta^{82/78}$Se to +1.4‰ (5). So, while the nitrogen data are comparable between the two events, the Se data suggest that the magnitude of oxidative weathering was smaller at 2.66 Ga than at 2.50 Ga.

3.5.4 *Transient surface ocean oxygenation in the Neoarchean: mode and tempo*

A transient enrichment in Archean sedimentary δ^{15}N at 2.5 Ga has previously been linked to an oxygen "whiff" before the GOE (3), and this AIDP dataset extends such evidence for surface ocean oxygenation back by ~160 Ma. Godfrey & Falkowski (4) previously reported several elevated δ^{15}N measurements from a roughly coeval section in the Transvaal Supergroup in South Africa sampled at coarse stratigraphic resolution, which are also consistent with aerobic nitrogen cycling in the surface ocean. However, the δ^{15}N data presented here show that surface ocean oxygenation was a transient phenomenon lasting 50 Myr or less (see text below for calculations). It also provides direct evidence that this episode of late Archean oxygenation extended over hundreds of kilometers, with surface waters evidently holding nM to μM concentrations of dissolved O_2 allowing widespread nitrification (56, 57), as previously predicted (78).

The mode of oxygenation cannot be resolved using nitrogen isotopes alone. Aerobic nitrogen cycling requires bioavailable trace metals such as Mo, Cu, and Fe along with free O_2 and dissolved NH_4^+, and it is not clear which was limiting before and after stage II. Surface ocean oxygenation could have been a purely oceanographic event driven by changes in upwelling that

delivered nutrients like Fe and NH_4^+ to the photic zone stimulating cyanobacterial productivity (78). Alternatively, mild oxidative weathering on land during stage II could have supplied bioessential trace metals to basin surface waters without supplying much Se, due to its high Eh. This could have resulted from localized oxidative weathering beneath non-marine cyanobacterial mats, hypothesized to have been significant before the GOE (79), or from a small global pulse in atmospheric oxygen levels. If cyanobacteria and nitrifiers were trace metal limited (80, 81), either mechanism would spur regional oxygen production allowing free O_2 and NO_3^- to accumulate in the photic zone. Both are consistent with the positive $\delta^{15}N$ values in stage *II* of the two cores, as well as the observed Se enrichment in AIDP-2.

If the Se enrichment in AIDP-2 were due to weak oxidative weathering of continental material (our preferred interpretation) then oxygenation of the surface ocean and mobilization of Se oxyanions were out of phase, as indicated by the $\delta^{15}N$ and [Se] values. Regardless of whether surface ocean oxygenation resulted from delivery of nutrients by upwelling or oxidative weathering, the Se peak could indicate a period of more vigorous oxidative continental weathering, but not to the extent of the 2.5 Ga Mt McRae "whiff". The occurrence of similarly positive nitrogen isotope values in rocks of similar age from South Africa indicates that surface oceanic oxygenation leading to aerobic nitrogen cycling (4) may have been relatively widespread at this time. Fluctuating balances between atmospheric O_2 sources and sinks could have led to transient increases in atmospheric O_2 of various magnitudes, consistent with a more global positive $\delta^{15}N$ signal and the Se enrichment. Alternatively, terrestrial cyanobacterial mat proliferation under a transient organic haze (43, 44, 82) providing temporary UV protection (83) may have increased the oxidative weathering flux of Se, but the feedback between O_2 generation, aerobic methane oxidation, and haze formation needs to be explored in greater detail.

As mass independent fractionation of sulfur isotopes is persistent throughout the Jeerinah Fm (84, 85), any atmospheric oxygenation event could have only been of limited magnitude. The duration of the $\delta^{15}N$ excursion in AIDP-2, covering ~35 meters of shale deposition, suggests that the shifting balance between O_2 sources and sinks driving oxygenation would have operated on a geologically rapid (< 50 Myr) timescale[4]. As the Se abundance excursion is even more stratigraphically restricted (<20 meters), any interval of atmospheric oxygenation would have been proportionately shorter.

The $\delta^{15}N$ data also clearly indicate that the microbial metabolisms of nitrification and denitrification had already evolved by ~2.66 Ga (SI Appendix, Figure 0.10), confirming the few data points previously reported from similarly ancient rocks from South Africa (4). Both nitrification and denitrification are complex pathways involving many redox steps utilizing multiple metalloenzymes, which on the modern Earth are typically mediated by microbial consortia or, in rare cases, by individual microbial taxa (88, 89). This implies that, by the mid-Neoarchean, microbes had developed either evolutionary or ecological sophistication comparable to their modern counterparts.

3.6 *Conclusion*

The data presented here record a second Archean event characterized by transient oxygenation of the surface ocean. While the nitrogen isotopic signal is similar in magnitude to the 2.50 Ga Mt. McRae "whiff" of oxygen, the Jeerinah event shows a smaller selenium enrichment

[4] The top and bottom of the Jeerinah Formation are dated to 2.629±5 (86) and 2.684±6 (87) respectively (differences of 44 Ma minimum and 66 Ma maximum). The positive $\delta^{15}N$ values in stage II occur in ~30m of black shale in the middle of the Jeerinah in both cores, accounting for < 25% of the formation's total thickness. It is therefore likely that oxygenation occurred on a timescale perhaps much less than 50 Ma, assuming similar deposition rates between the two sections.

and no isotopic excursion in $\delta^{82/78}$Se, suggesting that terrestrial oxidative weathering was weaker during this earlier episode. When viewed at high resolution, these data show that oxygenated surface waters both preceded and post-dated the oxidative weathering signal of selenium, perhaps indicating that local production of oxygen eventually enabled more vigorous sulfide dissolution on land. These results highlight the variability in mechanisms and magnitudes of Neoarchean oxygen fluctuations and demonstrate the importance of feedbacks between biogenic oxygen production, oxidative weathering, and nutrient fluxes during the prelude to the permanent oxygenation of Earth's surface environment.

3.7 *Methods*

Sample preparation and analytical procedures for bulk rock analyses of nitrogen isotopes followed the methodology outlined in (24, 25) and Se abundances and isotopes were determined using the protocol described in (90); for details see the SI Appendix. The linear regression model used to identify the stratigraphic location of significant shifts in $\delta^{15}N_{bulk}$ followed the methodology reported in (91), and is described in greater detail in the SI Appendix.

3.8 *Acknowledgements*

We thank the Agouron Institute, John Abelson and Melvin Simon for funding the drilling of AIDP-2 and AIDP-3, NASA grant NNX16AI37G and NSF FESD grant 338810 to R.B. for funding the analyses, NSF Graduate Research Fellowship funding to M.A.K. and J.Z., and U.W. ESS Departmental Awards to M.C.K. for other support. We thank the U.W. Isolab, the U.W. non-traditional isotope laboratory, Andy Schauer, Scott Kuehner, Bruce Nelson, and Fang-Zhen Teng

for technical support. We also thank Chad Ostrander, Mou Roy, and the Anbar lab at ASU for the aluminum data, as well as Iadviga Zhelezinskaia and Jay Kaufman for the sulfur data.

Chapter 4: SPATIAL AND TEMPORAL TRENDS IN PRECAMBRIAN NITROGEN CYCLING: A MESOPROTEROZOIC OFFSHORE NITRATE MINIMUM

This manuscript is published in the journal *Geochimica Cosmochimica Acta*
Co-authored by Matthew C. Koehler, Eva E. Stüeken, Michael A. Kipp, Roger Buick, and Andrew H. Knoll

4.1 *Abstract*

Fixed nitrogen is an essential nutrient for eukaryotes. As N_2 fixation and assimilation of nitrate are catalyzed by metalloenzymes, it has been hypothesized that in Mesoproterozoic oceans nitrate was limited in offshore environments by low trace metal concentrations and high rates of denitrification in anoxic and episodically euxinic deep water masses, restricting eukaryotes to near-shore environments and limiting their evolutionary innovation. To date this hypothesis has only been tested in the Belt Supergroup (~1.4 Ga), with results that support an onshore-offshore nitrate gradient as a potential control on eukaryote ecology. Here we present bulk nitrogen and organic carbon isotopic data from non-isochronous cross-basinal facies across the Bangemall (~1.5 Ga) and the Roper (~1.4-1.5 Ga) basins to better understand the extent and variability of onshore-offshore nitrogen isotope gradients in the Mesoproterozoic. Both basins show an average ~1-2‰ enrichment in $\delta^{15}N_{bulk}$ from deep to shallow facies, with a maximum range from -1‰ offshore to +7.5‰ onshore. Unlike the Belt basin, the Bangemall and Roper basins show some offshore $\delta^{15}N_{bulk}$ values that are enriched beyond the isotopic range induced by biological N_2 fixation alone. This suggests a mixture of aerobic and anaerobic metabolisms offshore. In shallow waters, where $\delta^{15}N_{bulk}$ enrichment peaks, an aerobic nitrogen cycle was evidently operating vigorously. Even though isotopic signatures of aerobic nitrogen cycling are seen in all parts of the Bangemall and

Roper basins, our data are consistent with a lateral gradient in nitrate availability within the photic zone, with higher concentrations in near-shore environments than offshore. The variability in $\delta^{15}N_{bulk}$ values in each depositional environment and the consistently low $\delta^{15}N$ values from Mesoproterozoic units compared to the Paleoproterozoic and Neoproterozoic suggest that nitrate concentrations in the global ocean were likely low. This trend is now seen in all three Mesoproterozoic basins so far examined, and contrasts with the Paleoproterozoic and Neoproterozoic where nearly all $\delta^{15}N_{bulk}$ data plot above the N_2 fixation window. Thus, we propose that the Mesoproterozoic ocean was characterized by a nitrate minimum between the Paleo- and Neoproterozoic, with the lowest concentrations in offshore environments. This inference is consistent with a Mesoproterozoic O_2 decline following a temporary Paleoproterozoic O_2 peak, and it further supports the idea that nitrate limitation offshore may have contributed to the restriction of photosynthetic eukaryotes to near-shore environments, delaying their rise to ecological dominance until the Neoproterozoic Era.

4.2 *Introduction*

Fixed nitrogen, including nitrate and ammonium, is an essential nutrient for eukaryotes. Its scarcity under certain oceanic redox and chemical conditions may have exerted spatial control on eukaryotic diversity and abundance to such an extent (92) that it repressed the evolutionary radiation of eukaryotic primary producers prior to the Neoproterozoic "second rise of oxygen." Consistent with this hypothesis, Javaux *et al.,* (93) found that eukaryotic microfossil diversity and abundance in the Mesoproterozoic Roper basin were greater in marine marginal and inner shelf environments than in outer shelf and basinal settings. Buick and Knoll (94) found a similar trend in acritarchs and prokaryotic microfossils in the Mesoproterozoic Bangemall basin, noting a

decrease in taxonomic diversity and numerical abundance offshore. Contemporaneous with these observed microfossil trends are geochemical data in the form of iron-sulfur systematics, Mo and Cr abundances, and sulfur isotopic ratios that suggest that the Mesoproterozoic ocean was characterized by more widespread anoxia and notably more euxinia than any other time after the Great Oxidation Event (95–100). In fact, Fe-S systematics and $\delta^{34}S$ measurements throughout the Roper Group suggest inner and distal shelf depositional environments were likely oxic, while basinal shales record prolonged periods of euxinia (99). Trace metal concentrations from the same basinal shales corroborate basinal anoxia with extended periods of euxinia, but overlying surface waters were likely at least transiently oxic (Cox *et al.,* 2016). The "bioinorganic bridge hypothesis" (92) links these micropaleontological and geochemical observations, as follows:

- Biological N_2 fixation and assimilation of nitrate are catalyzed by metalloenzymes that contain siderophile or chalcophile elements in their active sites (101).
- During the Mesoproterozoic Era, when the ocean had relatively widespread euxinia (96, 98, 100), N_2 fixation could have been limited in offshore environments by low trace metal concentrations, in particular Mo, due to their incorporation into precipitating sulfide minerals (92).
- This may have restricted photosynthetic eukaryotes to near-shore environments as suggested by microfossil evidence, prompting ecological subordination to cyanobacteria and, as a result, limiting evolutionary diversification (92).

But does this elegant theoretical scenario stand up to the constraints provided by empirical geochemical data? In an initial study, Stüeken (24) examined nitrogen isotopic ratios along a cross-basinal transect in the Mesoproterozoic Belt Supergroup, USA, and found that $\delta^{15}N_{bulk}$ values changed markedly from ~0‰ basinward to ~+5‰ near-shore. This was interpreted as indicating

a gradient from an anaerobic system dominated by N_2 fixation in the open ocean to aerobic nitrogen cycling involving nitrification coupled to partial denitrification in shallow settings. Although ammonium may have been present in the deeper water column in offshore waters, as in the modern Black Sea (102), the availability of fixed nitrogen of any form was probably low in the photic zone away from coastal areas (24). This would have been biologically significant, because in the modern ocean cyanobacterial phytoplankton commonly outcompete their eukaryotic counterparts where fixed nitrogen is scarce, because (a) only prokaryotes can fix atmospheric N_2 and (b) organisms with smaller cells have a lower nutrient requirement (103–107). Also, in modern oceans, the infiltration of phytoplankton biomass by larger cells occurs when total rates of primary production increase and grazing comes to limit production by smaller cells (108); thus, small cyanobacterial cells would be expected to dominate in off-shore, nutrient-limited environments.

Stüeken (24), however, examined only one sedimentary basin, which may not have been typical of global oceans at that time. Here we report nitrogen abundance and isotopic data from two additional basins of roughly equivalent age, the Bangemall (~1.5 Ga) and Roper (~1.5-1.4 Ga) basins of western and northern Australia, respectively. Although cross-basinal transects are not available, stratigraphic profiles through multiple sedimentary sequences provide samples of deep subtidal, shallow subtidal and peritidal facies, allowing offshore-onshore comparisons of relative nitrogen availability and speciation. Thus, they can indicate whether a nitrate constraint on eukaryotic evolution was just a local phenomenon, or more likely a global feature during the Mesoproterozoic.

4.3 *Precambrian nitrogen cycling*

Nitrogen cycling has been predominantly controlled by the biosphere since the advent of biological N_2 fixation no later than 3.2 billion years ago (41), but it has also been influenced by changes in atmospheric and oceanic redox states. For example, the appearance of free O_2 as early as 2.8 Ga (reviewed by 109) in microbial mats and marine surface waters (78, 79) probably spurred the radiation of nitrifying bacteria (4) because locally enhanced crustal weathering (6, 10, 50, 51, 54, 55, 110, 111) would have led to a greater influx of trace metals such as Fe, Cu, and Mo. Higher O_2 levels combined with increasing micro-nutrient availability would have facilitated the oxidation of ammonium to nitrite and nitrate (101, reviewed by 112). Complementary denitrifying bacteria would have been stimulated by the resulting supply of nitrate (3, 4). The extent of these coupled oxic-suboxic processes can be inferred from the sedimentary record, because they impart a distinct kinetic fractionation on the nitrogen isotopes of organic matter compared to those imparted by strictly anaerobic nitrogen cycling (Table 4.2).

Heavy $\delta^{15}N$[(5)] values, greater than those produced by biological N_2 fixation alone and thus interpreted to represent aerobic nitrogen cycling, are known from the late Archean and early Paleoproterozoic before the Great Oxidation Event (3, 4, 113, 114), and from the later Paleoproterozoic (72, 115), *i.e.* during and shortly after the proposed O_2 overshoot at 2.3-2.0 Ga (47, 116–119) (Figure 4.1). This suggests that surface waters at these times contained enough dissolved oxygen to form significant amounts of nitrate, which was then partially denitrified in the water column and assimilated into biomass. Moreover, isotopic profiles from cross-basinal facies show no trends (4, 72), indicating that nitrate was available in the most productive zone of the

[(5)] $\delta^{15}N = [(^{15}N/^{14}N)_{sample} / (^{15}N/^{14}N)_{standard} - 1] \cdot 1000$, where the standard is atmospheric N_2.

Table 4.2. **List of nitrogen cycle steps that induce large isotope fractionation effects and their respective fractionation factors**. Fractionations are expressed as $\delta^{15}N_{substrate} - \delta^{15}N_{product}$. References: 1.Zhang *et al.* (37), 2. Casciotti (58); 3. Frey *et al.* (120); 4. Brunner *et al.* (121); 5. Fulton *et al.* (122); 6. Fuchsman *et al.* (102); 7. Altabet & Francois (31); 8. Kessler *et al.* (123); 9. Sigman *et al.* (124).

Nitrogen cycle reaction	**Fractionation factor**	**Ref.**	**Preservation potential**
Nitrogen Fixation ($N_2 \rightarrow N_{org} \rightarrow NH_4^+$)	Mo-nitrogenase: +2‰ to -1‰ Fe- and V- nitrogenase: +6‰ to +8‰	1	Preserved in sediments from nitrogen-limited ecosystems [5]
Ammonium assimilation ($NH_4^+ \rightarrow R\text{-}NH_2$)	+14‰ to +27‰	2	Not known to be expressed [cf. 5] (Section 4.7.3)
Nitrification (ammonium oxidation) ($NH_4^+ \rightarrow NO_2^-$)	+14‰ to +38‰	2	Quantitative at chemocline [6]; not preserved
Nitrification (nitrite oxidation) ($NO_2^- \rightarrow NO_3^-$)	-12.8‰	2	Quantitative at chemocline [6]; not preserved
Nitrate assimilation ($NO_3^- \rightarrow R\text{-}NH_2$)	+5‰ to +10‰	2	Usually quantitative in photic zone [7]; not preserved
Denitrification ($NO_3^- \rightarrow N_2$)	+10‰ to +30‰	3	Non-quantitative in suboxia [8, 9]; preserved in biomass of NO_3^- assimilators [7]
Annamox ($NO_2^- + NH_4^+ \rightarrow N_2 + 2H_2O$)	NO_2^-: +16‰ NH_4^+: +23‰ to +29‰	4	Probably indistinguishable from denitrification [4]

water column in both on-shore and offshore settings. Similar patterns are also evident across Neoproterozoic basins (125).

Nitrogen cycling in the Mesoproterozoic, however, was potentially quite different from any other time in Earth's history. It has been predicted that the expansion of euxinic waters after 1.8 Ga (95, 96) would have led to the scavenging of trace metals such as Mo, Cu, and Fe from seawater into sediments by organic compounds or low-temperature sulfide mineral phases (98, 126), restricting their availability for use as metal cofactors in aerobic nitrogen cycle reactions (92, 112). For example, Mo concentrations may have been as low as 1-10 nM compared to 105 nM today (98), which may have limited biological N_2 fixation and nitrate assimilation (127, 128). This may in turn have delayed the radiation of photosynthetic eukaryotes, which are most productive under a steady supply of nitrate and are incapable of N_2 fixation (92). Nitrate scarcity could have created a positive feedback on trace metal scavenging because it may have spurred microbial sulfate reduction and consequently the expansion of euxinic environments (129). This would have prolonged nitrate limitation until the extent of euxinia contracted (100) possibly through a Neoproterozoic expansion of oxic waters (125, 130, 131). For these reasons, much of the Mesoproterozoic ocean may have been unsuitable for eukaryotic life.

Consistent with this idea, the Mesoproterozoic Belt basin displays a distinct onshore-offshore gradient in nitrogen isotopes (24). This trend was interpreted to represent a trend in nitrogen speciation, where nitrate was only available in near-shore environments while an anaerobic nitrogen cycle dominated by N_2 fixation prevailed offshore. A decrease in dissolved oxygen concentration and/or bioessential trace metals in offshore environments probably restricted nitrification to shallow waters (24). Any nitrate that was produced offshore was likely consumed rapidly and quantitatively at the chemocline.

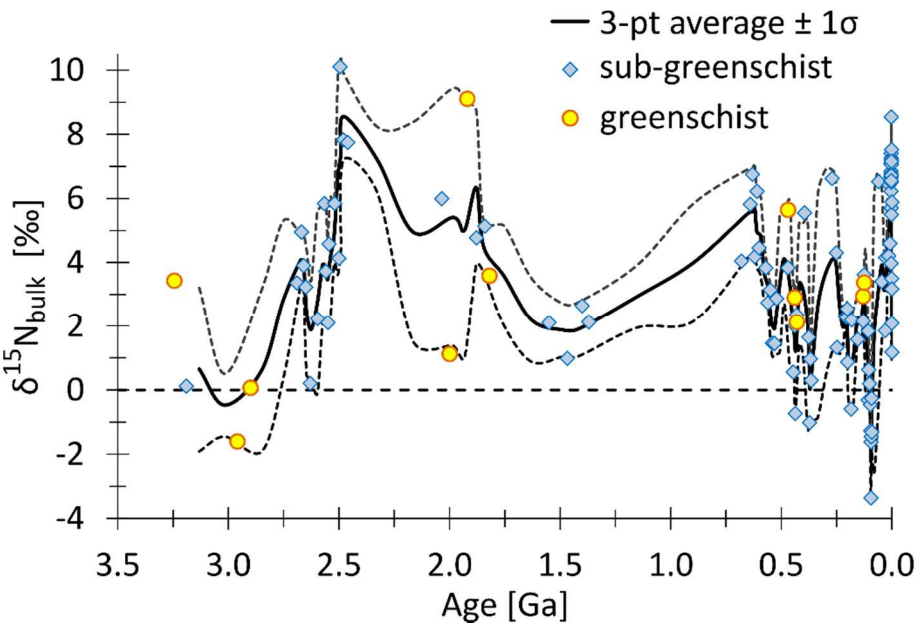

Figure 4.1**. Average nitrogen isotopic composition of bulk marine sedimentary rocks from offshore environments.** Data are compiled from the literature (see (41) for references) and from this study. Each point represents a time-point average, the black solid line marks the running mean over three points. Where no basinal gradient is present, all data were used. Samples from hydrothermal cherts and amphibolite facies were excluded.

4.4 *Location and geologic setting*

4.4.1 *Bangemall Supergroup*

The Bangemall Supergroup crops out over ~100,000 km^2 in northwestern Australia (Figure 4.2). Our samples predominantly come from three stratigraphic transects spread over 100 km along the Pingandy Shelf which forms the northern limb of the broad synclinorium in which the Supergroup is now exposed: from west to east Irregully Creek, Wandarry Creek and Fords Creek. These spanned almost the entire ~5 km section of the Edmund and Collier Groups, the components of the Supergroup preserved in this region. They largely consist of terrigenous mudrocks and sandstones with subordinate carbonates, cherts and conglomerates. Because of their broad outcrop area and facies relationships, they have been interpreted as entirely (Edmund Group) or dominantly (Collier Group) marine (132). Though parts of the Bangemall basin may have been restricted from the open ocean, the Pingandy Shelf, from where the great majority of our samples come, was evidently a long-lived basement high with variable paleo-current patterns (132, 133) suggesting that it was not an isolated and restricted sub-basin. On the Pingandy Shelf, deformation has been modest with only broad open folding during the Mutherbukin Tectonic Event, the Edmundian Orogeny, and the Mulka Tectonic Event (134). Several episodes of dolerite sill intrusion occurred during the Mesoproterozoic, causing local contact metamorphism of siliceous dolomites to talc-tremolite-calcite assemblages in aureoles about 100 meters across (135). Otherwise metamorphism has been insignificant with kerogen color grading from orange-brown in the east to mid-brown in the west indicating a temperature gradient from 100-125°C to ~150°C towards the western closure of the synclinorium (94).

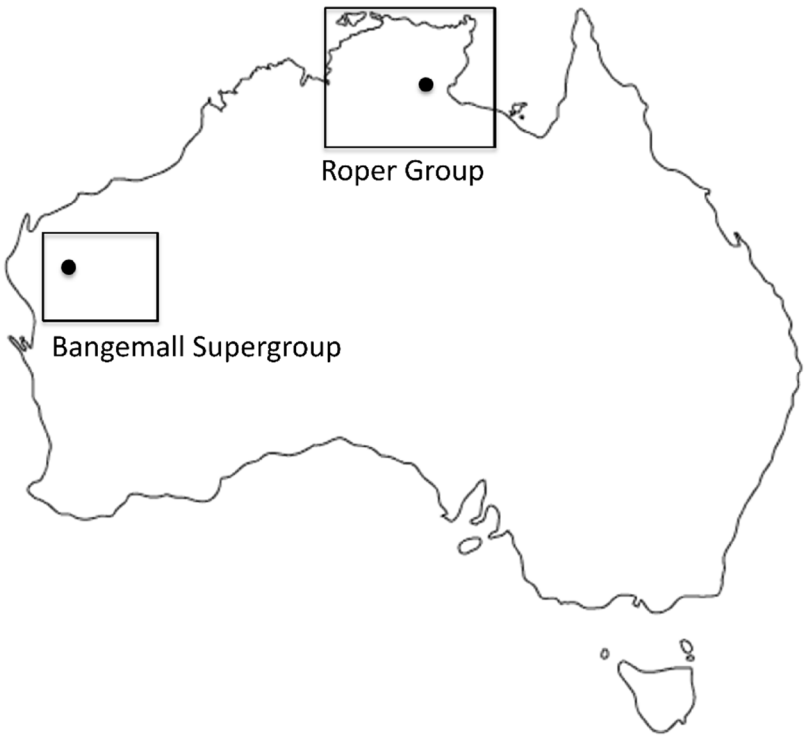

Figure 4.2**. Locations of the Bangemall Supergroup and Roper Group (boxes) and the approximate locations of sample collection (dots).**

The Bangemall rocks studied here range in age from between 1680-1610 Ma at the base of the stratigraphic section (134) to slightly older than 1070 Ma at the top (133, 136, 137), though most samples come from the >1465 Ma Edmund Group (137). Their depositional environments ranged from a peritidal carbonate platform in the Irregully Formation at the base through arenaceous siliciclastic shelf sediments containing scattered stromatolitic bioherms in the overlying Gooragoora, Blue Billy, Cheyne Springs, Kiangi Creek and Muntharra Formations, to off-shore delta-front and turbiditic deposits of the Discovery, Devil Creek, and Ullawarra Formations (132). The peritidal facies are characterized by silicified dolostones interbedded with green shale and cross-bedded sandstone, forming meter-thick transgressive cycles that pass upward from wavy laminated microbialites with intraclast breccias and teepee structures through stratiform, pseudocolumnar and muricate (linked conical) stromatolites to large bulbous stromatolites (94, 135). The shallow subtidal facies comprises unsilicified dolostone lenses among coarse-to-fine cross-bedded sandstones, siltstones and grey shales, with conical, domical and columnar stromatolites often on a gigantic scale up to 10 meters high and 5 meters broad. The deeper subtidal sediments deposited offshore commence with black kerogenous and sulfidic shale and chert but are dominated by siltstone and grey-green shale with minor fine sandstone and nodular to laminated dololutite and calcilutite, with stromatolite fragments only occurring in breccia lenses.

In terms of geobiological context, $\delta^{13}C_{carb}$ values are remarkably invariant throughout the section, averaging -0.5‰ ± 1.3‰ (135). The only significant deviation from such values occurs in the contact metamorphic aureoles around dolerite sills, where $\delta^{13}C_{carb}$ can go down to -8.4‰. However, as these rocks are bleached and kerogen-free, they were not analyzed in the current study. As noted above, stromatolites are ubiquitous in the peritidal facies, abundant and gigantic

in the shallow subtidal facies but present only as breccia fragments in the deeper offshore facies. Microfossils are often preserved in early diagenetic chert nodules within the peritidal stromatolites, recording benthic mat communities of small filamentous and coccoid prokaryotes (the *Siphonophycus-Sphaerophycus-Eosynecchococcus-Myxococcoides-Palaeopleurocapsa* assemblage of (94)). In the shallow subtidal facies, large non-matting filaments and planktonic sphaeromorph acritarchs with thin walls and moderate dimensions are preserved in grey shale (the *Siphonophycus-Leiosphaeridia-Pterospermopsimorpha-Satka* assemblage of (94)). In offshore kerogenous cherts and shales, only very large chuarid acritarchs with thick multilamellate walls (the *Crassicorium* assemblage) are preserved, their complex ultrastructure indicating that they were eukaryotic (94). Relevant to nitrogen isotopes, *Palaeopleurocapsa* in the peritidal facies is morphologically similar to an extant genus of N_2-fixing cyanobacteria.

4.4.2 *Roper Group*

Samples from the roughly coeval Roper Group from northern Australia were also analyzed in this study. These rocks crop out over 145,000 km^2 and have a maximum thickness of about 5000 meters. Their age ranges from 1492+/-4 Ma determined by U-Pb in zircon dating for the basal Mainoru Formation (138) to Re-Os dates of 1361+/-31 Ma and 1417+/-29 Ma from the upper Velkerri Formation (139) and a 1429+/-31 Ma Rb-Sr date from the McMinn Formation at the top of the section (140). The size of the basin, the abundance of glauconite and sulfide minerals, and sedimentary features indicative of strong tidal influence have been interpreted as indicating open exchange with the global ocean (141). Sediments are predominantly siliciclastic, ranging from mudrock to sandstone, that were deposited in six progradational cycles (142). High degrees of pyritization, large fractionations in sulfur isotopes and relatively small molybdenum isotope

fractionations in black shales indicate that anoxia was pervasive; euxinia was at least transient in deeper parts of the basin and was possibly common along continental margins globally at this time (95, 99, 100, 139, 141, 143, 144). In many areas, the rocks are essentially unmetamorphosed, having never been exposed to temperatures above the oil window (145).

The Roper Group is richly fossiliferous (146), with microfossil assemblages displaying onshore to offshore trends of decreasing abundance and diminishing diversity (93). There are abundant acritarchs with ultrastructure and ornamentation indicative of eukaryotic affinities (147). In support of this conclusion, kerogen and "live" oil from shales and fluid inclusions yield diverse sterane hydrocarbon biomarkers derived from eukaryotes (148–152) but see (153) for a contradictory finding, though most biomarkers are of prokaryotic origin. Sulfur isotope studies suggest that some of these prokaryotes metabolized by sulfate reduction (154) and sulfur disproportionation (143).

We obtained samples capturing a range of facies from the tide-dominated inner shelf platform, the storm-dominated outer shelf, and from the deep basin (142). The tide-dominated inner shelf platform comprises sandstones interbedded with mudstones and ooidal ironstones from a *coastal sand platform*; medium-bedded fine to coarse quartz sandstones with trough cross-stratification and ripple marks from a *tide-dominated shoreline*; and medium to thickly bedded sandstones that are massive or have swaley/hummocky cross-stratification from a *sand-dominated shelf*. The *storm-dominated shelf* consists of thinly interbedded sandstone, mudstone, and siltstone with ripple cross-laminae and small scours, or interlaminated siltstone and mudstone with minor very fine-grained sandstone. *Basinal* samples comprise interbedded mudstones and siltstones The samples came from four drill cores: Golden Grove 1 (GG1), Broughton 1(Br1), Urapunga 4 (U4), and Amoco 82/3 (A82/3). Samples from the Mainoru, Crawford, and Hodgson Formations

represent one of the six coarsening-upward progradational cycles; samples from the Corcoran and Velkerri Formations are from two separate, overlying cycles (142).

4.5 *Analytical methods*

4.5.1 *Sample preparation for bulk rock analyses*

Sample preparation followed the methods of Stüeken (24). Samples were first crushed into centimeter-sized chips using equipment that was thoroughly cleaned with methanol and 18Ω Milli-Q deionized water. These chips were then sequentially cleaned in an ultrasonic bath with hexane, methanol and deionized water for 10 minutes each to remove modern organic contaminants. The samples were then dried in a fume hood. Next, the chips were pulverized into a fine powder using an aluminum oxide ceramic puck mill that was cleaned with deionized water, methanol, and pre-combusted silica sand between samples. The powder was treated with 0.6 M HCl in three iterations (one per day) to dissolve all the carbonate, and then rinsed with deionized water in three more iterations to remove all of the acid. The samples were then left to dry in an oven (60 ^{o}C) for two days. The carbonate content was determined gravimetrically as the difference in mass between the untreated and the decarbonated powder aliquot.

4.5.2 *Kerogen extraction for organic nitrogen*

During early diagenesis, mineralization can liberate NH_4^+ from organic compounds, and pore-water NH_4^+ can then be sorbed by clay minerals through substitution for potassium, due to their similar ionic radii. There is still no consensus on whether bulk analyses (kerogen + silicate-bound nitrogen) or kerogen isolate analyses better record the primary isotopic signals in

sedimentary rocks, but due to the low metamorphic grade of these samples (section 4.7.1.4), it could be that bulk analyses better reflect primary processes, as kerogen seems to be more susceptible to metasomatic alteration (reviewed in 38). However, we further extracted the kerogen from a subset of samples where enough powder was available to quantify the relative proportions and isotopic compositions of organic-bound and silicate-bound nitrogen. The protocol was adapted from Robl & Davis (25, but also see 41). Around 5 g of rock powder were weighed into a 250 ml Nalgene bottle and decarbonated with 100 ml of 6 N HCl (reagent grade) at 60 °C in a shaking water bath overnight. Removal of $CaCO_3$ reduces the formation of insoluble calcium fluorides in subsequent steps. The acid was decanted after centrifugation (45 min at 4000 rpm) and powders were washed once with DI-H_2O (18 MΩ). Then the silicate matrix was dissolved with a mixture of DI-H_2O (100 ml) and concentrated HF (100 ml, reagent grade) at 60 °C in the shaking water bath overnight. The acid was again decanted after centrifugation. Residual fluoride precipitates were removed by treating the sample with a mixture of H_3BO_3 (62.5 g, reagent grade), DI-H_2O (100 ml) and concentrated HF (100 ml) at room temperature in the shaking water bath overnight. After decanting the acid, the sample was washed three times with 200 ml DI-H_2O, poured into a pre-combusted (500 °C overnight) scintillation vial with 10 ml of DI-H_2O, and placed into a freeze-drier for two days to remove excess water. Nalgene bottles were washed with soap, boiled in bleach for several hours, refluxed with concentrated HCl and methanol overnight, thoroughly rinsed with DI-H_2O, and dried in a clean, closed oven between samples.

4.5.3 *Isotopic analyses*

Isotopic compositions ($\delta^{15}N_{bulk}$, $\delta^{15}N_{ker}$ and $\delta^{13}C_{org}$) were determined using a Costech ECS 4010 Elemental Analyzer coupled to a Thermo Finnigan 253 continuous flow isotope-ratio mass

spectrometer. Three in-house standards (two glutamic acids "GA1" and "GA2", and dried salmon "SA") calibrated with the international reference materials USGS40 and USGS41 (26) were used to calibrate isotope measurements. Another in-house standard from the late Archean Mt. McRae formation (UW McRae) was analyzed frequently as a test for long-term precision (41). Analytical blanks resulting from the combustion process were monitored and subtracted for nitrogen isotope measurements; carbon backgrounds were insignificant. The average analytical accuracy of $\delta^{15}N$ among the individual runs based on the calibrated in-house standard "GA1" was 0.12 ± 0.09‰ (1σ). A similar test for accuracy in $\delta^{13}C_{org}$ measurements based on the calibrated in-house standard "SA" was 0.08 ± 0.10‰ (1σ). The average analytical precision of $\delta^{15}N$ and $\delta^{13}C_{org}$ among the individual runs based on the in-house standard "UW McRae" was 0.15‰ (1σ) and 0.13‰ (1σ) respectively. The average standard deviation between individual sample replicates was 0.31‰ for $\delta^{15}N$ and 0.09‰ for $\delta^{13}C_{org}$. Replication is the largest source of individual analytical uncertainty, and so it is used to represent the error of individual sample analyses. Nearly all samples were analyzed at least twice, except in cases where we were sample-limited. Samples where the $\delta^{15}N$ values varied by more than 0.5‰ or that had a nitrogen sample/blank ratio of less than five were replicated further to ensure no analytical biases.

4.6 *Results*

4.6.1 *Bangemall basin*

Bulk $\delta^{15}N$ values in the Bangemall basin have a maximum range from -1‰ to +7.5‰ with a modest trend towards lower $\delta^{15}N_{bulk}$ values offshore, higher $\delta^{15}N_{bulk}$ values near-shore, and variable $\delta^{15}N_{bulk}$ values in peritidal environments (Table 0.9). Each of the three stratigraphic sections (Fords Creek, Irregully Creek, and Wandarry Creek; Figure 4.3) shows these

characteristics (Table 4.3). Because the three sections cover equivalent facies, we normalized them with respect to the thickness of the shallow subtidal facies described by Buick *et al.* (135) and plotted a composite sequence of $\delta^{15}N_{bulk}$ values from deep to peritidal environments shown in Figure 4.3. Using all analyses from this composite transect, plus a few additional samples from other localities, the average $\delta^{15}N_{bulk}$ value is +3.3‰ ± 1.8‰ (n=18) for the peritidal facies, +3.4‰ ± 1.4‰ (n=26) for the shallow subtidal facies, and +1.8‰ ± 1.6‰ (n=28) in the deep water facies. Both the peritidal and shallow subtidal environments are statistically heavier than the basinal environment ($p_{one\text{-}tailed}$ = 0.003 and 0.00008 respectively), though peritidal and shallow subtidal $\delta^{15}N_{bulk}$ values are not statistically different from one another ($p_{one\text{-}tailed}$ = 0.67). The isotopic composition of kerogen isolates match well with the measured $\delta^{15}N_{bulk}$ values (average difference of 0.8‰ among replicated samples; Table 0.8), which indicates that the observed gradient is not an artifact of mixing between isotopically distinct nitrogen reservoirs ($N_{kerogen}$ and $N_{silicate}$). The average total organic carbon [%] and total nitrogen [%] for the Bangemall Group samples are 0.25%, and 0.01% respectively (See Table 0.9).

The same set of samples has $\delta^{13}C_{org}$ values that mostly range from -25‰ to -35‰. We found a slight basinal gradient of about 3‰ with lighter $\delta^{13}C_{org}$ in samples deposited in deeper subtidal environments (Table 4.4). Samples from each depositional environment come from statistically different $\delta^{13}C_{org}$ populations (p_{anova} = 0.002).

4.6.2 *Roper basin*

The Roper basin has $\delta^{15}N_{bulk}$ values ranging from -1‰ to +4.9‰ with a facies-dependent trend from lighter values in basinal and storm-dominated shelf samples to heavier values in tide-dominated platform samples (average gradient in Table 4.3, all data in Table 0.10). The mean

$\delta^{15}N_{bulk}$ value in the tide-dominated platform environment is statistically different from that of the storm-dominated shelf and basinal environments ($p_{one\text{-}tailed}$ = 0.008 and 0.0005 respectively). The outer shelf and basinal $\delta^{15}N_{bulk}$ populations are statistically indistinguishable from one another ($p_{one\text{-}tailed}$ = 0.27). The average total organic carbon [%] and total nitrogen [%] for the Roper Group samples is 0.34%, and 0.02% respectively (See Table 0.10).

Unlike the Bangemall Group, the Roper Group shows no sign of a trend in $\delta^{13}C_{org}$ across the basin (total average -31.3‰ ± 1.55‰, n=34, Table 3). Again, kerogen isolates are very similar to bulk samples with an average deviation from the $\delta^{15}N_{bulk}$ values of 0.6‰ for replicated samples (Table 0.8).

4.7 *Discussion*

4.7.1 *Diagenesis and metamorphism*

4.7.1.1 Oxic diagenesis: effects on preserved $\delta^{15}N_{bulk}$

Diagenesis under oxic conditions may increase $\delta^{15}N_{bulk}$ by as much as +4‰ (32, 155) due to kinetic fractionation of nitrogen isotopes in favor of ^{14}N during the deamination of organic matter (156), followed by oxidation and loss of the resulting light inorganic nitrogen (155, 157). We have no quantitative evidence to completely rule out any effect of oxic diagenesis; however it could not by itself explain the full ranges of $\delta^{15}N_{bulk}$ values we observe in the Bangemall (8‰) and Roper (6‰) groups, which are greater than the maximum range known to be caused by aerobic diagenesis. Furthermore, in the absence of bioturbation, middle Proterozoic sediments should have been largely anoxic even under an oxic water column. Hence the effects would likely have been

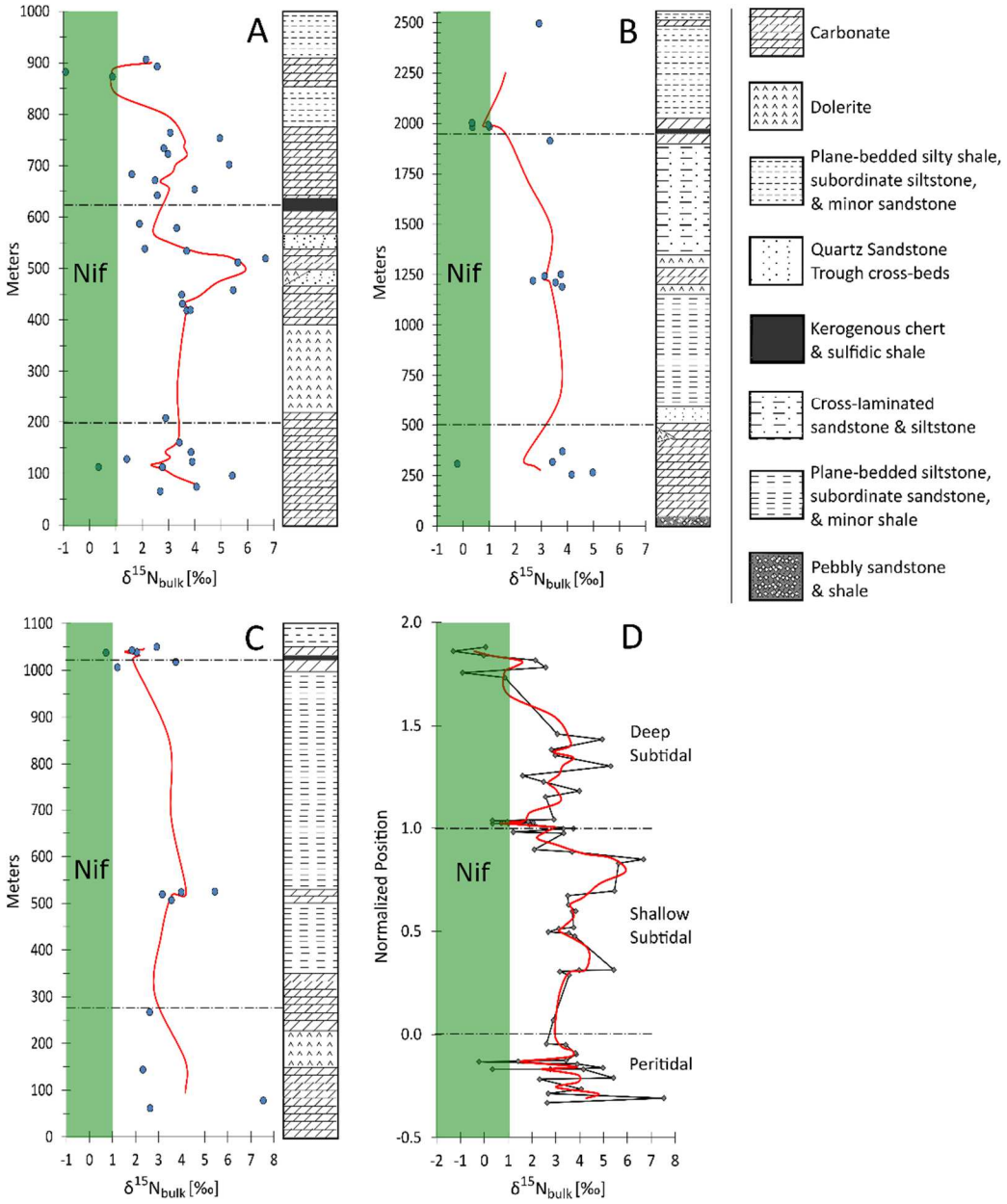

Figure 4.3. **Stratigraphic $\delta^{15}N_{bulk}$ plots of Bangemall transects**. (A) Fords Creek, (B) Irregully, (C) Wandarry. Depositional facies in each panel are as in panel (D), with deep subtidal above the top dot-dash line, shallow subtidal in the middle, and peritidal below the bottom dot-dash line. Panel (D) is a normalized compilation of all the Bangemall transects where the positions of each point are relative to the thickness of the shallow subtidal facies. The red line indicates the running mean over three points.

Table 4.3. **$\delta^{15}N_{bulk}$ values for the Bangemall basin transects and whole basin, the Roper basin, and the Belt basin. Belt data are from Stüeken (24)**. Parenthetical facies labels are specific to the Roper basin. Uncertainties are expressed as ±1σ. n = number of samples.

	Peritidal (tide-dominated platform) $\delta^{15}N_{bulk}$	**Shallow subtidal (storm-dominated shelf) $\delta^{15}N_{bulk}$**	**Deep subtidal (basinal) $\delta^{15}N_{bulk}$**
Bangemall basin:			
Fords Creek	3.1‰ ± 1.5‰ (n=10)	3.9‰ ± 1.4‰ (n=12)	2.7‰ ± 1.6‰ (n=13)
Irregully Creek	3.2‰ ± 2.0‰ (n=5)	3.4‰ ± 0.4‰ (n=6)	1.1‰ ± 1.1‰ (n=5)
Wandarry Creek	3.8‰ ± 2.5‰ (n=4)	3.5‰ ± 1.4‰ (n=6)	1.9‰ ± 0.9‰ (n=4)
All	3.3‰ ± 1.8‰ (n=18)	3.4‰ ± 1.4‰ (n=26)	1.8‰ ± 1.6‰ (n=28)
Roper basin:	3.7‰ ±0.8‰ (n=6)	2.3‰ ± 1.3‰ (n=20)	2.0‰ ± 0.8‰ (n=8)
Belt basin:	3.7‰ ± 1.4‰ (n=13)	1.5‰ ± 1.2‰ (n=35)	0.1‰ ± 0.9‰ (n=21)

Table 4.4. **$\delta^{13}C_{org}$ in the Bangemall, Roper, and Belt basins. Parenthetical facies labels are specific to the Roper basin**. Data from the Jixian basin are taken from Guo *et al.* (158). Uncertainties are expressed as ±1σ. n = number of samples.

	Peritidal (tide-dominated platform) $\delta^{13}C_{org}$	**Shallow subtidal (storm-dominated shelf) $\delta^{13}C_{org}$**	**Deep subtidal (basinal) $\delta^{13}C_{org}$**
Bangemall basin	-27.0‰ ± 3.2‰ (n=18)	-29.2‰ ± 2.6‰ (n=26)	-30.2‰ ± 2.9‰ (n=28)
Roper basin	-31.5‰ ± 0.9‰ n=6	-30.6‰ ± 1.2‰ n=20	-32.9‰ ± 1.6‰ n=8
Belt basin	-32.2‰ ± 1.2‰ (n=13)	-30.1‰ ± 1.9‰ (n=35)	-22.9‰ ± 2.9‰ (n=21)
Jixian basin	-28.2‰ ± 1.6‰ (n=191)	-30.8‰ ± 2.0‰ (n=61)	n/a

much smaller than in modern sediment profiles (155). In thin sections from the Bangemall Group, shallow sediments show no evidence of being more oxidized than deeper equivalents. In particular iron oxides, which have a lower redox potential than nitrate and should thus have formed if pore fluids that were oxidizing enough for nitrification, are absent in both facies. Therefore, a systematic bias of shallow oxic and deep anoxic diagenetic isotope effects is unlikely to be the reason for the basinal gradients in $\delta^{15}N_{bulk}$.

4.7.1.2 Anoxic diagenesis: effects on preserved $\delta^{15}N_{bulk}$

Anoxic diagenesis can decrease the $\delta^{15}N_{bulk}$ of bulk nitrogen in sediments through either the addition of ^{15}N-depleted biomass from in-situ growth of anaerobic bacteria (32), or if organic compounds with relatively higher $\delta^{15}N$ values such as proteins (159) are preferentially degraded, releasing isotopically heavy NH_4^+ into pore waters. However, neither of these mechanisms should have introduced a basinal gradient, because as noted above all sediment samples in this study likely underwent anoxic diagenesis regardless of the redox state of the overlying water column. Indeed if anoxic diagenesis caused addition of light N_{org} from bacterial growth, derived from N_2 fixation or the preservation of its isotopic signal, (32), then preferential growth of those organisms in deeper environments would only support our interpretation of offshore nitrate depletion (discussed below). We can further address the latter mechanism, *i.e.* preferential ^{15}N loss from degrading biomass, by comparing bulk $\delta^{15}N$ values to the $\delta^{15}N$ values of kerogen isolates. This diagenetic pathway should have led to an isotopic enrichment in silicate minerals that absorbed some of the dissolved heavy NH_4^+. Hence the $\delta^{15}N$ of the kerogen isolate from a sample should be systematically lighter than its bulk value, which is not observed. In fact, the Roper and Bangemall kerogen analyses show a very slight average isotopic enrichment of +0.6‰ and +0.8‰,

respectively, over the bulk analyses (Table 0.8). These data may be best explained if NH_4^+ release did not lead to a net isotopic fractionation, perhaps because the effects of kinetic fractionation during deamination (156) and relative compound instabilities (cf. 159) were roughly balanced. Bulk sediment values are therefore probably close to the original isotopic composition of biomass.

4.7.1.3 Diagenetic effects on the $\delta^{13}C$ of organic matter

Both aerobic and anaerobic diagenesis mildly decrease the $\delta^{13}C$ of organic matter to a maximum of ~1.6‰ (32, 155), probably due to preferential degradation of isotopically heavy organic compounds. Carbohydrates and proteins, which are more susceptible to microbial degradation under both oxic and anoxic conditions, tend to be more enriched in $\delta^{13}C$ than other more recalcitrant fractions such as lipids (32). Diagenetic effects can be larger (on the order of ~20‰ depending on the substrate) if organic degradation is catalyzed by microbes using the Wood-Ljungdahl pathway, which includes methanogens, methanotrophs, and acetogens (160). The range of $\delta^{13}C_{org}$ in the Bangemall samples is too large (~10‰) to be explained solely by diagenetic effects that do not involve the Wood-Ljungdahl pathway. The slight gradient from lighter values offshore to heavier values near-shore is similar to the environmental trends seen in other studies spanning the Archean and Proterozoic (49, 158, 161), suggesting that it is a primary feature reflecting differential contributions from varying microbial metabolisms in response to local redox conditions (4.7.3).

4.7.1.4 Metamorphism

Four lines of evidence indicate that the effects of metamorphism on primary nitrogen isotope signals were probably insignificant. First, as stated previously, both the Bangemall and Roper rocks were not exposed to temperatures much above the oil window (94, 145), whereas there seems to be no metamorphic effects on nitrogen isotopes (*i.e.* preferential loss of ^{14}N) in other rocks up through the gas window (162); these may only become important (> 1 ‰) at greenschist facies and above (reviewed by 30). Second, the slight metamorphic gradient from east to west in the Bangemall basin does not parallel, but is nearly perpendicular to, the three transects, but no significant differences are evident between them. Third, if metamorphism did have an effect on the nitrogen isotope ratios of the samples, then increasing $\delta^{15}N_{kerogen}$ should correlate with increasing $(C/N)_{kerogen}$ ratios, as nitrogen is more mobile than carbon and ^{14}N is more mobile than ^{15}N under such conditions (70, 71, 163). However, such correlations are not seen in either sample set (Figure 4.4, $r^2 = 0.28$ for Bangemall, and $r^2 = 0.14$ for Roper). Lastly, offsets between $\delta^{15}N_{silicate}$ and $\delta^{15}N_{kerogen}$ of up to ~12‰ have been observed in rocks within hornfels aureoles (4), suggesting there may be a relationship between increasing metamorphic grade and increasingly divergent $\delta^{15}N_{bulk}$ and $\delta^{15}N_{kerogen}$ values. There is little consensus on whether kerogen or bulk nitrogen better preserves primary biological signals (see 38); however, on average, the kerogen nitrogen isotope values in the Bangemall and Roper Groups fall within 0.7‰ of bulk values, inconsistent with significant metamorphic alteration.

In the case of carbon isotopes, metamorphism also can spur exchange between the carbon in organic matter and the carbon in carbonates, causing $\delta^{13}C_{carb}$ to become depleted by up to 5‰

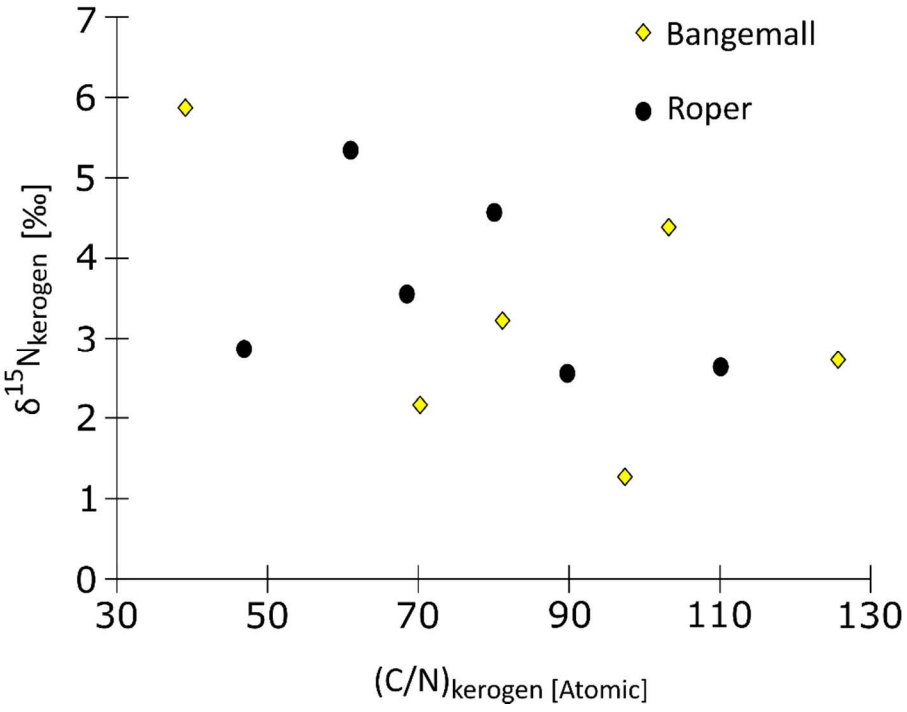

Figure 4.4. **$\delta^{15}N_{kerogen}$ vs. $TOC/N_{kerogen}$ (total organic carbon / kerogen-bound nitrogen) for Bangemall (yellow diamonds) and Roper (black circle) samples.**

and $\delta^{13}C_{org}$ to become enriched by as much as 15‰ (reviewed by 164). This effect is sensitive to the relative percentages of carbonate to organic carbon. Hence in carbonate-rich sediments such as the Bangemall samples, depletion of the carbonate may not be noticeable but enrichment of organic matter might be prominent. However, fractionations caused by carbon equilibration between organics and carbonates are generally insignificant below greenschist facies (165–167). There is no inverse correlation between the $\delta^{13}C_{org}$ and $\delta^{13}C_{carb}$ values of the same Bangemall samples ($r^2 = 0.003$), and the total fractionation $\Delta^{13}C$ (= $\delta^{13}C_{carb} - \delta^{13}C_{org}$) is not inversely correlated with carbonate content ($r^2 = 0.008$), even in the largest negative excursions of $\delta^{13}C_{carb}$. These lines of evidence all suggest the carbon isotopic composition of the samples measured in this study are unaltered by metamorphism.

4.7.2 *Carbon cycling in the Bangemall and Roper Basins*

The Bangemall basin shows a slight spatial trend in $\delta^{13}C_{org}$ values, with relatively more depleted values offshore and more enriched values near-shore (Table 4.4). The $\delta^{13}C_{org}$ gradient in the Bangemall basin is thus the opposite to that of the Belt basin (24), where onshore sediments are markedly depleted in $\delta^{13}C$ compared to offshore sediments (Table 4.4, $p_{anova} = 0.0009$). However, a similarly oriented gradient to this study was recently reported from the roughly contemporaneous Jixian Group (1.5 Ga) with values around -28.2‰ onshore and -30.8‰ offshore with $p_{anova} < 0.0001$ (Table 4.4, (158)). Given that $\delta^{13}C_{carb}$ is nearly invariable in this and earlier Mesoproterozoic basins (135), this gradient is probably not caused by changes in the isotopic composition of dissolved inorganic carbon, as seen from the later Mesoproterozoic onwards (168, 169), but may instead reflect spatial variability in biological fractionation effects. A similar trend was also observed in the Pretoria and Fortescue Groups, which along with the Jixian Group and

Bangemall Group represent the Mesoproterozoic, Paleoproterozoic, and Neoarchean. (49, 158, 161). All $\delta^{13}C_{org}$ values in the Bangemall and Roper basins are consistent with autotrophic fixation of CO_2 by the Calvin cycle that is used by a wide range of organisms including cyanobacteria and eukaryotic algae (170). However, the fact that multiple basins through time show a similar trend suggests there may be (i) autotrophic carbon fixation under a gradient of nutrient availability, or (ii) photoautotrophic biomass mixed with varying proportions of secondary chemoautotrophic and/or heterotrophic biomass, as proposed for the contemporaneous Belt and Jixian basins (24, 158). Such secondary metabolisms could include methanogenesis, acetogenesis, and methanotrophy that use the Wood-Ljungdahl pathway and are known to cause large fractionations in carbon isotopes (160) We cannot rule out either possibility, and it is also not clear why the reverse gradient is seen in the Mesoproterozoic Belt basin (24). The samples from the Roper Group do not show a gradient in $\delta^{13}C_{org}$ values.

4.7.3 *Nitrogen cycling in the Bangemall and Roper Basins*

The Bangemall transects and the Roper Group samples all show a ~1.0‰ to ~2.0‰ gradient in nitrogen isotopes, with lighter values recorded in offshore facies and heavier values in near-shore facies. We note that our results for the deep subtidal/basinal facies of the Bangemall and Roper groups (+1.8‰ ± 1.6‰, n = 28; +2.0‰ ± 0.8‰, n = 8 respectively) are in good agreement with basinal mudstones from the roughly contemporaneous Xiamaling Formation ($\delta^{15}N_{bulk}$ = +2.1±0.2‰, n = 4, age 1.37 Ga) (171). The facies-dependent trend in the Bangemall and Roper basins likely reflects primary nitrogen cycling rather than post-depositional alteration (see above), and so is interpreted as being consistent with cross-basin differences in nitrogen speciation, comparable to the Belt basin (Table 4.3; (24)). As noted in section 4.2, Fe-S

systematics, $\delta^{34}S$, and trace metal data also have facies-dependent trends in the Roper Group, providing evidence for an oxic near-shore water column, and anoxic/euxinic basinal deep waters overlain by at least transiently oxic surface waters (99, 144). There are no equivalent data for the Bangemall Group, but a similar range of conditions appears to have been widespread in the Mesoproterozoic ocean (100). These data are consistent with, and indeed support, our interpretation of the nitrogen isotope data which follows.

The lightest $\delta^{15}N_{bulk}$ values are most plausibly explained by an ecosystem dominated by N_2 fixation using the molybdenum-bearing nitrogenase Nif (37, 172, 173). If the ocean had been fully oxygenated at that time, more so than today, then values around 0‰ could in theory also have been produced by quantitative nitrification of biomass followed by quantitative re-assimilation of nitrate without any denitrification and consequent isotopic fractionation in oxygen-minimum zones (174). However, this scenario is unlikely in the mid-Proterozoic, where widespread anoxia has been well documented (95, 98, 100, 175, 176). An N_2-fixation dominated regime is thus the most parsimonious explanation for light $\delta^{15}N_{bulk}$ values in our samples.

Three alternative mechanisms can be considered to explain the isotopically heavy $\delta^{15}N$ values (> 2‰) (see (24, 28, 38) for detailed discussion).

(i) It has been hypothesized that in an anaerobic nitrogen cycle, partial assimilation of an NH_4^+ pool by organisms can leave the residual NH_4^+ pool enriched in ^{15}N, as life preferentially assimilates ^{14}N into biomass (74). If this enriched pool of NH_4^+ is subsequently transported to a different location and assimilated by organisms, two isotopic facies result: the first location preserves light $\delta^{15}N_{bulk}$ and the second preserves heavy $\delta^{15}N_{bulk}$.

(ii) Partial nitrification of NH_4^+ can create a nitrate pool that is depleted in ^{15}N and a residual NH_4^+ pool that is enriched in ^{15}N because nitrification preferentially selects for the lighter

isotope. Assimilation of the NH_4^+ pool will result in heavy $\delta^{15}N_{bulk}$ so long as the light nitrate is removed from the system, either through subsequent complete denitrification or relocation. Partial nitrification is rare in modern water columns, occurring where seasonally fluctuating oxygen concentrations occur in transiently stratified waters (177, 178). However, it is possible that low oxygen concentrations in the Mesoproterozoic enabled more widespread partial nitrification coupled with the removal of the light nitrate pool by complete denitrification. Subsequent uptake of the leftover heavy $NH_4^+$and further remineralization of organic matter to NH_4^+ could result in a range of positive $\delta^{15}N_{bulk}$ values (24, 177).

(iii) Partial denitrification of a nitrate pool in the water column will leave the residual nitrate enriched in ^{15}N, as the biologically governed steps of denitrification, like nitrification, preferentially use ^{14}N over ^{15}N. So $N_{2(g)}$, the most common end-product of denitrification, would be isotopically depleted in ^{15}N and organisms could assimilate the remaining heavy nitrate pool. This is the mechanism producing heavy $\delta^{15}N_{bulk}$ in the modern ocean (e.g. 76, 179).

Mechanisms (i) and (ii) should result in two distinct isotopic reservoirs, one that is relatively depleted below -2‰, and one that is relatively enriched above +1‰. There are no samples or sample sets from this study that are lighter than the $\delta^{15}N_{bulk}$ values that would result from N_2 fixation by Mo-nitrogenase (-2‰ to +1‰, (37)). We cannot rule out that a much lighter facies exists somewhere within or adjacent to the Bangemall and Roper basins, but was not sampled. Nevertheless, explanations (i) and (ii) are unlikely for several reasons. First, the Black Sea, our best modern analog for the Mesoproterozoic ocean, has a large NH_4^+ reservoir in the anoxic bottom water, but underlying sediments do not record evidence of partial NH_4^+

assimilation; values are close to 0‰, reflecting nitrogen limitation and N_2 fixation in the photic zone (122). The same is true for the modern anoxic Cariaco basin (180). This argues against an isotopically light nitrogen reservoir resulting from partial NH_4^+ assimilation in the similarly chemically stratified Mesoproterozoic ocean (option i). Hydrodynamically, the Black Sea and Cariaco basin are probably more stagnant than open marine settings like the Roper and Bangemall basins, and so it is conceivable that these Mesoproterozoic settings experienced a relatively higher upwelling flux of NH_4^+ from deeper waters into the photic zone. In theory, this scenario could favor non-quantitative NH_4^+ assimilation. However, in the modern ocean, NO_3^- assimilation usually goes to completion with minimal net isotopic fractionations because nitrogen is the proximally limiting nutrient (e.g. 34, 179, 181). There is no *a priori* reason to expect that this would have been different if the nitrogen compound was NH_4^+ instead of NO_3^-. This is especially true if low Mo levels reduced N_2 fixation rates in the Mesoproterozoic ocean and exacerbated nitrogen limitation (98). Furthermore, upwelling would have been most pronounced along the continental margin rather than far offshore, and so the hypothetical isotopically light reservoir should be preserved in our sample set, which is not the case. Regarding option (ii), in the Black Sea nitrification quickly goes to completion under suboxic conditions at the chemocline (102). The same is true in bacterial cultures and oxygen minimum zones along open marine margins (182–184), suggesting that partial nitrification may also have been rare in the past as long as surface waters were at least mildly oxidizing. Indeed, in modern environments partial nitrification requires transient seasonal changes in the environment such as fluctuating sea ice cover and is not known to operate over long geologic timescales. This leaves option (iii), partial denitrification at the chemocline (cf. 124) or in sediment pore waters (123) as the most plausible mechanism responsible for heavier $\delta^{15}N_{bulk}$ values in the shallower facies of the Bangemall and Roper basins. We thus

interpret the large variations of $\delta^{15}N_{bulk}$ in the Bangemall and Roper basins as reflecting differential mixing between components derived from N_2 fixation (alone responsible for the most depleted values between -2‰ to +1‰) and from an aerobic nitrogen cycle coupled with varying degrees of partial denitrification of a nitrate pool followed by nitrate assimilation yielding $\delta^{15}N_{bulk}$ values above +1‰.

As some peritidal samples have anomalously light $\delta^{15}N_{bulk}$ values, it may be that N_2 fixation temporarily dominated in microbial mats that were transiently cut off from the marine nitrate pool at low tide, which would be consistent with microfossil evidence from the Bangemall basin peritidal facies, where *Palaeopleurocapsa* (morphologically similar to a modern genus of nitrogen-fixing cyanobacteria; Section 4.4.1) is found (94). All shallow subtidal samples have $\delta^{15}N_{bulk}$ values above +1‰ (barring one outlier), suggesting that some nitrate was always available in the water column and that there was a permanent chemocline where partial denitrification was occurring. Deep subtidal samples have lower $\delta^{15}N_{bulk}$ values than shallow (Table 4.3) and contain samples within the -2‰ to +1‰ range (Figure 4.5, Figure 4.6). Almost all deep-water values for both basins are lighter than +3 ‰, *i.e.* lighter than most modern and recent marine sediments (> +4 ‰, *e.g.* (185–187)). This suggests that offshore sites had less nitrate available compared to shallower facies and the modern deep ocean. Thus our data is consistent with at least some nitrate in all depositional environments in both the Bangemall and Roper basins, but relatively more in near-shore facies than offshore. When we discuss nitrate availability, we refer to availability in the zones of highest biological production, as this zone will result in the dominating isotopic signal preserved in sediments. This is probably the photic zone, and it is unlikely that nitrate could have existed much deeper in the water column if bottom waters during the Mesoproterozoic were predominantly anoxic.

4.7.4 *$\delta^{15}N_{bulk}$ variability in the Bangemall and Roper basins*

The variability of $\delta^{15}N_{bulk}$ values in the Bangemall and Roper shallow water facies can be better understood by drawing an analogy to the variability of $\delta^{34}S$ values proposed for the Proterozoic (188). In this conceptual model, the rate of change in the nitrate isotopic composition in the shallow water environments is controlled by the size of the nitrate reservoir, and the size and isotopic composition of fluxes that both add and remove isotopically distinct nitrogen. The relationship is as follows, with fluxes labeled in Figure 4.7:

$$d(\delta_{NO3-})/dt = (F_{upwell}*\Delta_{upwell} + F_{nitri.}*\Delta_{nitri.} + F_{fixation}*\Delta_{fixation} - F_{assim}*\Delta_{assim} - F_{den.sed.}*\Delta_{den.sed.} - F_{den.wc.}*\Delta_{den.wc.}) / M_{NO3-}$$

$d(\delta_{NO3-})/dt$ is the isotopic rate of change of the shallow water nitrate reservoir. F_{upwell} is the flux of nitrogen being upwelled from deep water environments. Δ_{upwell} is equivalent to $\delta^{15}N_{NH4+} - \delta^{15}N_{NO3-}$, which is the isotopic difference of the ammonium being upwelled and the existing shallow water nitrate reservoir. $F_{nitri.}*\Delta_{nitri.}$ is the isotopic flux term of organic nitrogen that is nitrified within the shallow water environment. $\Delta_{nitri.}$ is 0 because nitrification likely goes to completion, and will preserve the isotopic composition of shallow water nitrate, from which the organic matter was likely derived. $F_{fixation}*\Delta_{fixation}$ is the isotopic flux contributed by N_2 fixation in shallow water environments. This flux could contribute to changes in the isotopic composition of shallow water nitrate as $\Delta_{fixation}$ equals $\delta^{15}N_{fixation} - \delta^{15}N_{NO3-}$.

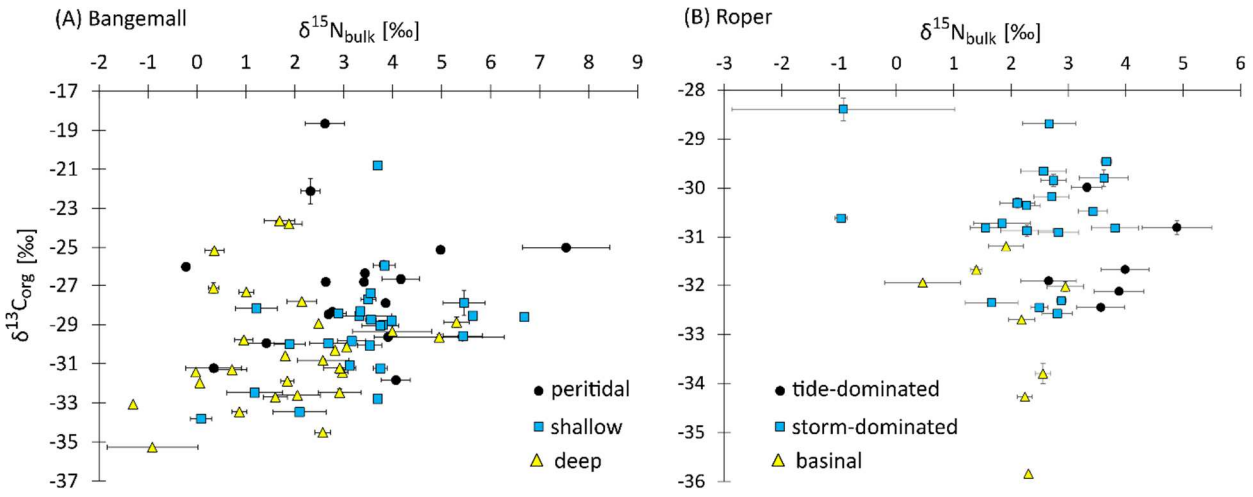

Figure 4.5. **$\delta^{15}N_{bulk}$ plotted against $\delta^{13}C_{org}$ for the Bangemall (A) and Roper (B) basins**. The plot also includes those samples from the Bangemall basin that do not belong to one of the three main transects shown in Figure 4.3A-C. Error bars are ±1σ.

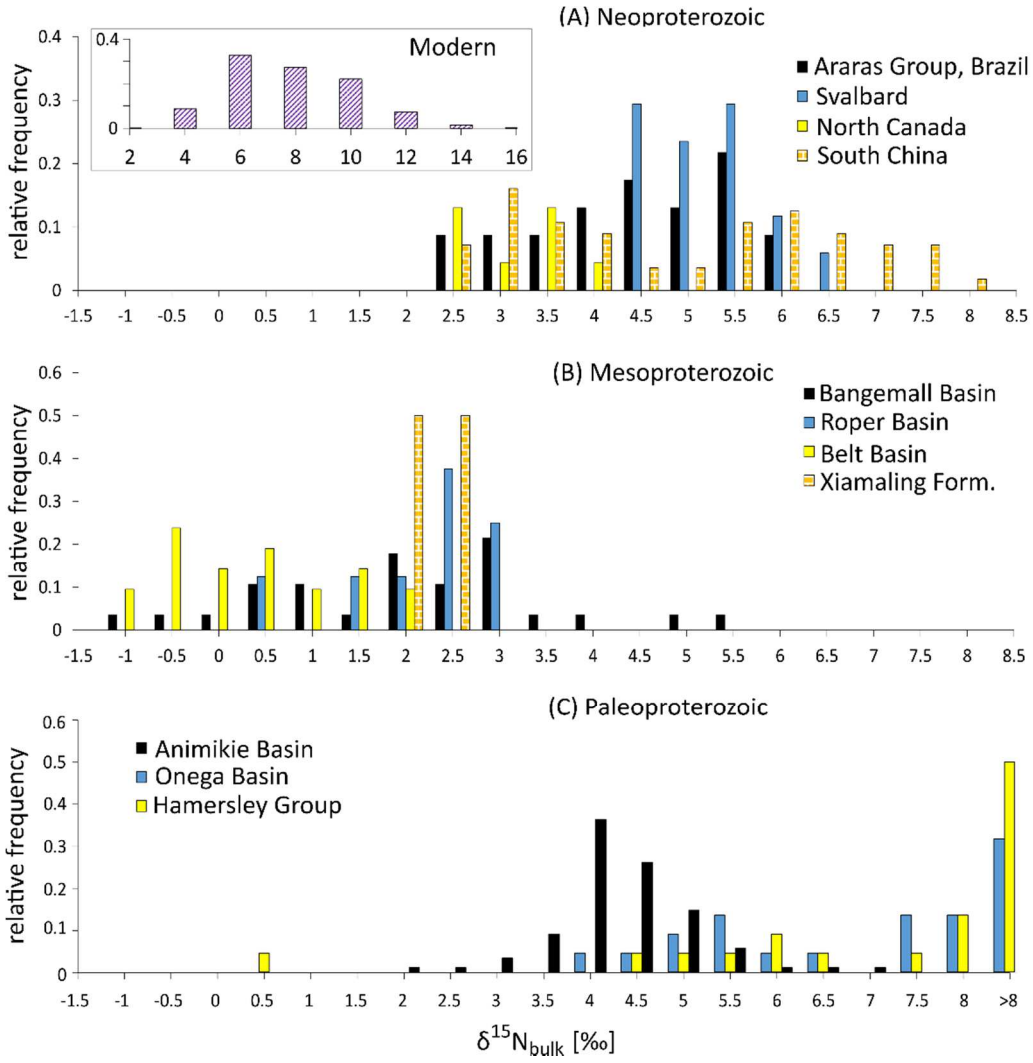

Figure 4.6**. Histogram of Proterozoic offshore $\delta^{15}N_{bulk}$ data.** (A) Neoproterozoic era (1.0-0.548 Ga) with data from Ader *et al.* (125) and Kikumoto *et al.* (189); (B) Mesoproterozoic era (1.6-1.0 Ga) with data from Stüeken (24), Luo *et al.* (171) and this study; (C) Paleoproterozoic era (2.5-1.6 Ga) with data from Busigny *et al.* (113), Kump *et al.* (115) and Godfrey *et al.* (72). Subsets of the datasets listed above were taken to only include offshore environments: from Ader *et al.* (125) the Camil, Carmelo, and Copacel sections from Brazil and all data from Svalbard and North Canada. From Kikumoto *et al.* (189) all data from the Doushantuo Formation. From Stüeken (24) data from the Newland Formation in Deep Creek. From the Bangemall and Roper of this study, "deep" and "basinal" data respectively. From Luo *et al.* (171) all data. From Busigny *et al.* (113) data from the Brockman Iron Formation. From Kump *et al.* (115) data from above 180 meters in core depth (from 0m to 180m). From Godfrey *et al.* (72) data from cores MGS-7 and MGS-8. The inset in panel A shows modern marine sediment data from Tesdal *et al.* (179). The modern data show no correlation with water depth and are therefore not separated by facies. Paleoproterozoic data from the Aravalli Group (74, 190) were excluded because they are of higher metamorphic grade and their depositional environment is uncertain.

It may be the case, however, that $F_{fixation}$ is 0 because N_2 fixation was probably negligible onshore where nitrogen was more available. $F_{assim}*\Delta_{assim}$ is the isotopic flux of nitrogen being assimilated by shallow water organisms. This is likely also 0, as there is no evidence for non-quantitative assimilation (negative $\delta^{15}N_{bulk}$ values). $F_{den.sed.}*\Delta_{den.sed}$ is the isotopic flux associated with sedimentary denitrification. $\Delta_{den.sed}$ is also close to 0, as sedimentary denitrification does not impart large isotopic fractionations on the nitrate in the overlying water column (123, 191). $F_{den.wc.}*\Delta_{den.wc}$ is the isotopic flux from canonical water column denitrification. $\Delta_{den.wc}$ is around 20. M_{NO3-} is the total onshore nitrate reservoir in grams or moles. Removing the 0 terms, we are left with:

$$d(\delta_{NO3-})/dt = (F_{upwell}*\Delta_{upwell} - F_{den.wc.}*\Delta_{den.wc.}) / M_{NO3-}$$

The average isotopic rate of change is 14.7‰, 4.7‰, and 0.3‰ per 100 meters within the shallow water facies of the Bangemall, Roper, and Belt basins respectively. The sedimentation rates between the basins were likely different, but if we assume that they were somewhat comparable then these isotopic rates of change may reflect primary changes in shallow water nitrate. For the Belt basin $d(\delta_{NO3-})/dt$ is an order of magnitude less than in the Bangemall and Roper basins. In the context of our model, this would have to result from the Belt basin either having a greater nitrate reservoir in shallow waters (M_{NO3-}), or smaller fluxes ($F_{upwell}*\Delta_{upwell}$ and $F_{den.wc.}*\Delta_{den.wc}$). It is unlikely that the Belt basin had a greater nitrate reservoir compared to the Bangemall and Roper basins because it was likely more restricted from the open ocean (see following section). As a result of this restriction, upwelling and water column denitrification fluxes were likely smaller in magnitude in the Belt basin than those in the Bangemall and Roper basins.

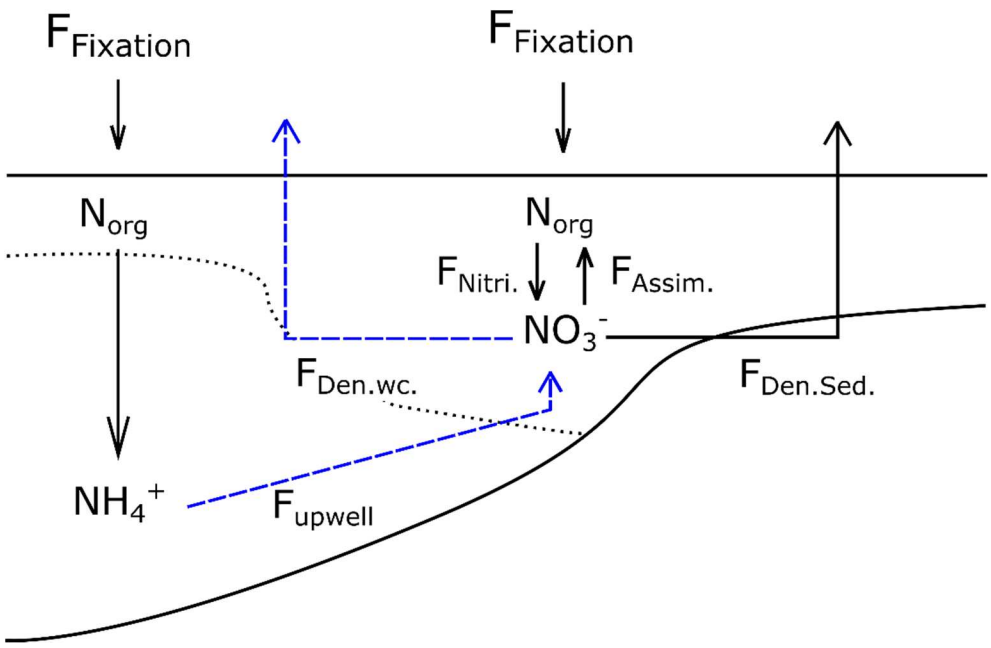

Figure 4.7**. Schematic of the proposed Mesoproterozoic nitrogen cycle.** Shown are fluxes (F) both in and out of a shallow water nitrate reservoir as we propose for the Bangemall and Roper basins. Blue flux arrows represent fluxes that, when varied, are most likely able to change the isotopic composition of a relatively small nitrate reservoir. All other fluxes are unlikely to change the isotopic composition of the nitrate reservoir. Flux labels are as follows: $F_{fixation}$ = N_2 fixation flux, $F_{nitri.}$ = nitrification of organic matter to nitrate, $F_{assim.}$ = assimilation of nitrate into biomass, $F_{den.wc.}$ = water-column denitrification, $F_{den.sed.}$ = sedimentary denitrification, F_{upwell} = upwelling of ammonium from anoxic waters.

In this conceptual model, then, the Bangemall and Roper basins, having a greater connection to the open ocean, had larger upwelling and denitrification fluxes that, when altered, resulted in changes in the isotopic composition of the shallow nitrate reservoir. This variability is reflected in the variability of $\delta^{15}N_{bulk}$ values from the shallow water depositional environments in each basin. Variability in the deep basin can be attributed to a small nitrogen reservoir, where incursions of nitrate into the deep ocean could not fully be isotopically buffered by existing NH_4^+. If the fixed nitrogen reservoir had been larger in the Mesoproterozoic ocean, then it would have been less susceptible to isotopic change. The degree of variability in our sample sets may thus be a reflection of a small and isotopically variable nitrogen supply in comparison to the Paleo- and Neoproterozoic settings that are more uniform (Section 4.7.6).

4.7.5 *Comparing the Bangemall and Roper basins to the Belt basin*

The Bangemall and Roper basins show facies-dependent trends in nitrogen isotopes similar in direction to but smaller in magnitude than the Mesoproterozoic Belt Supergroup (Table 4.3; (24)), suggesting that such a pattern may have been common in the Mesoproterozoic Era. The Belt basin, however, has a deep depositional environment where 80% (n=21) of the samples fall within the range of Nif N_2 fixation, compared to 36% and 8% in the Bangemall and Roper respectively. This difference could be an artifact of sampling, if relatively deeper facies were sampled in the Belt and not captured in the Bangemall transects and Roper samples. However, the Belt basin could instead have been more restricted and consequently more strongly stratified than the Bangemall and Roper basins, which may have led more rapid depletion of the dissolved nitrate reservoir. This hypothesis is supported by the geometry of the Belt basin, which is thought to have been formed by intracontinental rifting (192) and may only have had limited exchange with the

open ocean for some of its history (e.g. 193–195). The unusually steep gradient in organic carbon isotopes from -32.2‰ to -22.9‰, which is not seen in any other Mesoproterozoic basins ((158), this study), further supports significant water mass stratification in the Belt basin. Hence the subtler carbon and nitrogen isotopic gradients in the Roper and Bangemall basins may be more representative of global marine conditions. Importantly, none of the three basins show nitrogen isotope values within the range of vanadium or iron-based nitrogenases (< -6‰, (37)), suggesting that Mo was available in sufficient quantities for the dominance of the molybdenum nitrogenase despite being present at low concentrations in the Mesoproterozoic ocean (98).

4.7.6 *Mesoproterozoic nitrate minimum*

While available data are consistent with a basinal gradient in $\delta^{15}N_{bulk}$ and thus in nitrogen speciation in the Mesoproterozoic (Section 4.7.3), this was not the case in the earlier and later Precambrian. In the mid-Archean Witwatersrand Supergroup (2.87-2.96 Ga), sediments deposited near estuaries (+1.2 ± 1.0 ‰) are on average slightly heavier than marine sediments further offshore (-1.6 ± 0.8 ‰) (41), but almost all of these values fall within the range of biological N_2 fixation. The subtle gradient is thus more likely a result of varying Fe^{2+} availability to diazotrophic microbes (173) rather than a gradient in nitrate abundance. Nitrate was likely scarce in all parts of the mid-Archean ocean, including shallow waters (41), consistent with very low levels of atmospheric oxygen at this time (46, 52, 196). Surface water nitrate levels may have increased in the late Archean with the onset of low levels of oxidative weathering and enhanced oxygenation of the surface ocean (10, 44, 50, 51, 53–55). In the Ghaap Group in South Africa (2.67-2.52 Ga), bulk $\delta^{15}N_{bulk}$ values have a mean of +4.6 ± 2.0 ‰ and show no systematic variation between different facies, which include shallow-water microbialites and deeper-water siliciclastic

sediments (4). These results were interpreted as evidence of aerobic nitrogen cycling (4), implying that nitrate had become a significant ion in the surface ocean at this time. Across the Archean-Proterozoic boundary in the Hamersley Group in Western Australia (2.50-2.46 Ga), combined data sets from Garvin *et al.* (3) and Busigny *et al.* (113) capture offshore marine facies from the outer shelf and the shelf edge, respectively, and in both settings values are mostly above +4 ‰, especially after the 'whiff of oxygen' at 2.5 Ga (3, 5, 6). Although data from contemporaneous shallow marine sediments are not available, these fairly heavy values in offshore sediments are distinct from the comparatively light values found in the Mesoproterozoic ((24), this study) and provide strong evidence for a significant reservoir of nitrate throughout the surface ocean at the end of the Archean and extending into the early Paleoproterozoic. From the late Paleoproterozoic, Godfrey *et al.* (72) analyzed drill-core samples along a basinal profile in the Animikie Group (1.87-1.84 Ga) and reported a subtle gradient of 1.0-1.4‰ from onshore to offshore, the latter being slightly lighter, but nearly all their values (98%) were above +3‰ irrespective of environment. Hence nitrate was probably relatively abundant in the surface ocean across all environments in the Animikie basin. This may also have been the case in most of the Neoproterozoic where bulk $\delta^{15}N$ values are mostly above +2 ‰ and show no systematic basinal gradient (125). From the late Neoproterozoic onwards, nitrate depletion is only reported during temporary anoxic events (197–204); throughout most of the Phanerozoic the nitrogen cycle seems to have been predominantly aerobic with little spatial variance (187). Hence the Mesoproterozoic basins analyzed in this study appear to be anomalous in displaying subtle but significant facies-dependent variation in nitrogen isotopes and, by inference, nitrogen speciation.

We cannot rule out the possibility that this pattern is biased by latitudinal or oceanographic effects, because all of the Mesoproterozoic sites were originally located at low latitudes (< 30°,

(205, 206)) and in epicontinental seas, which could have enhanced stagnation and stratification of the water column. The Paleoproterozoic Animikie basin, on the other hand, formed at a higher latitude (>60°, (207)) possibly under colder temperatures, which would have favored downward mixing of oxidants produced in the upper ocean. Samples from other localities and better constraints on paleolatitude for other Precambrian basins would be needed to test this possibility.

The relatively light $\delta^{15}N_{bulk}$ values in offshore sediments from the Mesoproterozoic are unique and may have been a global characteristic of this time period (Figure 4.6). Figure 4.1 shows a compilation of bulk nitrogen isotopic compositions from offshore marine environments, highlighting the decline between ~1.7 Ga and ~1.2 Ga or possibly later. This interval post-dates the proposed mid-Paleoproterozoic oxygen overshoot (~2.3-2.0 Ga, (116, 118, 208, 209)) and has recently been identified as a time when atmospheric pO_2 may have dropped back to as little as 0.1% or as great as 4% (144, 210) of present atmospheric levels until a second, potentially protracted rise to nearer modern amounts across the Neoproterozoic/Paleozoic, possibly beginning at ~800 Ma (97, 211). Statistical analysis of global Fe-speciation data indicates that while subsurface anoxia was widespread throughout the Proterozoic Eon, euxinia was disproportionately common in Mesoproterozoic oceans (100), consistent with lower atmospheric oxygen levels. Marine sulfate concentrations are also thought to have declined after 1.7 Ga from ~10 mM to less than 1.8 mM, followed by a return to > 2-3 mM after 1.3 Ga (117, 119, 188, 212). Given that the redox potential of nitrate is intermediate between that of sulfate and oxygen (213), it is plausible that the abundance of nitrate in the surface ocean also declined in the mid-Proterozoic. This would have encouraged microbial N_2 fixation, leading to relatively low $\delta^{15}N_{bulk}$ values in offshore marine sediments (Figure 4.6). Nitrification of ammonium to nitrate requires oxygen, and so the production of nitrate was perhaps favored in shallow waters where O_2 was actively being produced.

In contrast, nitrification may have been suppressed further offshore where O_2 production was lower.

4.7.7 *Implications for life*

Both the Bangemall and the Roper basins have fossil assemblages that are consistent with an onshore-offshore trend of decreasing organismic diversity and abundance seawards (93, 94). Stüeken (24) suggested there could be a linkage between the basinal nitrate gradient observed in the Belt basin and the fossil distributions in the Bangemall and Roper basins, if they also had a nitrate gradient. Although our data are inconsistent with complete nitrate depletion offshore in the Roper and Bangemall basins (unlike in the Belt basin), several features of our results indicate that nitrate concentrations were probably significantly lower than in the Paleoproterozoic, Neoproterozoic, and modern ocean. First, $\delta^{15}N$ values were below +3‰ in offshore Mesoproterozoic sediments compared to +4‰ to +5‰ in the Cenozoic and modern (179, 187) (Figure 4.6), which likely reflects a mixture of two biological inputs from nitrate-assimilating organisms ($\delta^{15}N > 0‰$) and diazotrophs ($\delta^{15}N \sim 0‰$). The latter would not have been ecologically significant if nitrate had been abundant because N_2 fixation is energetically costly. Second, the lightest $\delta^{15}N_{bulk}$ data from the peritidal facies suggest rapid nitrate depletion and domination by N_2 fixers during temporary restriction from the marine nitrate reservoir. This is consistent with microfossil evidence from the Bangemall basin peritidal facies where *Palaeopleurocapsa* which resembles a modern genus of nitrogen-fixing cyanobacteria (Section 4.4.1) is found (94). Further support comes from biomarker evidence from the late Mesoproterozoic Taoudeni basin (1.1 Ga), which indicates that even some shallow waters during the Mesoproterozoic could have also been deficient in oxidized nitrogen species (214). Lastly, the variability in $\delta^{15}N$ throughout the basins

is best explained by a small nitrate reservoir whose relative size and isotopic composition were easily perturbed. Similar variability is seen in sulfur isotopes from the Mesoproterozoic, which is interpreted as an artifact of a small sulfate reservoir (188, 215). It is likely that the magnitude of nitrogen speciation trends varied between different basins; nevertheless all the currently available nitrogen isotope data point towards generally low Mesoproterozoic nitrate concentrations in the surface ocean with a minimum in offshore waters.

If so, then nitrogen availability may have contributed to the ecological distribution of marine organisms. As photosynthetic eukaryotes are apparently outcompeted by prokaryotes in nitrate-limited environments (103–107, 216, 217), it is likely that the open ocean was dominated by prokaryotic organisms with eukaryotes perhaps only inhabiting the most oxygenated part of the water column. Nearer shore, a more diverse ecosystem including abundant eukaryotes may have developed in relatively nitrate-rich waters. The very shallowest peritidal settings may again have excluded eukaryotes, not because of anoxia but due to periodic nitrate depletion during intervals of restricted water exchange at low tides. This ecological gradient may have also had evolutionary consequences in that eukaryote diversification was not possible in offshore and onshore nitrate-poor settings but was instead confined to near-shore waters that were relatively nitrate-rich. It is also possible that eukaryotic life was inhibited directly by episodic upwelling of anoxic and sometimes sulfidic waters (218); these two mechanisms of eukaryotic inhibition are not mutually exclusive and likely both occurred. If so, then perhaps eukaryotes underwent a major evolutionary radiation and rise to ecological dominance only after a Neoproterozoic oxygen increase, resulting in globally prevalent nitrification and deeper or less widespread anoxic water masses. Thus, our data support the hypothesis of Anbar & Knoll (92) that nitrogen availability may have been a key constraint on the evolution of eukaryotes.

4.8 *Conclusion*

Nitrogen isotope data from the Bangemall and Roper basins, considered in concert with the Belt basin (24), are consistent with the idea that distinct facies-dependent nitrogen regimes (largely aerobic near-shore and partially to fully anaerobic offshore) were a common feature in the early Mesoproterozoic. Peak enrichment in $\delta^{15}N_{bulk}$ occurs in shallow and peritidal depositional environments and cannot solely be explained by post-depositional alteration. There is no apparent systematic cross-basin bias of oxic versus anoxic diagenesis or metamorphism, so it is likely that these heavy values reflect the primary isotopic composition of biomass forming in the water column. The most plausible explanation for positive $\delta^{15}N_{bulk}$ values in the shallower waters is that a pool of dissolved nitrate was partially denitrified and the residual isotopically heavy nitrate was subsequently assimilated into biomass, as in the modern ocean (e.g. 76). Instances of light $\delta^{15}N_{bulk}$ in peritidal environments probably represent transient periods of isolation from the marine nitrate supply at low tide leaving fixation as the primary source of nitrogen. Light $\delta^{15}N_{bulk}$ values in deep water samples are consistent with a predominance of N_2 fixation by the Mo-Fe nitrogenase; slightly heavier samples likely record mixing with biomass from nitrate assimilators during intervals when nitrate was more available in the surface ocean, as in parts of the modern redox-stratified Cariaco basin (219). Such mixing implies that nitrate concentrations were low, because any isotopic signal from N_2 fixation would be erased without a nitrate deficit in the water column (122).

It is not clear whether the proposed spatial and temporal trends in nitrogen cycling indicate reduced concentrations of trace metals, oxygen, or both in deep water environments during the Mesoproterozoic where aerobic nitrogen cycling seems to have been limited. Our results are

consistent with metal-nitrogen co-limitation controlled by the extent of euxinic conditions (92, 98, 220), but probably only to a degree that limited nitrification and denitrification offshore while N_2-fixation by the Mo-Fe nitrogenase was able to persist. Our data are also consistent with a Mesoproterozoic oxygen decline (116, 117, 119, 209), as nitrogen isotopic ratios are lower in the Mesoproterozoic than in the Paleo- and Neoproterozoic, suggesting relatively lower nitrate concentrations. A basinal gradient of dissolved oxygen concentrations (higher near-shore to lower offshore) could potentially also produce the nitrogen isotopic trend seen in our datasets by limiting the extent of nitrification. Thus the theoretical prediction of two spatially separated states of the nitrogen cycle in the mid-Proterozoic (129) is now expressed in three different Mesoproterozoic basins, though how much this pattern directly depended on the location and extent of underlying euxinic waters is still unclear. Regardless, such patterns would probably have restricted eukaryote biomass and evolution to near-shore settings, as hypothesized by Anbar and Knoll (92), though the key limiting factor may not have been nitrogen fixation rates but nitrogen speciation.

4.9 *Acknowledgements*

We thank NSF EAR FESD grant #1338810 (RB), NASA grant NNX16AI37G (RB), the Agouron Institute (RB), the NASA Astrobiology Institute's Virtual Planetary Laboratory (RB), the NSF Graduate Research Fellowship Program (MAK), and the Department of Earth and Space Sciences, University of Washington Goodspeed Geology Fellowship (MCK), Misch Fellowship (MCK), and the Kenneth C. Robbins Field Study Fellowship (MCK) for funding, Andrew Schauer, Virginia Littell, and the University of Washington Isolab for technical support, and Simon Poulton for three additional Roper Group samples. We also thank Chris Reinhard, two

anonymous reviewers, and the associate editor James Farquhar for their comments that significantly improved this paper.

Chapter 5: NITROGEN AND CARBON BIOGEOCHEMISTRY ACROSS THE ORDOVICIAN-SILURIAN BOUNDARY AT DOB'S LINN, SCOTLAND

This manuscript will be submitted to the journal *Paleogeography, Paleoclimatology, Paleoecology*
Co-authored by Matthew C. Koehler, Eva E. Stüeken, and Tony Prave

5.1 *Abstract*

Marine ecology co-evolved with dramatic environmental change across the Ordovician-Silurian boundary. In particular, apparent trends in nitrogen cycling, both latitudinal and with respect to depositional environment, suggest extreme spatial-temporal heterogeneity in the availability of dissolved-nitrogen species associated with global climate change and mass extinction. Missing from these data-sets are analyses from the paleo-mid-latitudes and facies that represent the most distal continental margin. Here we present nitrogen and carbon isotope/abundance data from the O-S Global Boundary Stratotype Section and Point at Dob's Linn, Scotland. Nitrogen isotope and abundance data from bulk rock shale and bentonite samples as well as kerogen extractions indicate that unlike in tropical shallow-water sections, the sub-tropical locale at Dob's Linn shows no changes in nitrogen cycling associated with the Hirnantian glaciation, and suggest persistent nitrogen limitation. Diminishing oxygen minimum zones cause by increased ocean ventilation towards the end of the Ordovician apparently increased bioavailable nitrogen concentrations in shallow water tropical settings, alleviating nitrogen limitation in these environments. If perturbations to the nitrogen cycle in part *caused* the mass extinction and changes in climate, then these results highlight the importance of a climate-denitrification positive feedback in regulating the global environment. Carbonate data from this and other sections suggest a

deepening of the carbonate compensation depth during the Hirnantian which is also consistent with increased ocean ventilation. This indicates Pacific-style responses of the CCD to glacial/interglacial periods were operational across the O-S boundary, and that the expansion of deep-sea abiotic carbonate deposition and preservation could have in-part mediated changes to surface CO_2 during these extreme changes in climate.

5.2 *Introduction*

The Ordovician-Silurian (O-S) boundary is characterized by dramatic changes in Earth's climate, surface environments, and biosphere. It is generally thought that through the Ordovician, atmospheric pCO_2 levels and surface temperatures steadily decreased from greenhouse conditions (221), culminating in the Hirnantian glaciation. This climatic trend likely caused the progressive ventilation of the oceans due to stronger latitudinal temperature gradients (222), causing deep-ocean anoxia to diminish; a process that has been used in part to explain the Great Ordovician Biodiversification Event (GOBE; (223)). The initiation of the Hirnantian glacial period likely occurred when pCO_2 levels fell below a threshold level (224, 225), eventually resulting in the expansion of a Gondwanan ice sheet to volumes that rivaled or surpassed those of the Pleistocene Last Glacial Maximum (226). The beginning and end of the glaciation were punctuated by two mass extinction pulses that in combination eradicated 85 ± 3% of all marine invertebrate animal species (227). The close associations between global climate change and mass extinction pulses have led to the common view that the former caused the latter, but there are more recent data linking widespread ocean anoxia, not necessarily correlated with global climate change, to these extinctions (228). As with all documented mass extinction events, astronomic (e.g. 229, 230), geologic (e.g. 231–233), and biologic drivers (e.g. 234) have been proposed as mechanisms for

global environmental change and extinctions. Further insights into these cause-effect relationships can be gained from biogeochemical cycles.

The carbon isotope record from the Ordovician indicates periods of enhanced organic carbon burial, caused by increases in marine primary productivity (e.g. 235), leading to increased CO_2 sequestration from the atmosphere. The start of the largest magnitude carbon isotope excursion is documented from the early Hirnantian stage with a peak in the late Hirnantian, consistent with rapid CO_2 drawdown and global cooling. Sulfur isotopes from carbonate-associated sulfate and pyrite covary through the Ordovician, and recent interpretations of these records suggest more vigorous ocean ventilation by the middle Ordovician (222). Similar sulfur-redox records through the Hirnantian were initially interpreted as representing increased anoxia at the start of glaciation (236), but reevaluation of the single-reservoir model and independent proxies suggest that these records may indicate enhanced ocean ventilation and O_2 at the start of the Hirnantian (222).

It has been proposed that changes in the biogeochemical nitrogen cycle, specifically changes in the global rate of denitrification[6], in part contributed to the onset and termination of glaciation (237), as well as the abundance and distribution of prokaryotic and eukaryotic organisms in the global ocean (238–240). Nitrous oxide (N_2O) is a by-product of denitrification and a potent greenhouse gas, so decreases in the global denitrification rate caused by glacial eustatic sea-level fall or diminishing oxygen minimum zones could act as a positive cooling feedback by decreasing the N_2O flux to the atmosphere. Also, because denitrification removes bioavailable nitrogen (NO_3^- and NO_2^-) from the ocean, eukaryotic organisms that rely more heavily on the presence of fixed nitrogen in the form of nitrate may become advantaged if global rates of denitrification decreased.

[6] Denitrification is the biologically mediated reduction of oxidized nitrogen species (NO_3^-, NO_2^-) to N_2 gas through multiple intermediate nitrogen oxide products.

If such a feedback between climate, redox, and global rates of denitrification existed, then nitrogen cycling is inherently linked to the carbon cycle, and the mass extinctions pulses. It is worth noting that recent high-resolution uranium isotope data from across the O-S boundary suggests a decoupling between global ocean redox and eustatic sea-level/climate at the end-Hirnantian as the last mass extinction pulse is associated with an ocean anoxic event that begins during a sea-level high stand and lasted through a sea-level low stand (228). Importantly, this does not preclude a relationship between anoxia, the nitrogen cycle, and mass extinctions, but instead suggests climate and sea-level may at times be decoupled from these systems.

Nitrogen isotopic data from sections in present-day China (237), Canada (239), and USA (199) record nitrogen limitation in the paleotropics (~10^{o} N, ~15^{o} N, and ~5^{o} S respectively) spurred by widespread ocean anoxia and high rates of denitrification, before, near the end, and after the Hirnantian. During the Hirnantian, positive $\delta^{15}N$ excursions indicate temporary alleviation from nitrogen limitation in shallow tropical sections. Shallow-water sections from the high-paleolatitudes (~60^{o} S) in the present-day Czech Republic break from this pattern, showing positive $\delta^{15}N$ values from the Katian through the Hirnantian, suggesting persistent nitrate availability (239). The emerging spatial-temporal trends in nitrogen cycling from the available data suggest redox changes (the extent of oxygen minimum zones) across the O-S boundary affected nitrogen bioavailability in tropical shallow-water settings. Here, we add nitrogen and carbon isotope and abundance data from the O-S Global Boundary Stratotype Section and Point at Dob's Linn, Scotland. This is the first nitrogen isotope dataset from mid-latitudes across the O-S boundary, and is one of the deepest sections recording $\delta^{15}N$ values and transient increases in deep-sea carbonate abundances during the Hirnantian.

5.3 *Geologic setting*

Sample were collected from the Upper Hartfell Shale and the conformably overlying Lower Birkhill Shale formations of the Moffat Shale Group, located in the Central Belt of the Scottish Southern Uplands terrain. The ~11 meter section spans from the late Katian (Rawtheyan) to the Rhuddanian, and was sampled at ~30 cm resolution. The Upper Hartfell shale is a massive organic-lean (0.02% - 0.15% total organic carbon; TOC) grey shale with subordinate layers of organic-rich (1% - 2% TOC) graptolitic shale referred to as the *anceps* bands (241). These bands are reminiscent of the Lower Birkhill Shale, which is a laminated organic-rich (1.2% - 2.0% TOC) graptolitic black shale with abundant disseminated and laminated pyrite. These formations at Dob's Linn have only been subjected to prehnite-pumpellyite facies metamorphism (242). The sampled section contains over 20 bentonite beds through both formations ranging from 1 cm to 12 cm in thickness. Seven of these beds were sampled for nitrogen and carbon analyses. Geochemical similarities between these bentonite horizons and bentonite beds deposited in eastern Baltica suggest a common volcanic source that transported ash more than 1200 km from modern-day Scandinavia, which was located on the eastern margin of the Iapetus paleo-ocean (243). This correlation has qualitatively led to the hypothesis that perhaps the Dob's Linn sediments were deposited near the middle of the Iapetus Ocean before its closing (243). Classic interpretations, however, suggest deposition on the eastern continental margin of Laurentia at 30^{o}S, north of the Iapetus suture, and on the more distal section of the continental slope (244, 245). This is perhaps more consistent with the micro-turbidite sedimentary structures in the Dob's Linn sediments (241, 244). Regardless, deposition at Dob's Linn represents the most distal-marine sedimentary package across the O-S to be analyzed for nitrogen isotopes.

5.4 *Methods*

5.4.1 *Sample preparation: bulk and kerogen isolates*

Bulk samples and kerogen extractions were prepared using standard methodology (e.g. 23, 24). Outcrop samples were cut into ~ 3 x 3 x 2 cm chips and weathering rinds were shaved off with a diamond tip saw to remove modern contaminants. The chips were then crushed with a steel pestle on a steel plate which were covered with clean aluminum foil between each sample. The resulting smaller chips and coarse powder were transferred to clean glass beakers that had previously been heated at 500ºC overnight to remove contamination. Each sample was then sonicated with ethanol for 2 minutes, followed by 2N HCl for ~20 seconds to further remove modern contaminants. The acid was rinsed from the sample three times with 18MΩ milli-Q water, and samples were covered and left in a ventilated oven at 60ºC until dry. Samples were then finely powdered using an aluminum oxide puck mill that was thoroughly cleaned with ethanol, 18MΩ milli-Q water, and pre-combusted silica sand between each sample. Sample powders were stored in clean glass scintillation vials. Before analysis, bulk shale and bentonite samples were decarbonated using the methodology outlined in Section 5.4.3.

Methods for kerogen extractions were adapted from (25). Depending on organic carbon abundance estimates, 1-4 grams of unacidified powder were weighed into 250ml Teflon bottles. 100ml of 50% v/v hydrofluoric acid (HF) were added to sample bottles to react overnight in a shaking water bath at 55ºC. The acid was then decanted after centrifugation, and next any resulting fluoride precipitates were eliminated by treating the samples with 100ml of saturated boric acid in 50% v/v HF overnight in a shaking water bath at 55ºC. The acid was decanted, and samples were rinsed 3 times with 200ml of 18MΩ milli-Q water. Kerogen was transferred from the Teflon bottles to clean glass scintillation vials, frozen, and then freeze-dried for two days.

5.4.2 *Analytical Methods*

$\delta^{15}N_{bulk}$, $\delta^{15}N_{kerogen}$, total nitrogen (TN), total organic carbon (TOC), and $\delta^{13}C_{org}$ data were measured using a Costech ECS 4010 Elemental Analyzer coupled via a Conflo III to a Thermo Finnigan MAT253 continuous-flow isotope-ratio mass spectrometer. Groups containing a maximum of 6 samples were bracketed by three in-house standards calibrated to reference materials USGS40 and USGS41 (26) that were used to calibrate both abundance and isotope analyses as well as to monitor accuracy within individual runs. A fourth in-house rock standard was used to monitor long-term precision. Average analytical accuracy for $\delta^{15}N_{bulk/kerogen}$ and $\delta^{13}C_{org}$ through all runs was 0.16 ± 0.16‰ and 0.08 ± 0.06‰ respectively, and average analytical precision was 0.11‰ and 0.02‰ respectively. The average standard deviation of sample replicates was 0.11‰ for all $\delta^{15}N$ measurements, and 0.15‰ for all $\delta^{13}C_{org}$ measurements.

$\delta^{13}C_{carb}$ and $\delta^{18}O_{carb}$ analyses were performed on unacidified sample powders using a Kiel III Carbonate Device coupled to a Delta V Plus Thermo Finnigan Isotope Ratio Mass Spectrometer. The Kiel parameters were set to a phosphoric acid temperature of 80°C, 10 drop acidification for each sample, and a reaction time of 10 minutes in order to digest more recalcitrant carbonates such as siderite. Internal calcite standards "C1" and "C2" that had been calibrated to international standards NBS19, LSVEC, and NBS18 were used to calibrate $\delta^{13}C_{carb}$ and $\delta^{18}O_{carb}$ values on the VPDB scale. A third quality control standard "CQS2" was used to track long term precision. In total, 15 standards were run with 20 samples from Dob's Linn. The average analytical accuracy based on all standards was 0.02 ± 0.02‰ and 0.04 ± 0.03‰ for $\delta^{13}C_{carb}$ and $\delta^{18}O_{carb}$ respectively. The average analytical precision based on the in-house standard CQS2 was 0.02‰ and 0.05‰ for $\delta^{13}C_{carb}$ and $\delta^{18}O_{carb}$ respectively. The average standard deviation of sample

replicates was 0.1‰ for all $\delta^{13}C_{carb}$ measurements, and 0.2‰ for all $\delta^{18}O_{carb}$ measurements. Because all the standards are calcite, calcite was the assumed mineralogy when correcting the raw $\delta^{18}O_{carb}$ data for fractionation during phosphoric acid digestion. Fractionation factors during phosphoric acid digestion of carbonate vary depending on mineralogy (siderite, aragonite, dolomite, etc; , 246). If dolomite, siderite, or aragonite were the primary carbonate, the $\delta^{18}O_{carb}$ data presented here would only shift by approximately +1‰, and their relative values would remain the same (246).

5.4.3 *Percent carbonate*

The percent carbonate of our samples was initially calculated gravimetrically (e.g. 23, 24). Sample powders were acidified with 6 M HCl at 60ºC in three iterations over three days. They were then thoroughly rinsed three times with 18 Ω Milli-Q deionized water to remove the acid. The weight of the samples before and after the acidification was used to estimate percent carbonate. The resulting values were >10% greater than values measured by the Kiel device, prompting suspicion that the phosphoric acid in the Kiel was not properly digesting recalcitrant carbonate in the Dob's Linn samples.

Because recalcitrant carbonates such as siderite are notoriously hard to digest in phosphoric acid, special attention was given to conditions that will yield complete digestion (e.g. 247). To test if the Kiel III Carbonate Device was completely digesting all carbonates in our samples, we used a methodology similar to the "open vessel digestion" of Fernandez et al. (2016), which was shown to more rapidly digest siderite. Approximately 50 mg of two Dob's Linn samples were weighed into separate Pyrex reaction tubes. Room-temperature phosphoric acid was added to the reaction tubes but did not interact with the sample at the bottom of the tube because of its high viscosity.

Reaction tubes were then attached to a vacuum line to remove the headspace, and subsequently flame-sealed. They were then vortexed to mix the acid with the sample and placed in an oven overnight at 100ºC. The tubes were intermittently vortexed during the hot digestion period to ensure the acid was completely mixing with the sample. After the digestion period, the tubes were cracked on a vacuum line and gasses were cryogenically cleaned to isolate the CO_2 produced by the digestion. The amount of CO_2 produced by the digestions was then measured manometrically.

5.5 *Results*

5.5.1 *Carbonate*

The two Dob's Linn samples that were reacted with phosphoric acid overnight at 100ºC and measured manometrically are within 1% of the percent carbonate values produced by Kiel analysis, suggesting that the Kiel carbonate values are reliable. This means the gravimetrically-determined carbonate abundances were inaccurate (overestimating by more than 10%), likely due to the dissolution of non-carbonate species by the hot concentrated HCl. As a result, all carbonate values (isotopes and abundances) discussed below refer to the Kiel-measured values.

5.5.2 *Nitrogen and carbon*

The lithological change between the Upper Hartfell and Lower Birkhill is driven by changes in the abundance of organic matter. TOC [%] is on average an order of magnitude greater in the Lower Birkhill (1.6 ± 0.3) than in the Upper Hartfell (0.11 ± 0.11). Because the C/N [atomic] ratios of organic matter are similar - and the abundance of silicate-bound nitrogen is invariant -

through both formations, the fraction of nitrogen bound in organic matter ($F_{kerogen}$)[7] rather than in silicates is an order of magnitude greater in the Lower Birkhill (26.2 ± 3.6%) than in the Upper Hartfell (2.8 ± 2.6%). In both formations, silicate-bound nitrogen is the dominant nitrogen fraction. This is especially true for the bentonite samples, where TOC [%] values are comparable to Upper Hartfell shale, but TN [%] values are approximately triple those from shale samples. (Figure 5.3 and Figure 0.12). Because the silicate-bound nitrogen fraction is large and silicate-bound nitrogen abundances are invariant in the Upper Hartfell and bentonite samples, it is no surprise that bulk C/N [atomic] ratios are strongly correlated to TOC [%] in these samples (Figure 0.13). This correlation is much weaker in the Lower Birkhill because the variability in organic matter C/N [atomic] ratios in this more organic rich formation contributes more significantly to bulk C/N [atomic] values. Carbonate [%] in bulk shale samples are all below 1% (the limit of detection for these runs) except during the middle Hirnantian where values peak at 23% (Figure 5.3).

$\delta^{15}N_{bulk}$ measurements through both the Upper Hartfell Shale and Lower Birkhill Shale are relatively invariant and range from +0.7‰ to -0.1‰ (Figure 5.1a and Figure 5.2). $\delta^{15}N_{bulk}$ measurements from the bentonite horizons are equally invariant and on average slightly more negative, ranging from -0.47‰ to -1.25‰. $\delta^{15}N_{kerogen}$ measurements through both formations are more varied, ranging from -6.0‰ to +1.3‰, with seven out of ten samples containing $\delta^{15}N_{kerogen}$ values that are >1‰ more depleted than $\delta^{15}N_{bulk}$ values of the same sample (Figure 5.1e and Figure 5.2).

$\delta^{13}C_{org}$ measurements from the shales agree with those of previous studies (e.g. 248, 249), with values up to -29.3‰ during the middle Hirnantian, followed by a steady decrease to more depleted values averaging -32.8‰ starting at the lithological boundary to the Birkhill Shale (Figure

[7] $F_{kerogen} = 1 - F_{silicate} = \frac{N\,[\%]_{kerogen}}{C\,[\%]_{kerogen}} \times \frac{TOC\,[\%]_{bulk}}{TN\,[\%]_{bulk}}$

5.2). One $\delta^{13}C_{org}$ measurement in the Rawtheyan is enriched to a similar magnitude (-29.1‰), also corroborating a prior study (248). Bentonite samples are all enriched in $\delta^{13}C_{org}$ compared to adjacent shale samples, ranging from -26‰ to -30‰ (Figure 5.1c). Differences between kerogen and bulk shale $\delta^{13}C_{org}$ measurements of the same sample are all less than 0.5‰. $\delta^{13}C_{carb}$ and $\delta^{18}O_{carb}$ values for these carbonates average -4.9 ± 0.4 ‰ and -5.3 ± 0.3 ‰ respectively (Figure 0.11).

5.1 *Discussion*

5.1.1 *Potential for post-depositional alteration*

Post-depositional alteration of nitrogen and carbon isotopes can occur during diagenesis and metamorphism. To interpret our data as primary biological and environmental signals, these effects need to be addressed.

5.5.2.1 Diagenesis

Depending on the redox state of the water column and marine sediments, diagenesis can have varying effects on both carbon and nitrogen isotope ratios. In modern marine sediments, residual organic nitrogen is often enriched in ^{15}N as a result of preferential ^{14}N loss during oxic diagenesis (e.g. 31, 33, 34). The magnitude of this enrichment depends on the sediment redox state and sedimentation rates, with greater enrichments (3‰ - 4‰) occurring in oxic sediments with low sedimentation rates. These enrichments approach 0‰ in anoxic sediments with high sedimentation rates (157). Depletion of ^{15}N in residual organic nitrogen after diagenesis has been observed in a few modern marine environments (e.g. 35, 36), and during laboratory experiments (32). The mechanism for depletion is thought to be the addition of ^{15}N-depleted biomass through the *in-situ* growth of N_2-fixing bacteria that have an isotopic composition of -2‰ to +1‰. Of course, this

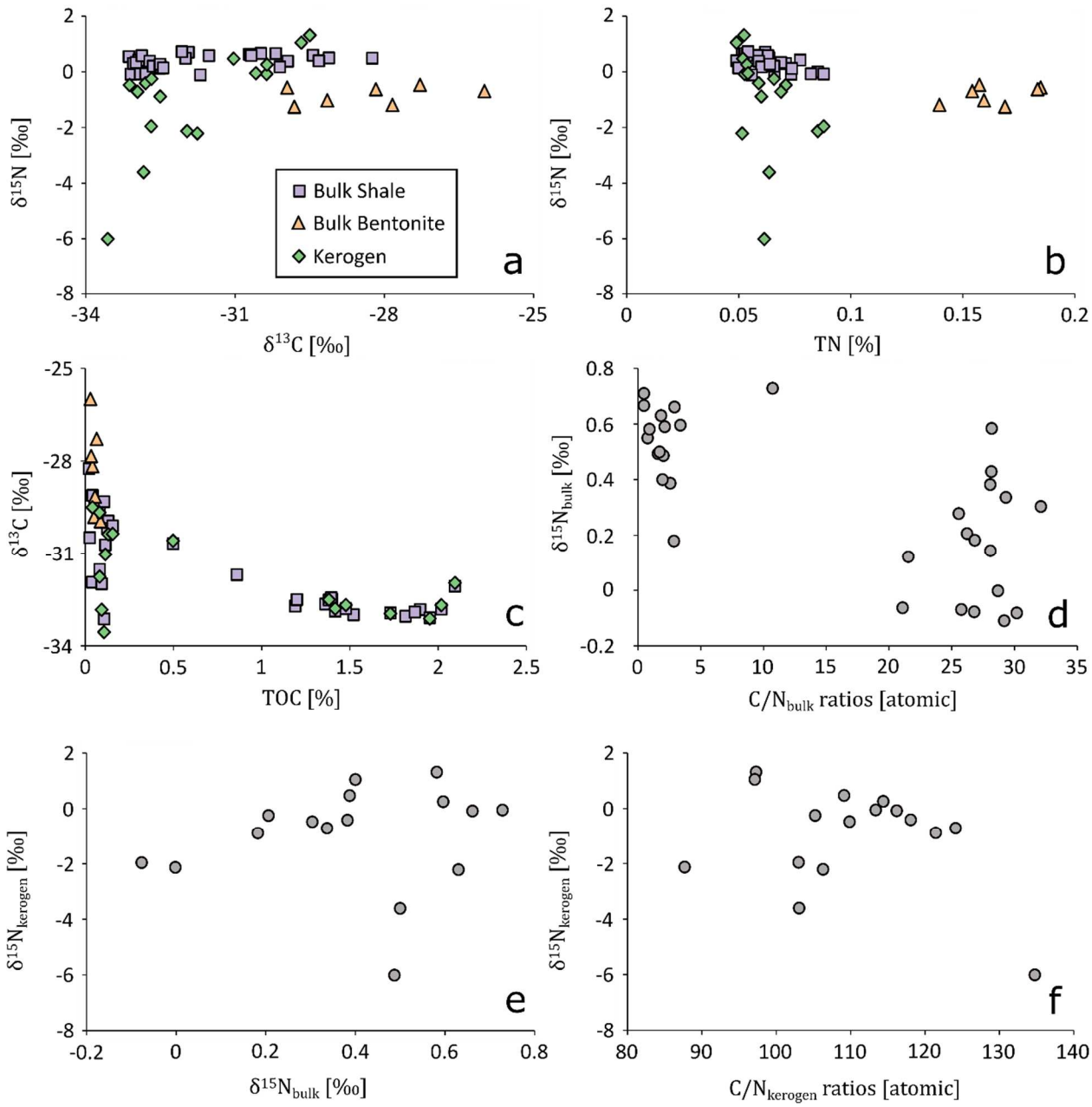

Figure 5.1**. Cross-plots of nitrogen and organic carbon isotopes, abundances, and ratios from Dob's Linn shales, bentonites, and kerogen isolates.** Grey dots are sample measurements that follow the axes labels.

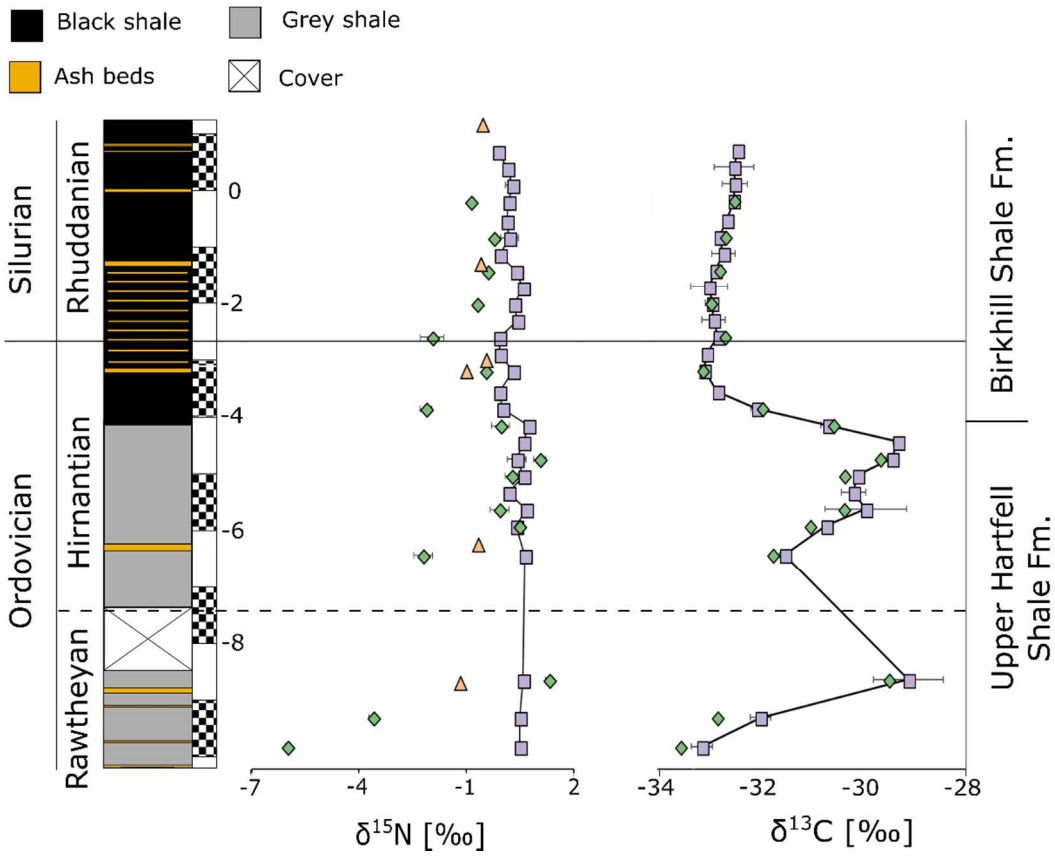

Figure 5.2**. Nitrogen and organic carbon isotope chemostratigraphy through the Dob's Linn section.** Symbols for bulk shale, bentonite, and kerogen measurements are as in Figure 5.1.

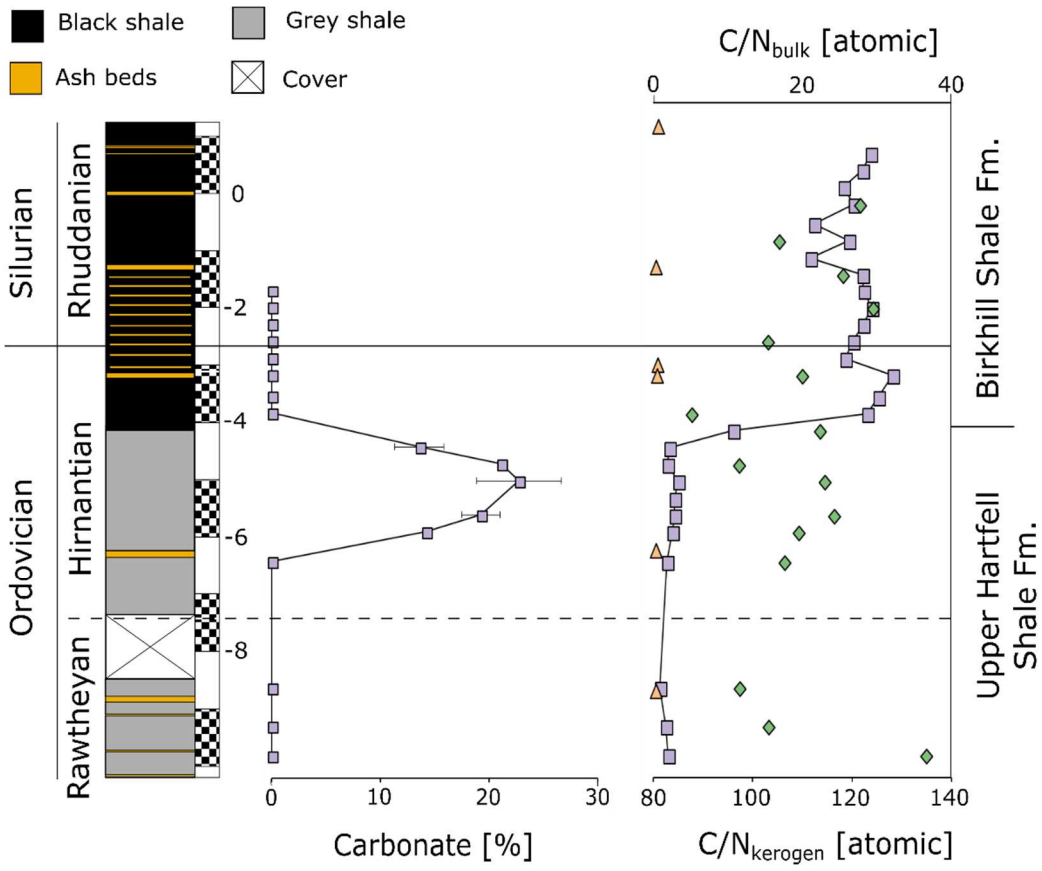

Figure 5.3**. Nitrogen and organic carbon chemostratigraphy through the Dob's Linn section.** Symbols for bulk shale, bentonite, and kerogen measurements are as in Figure 5.1.

would only cause a depletion of ^{15}N in residual organic nitrogen if the organic matter was originally enriched in ^{15}N; *i.e.* biomass dominated by N_2-fixers is unlikely to be isotopically altered by the addition of biomass from more N_2-fixers. Iron speciation data from Dob's Linn tell an inconclusive story regarding bottom-water redox conditions through this section, because they straddle the empirically-defined oxic-anoxic boundary (236). It is possible that during the Rawtheyan, sediments were deposited under more oxic conditions than during the Hirnantian and Rhuddanian. However, systematic trends in diagenetic alteration of original $\delta^{15}N$ values are difficult to evaluate due to apparent nitrogen migration and $\delta^{15}N$ homogenization through this section (see section 5.5.2.3). If our rough calculations of original Upper Hartfell $\delta^{15}N$ values are correct (section 5.5.2.3), then the lack of $\delta^{15}N$ variability through the section suggests that preferential large scale diagenetic changes to any part of the studied section are unlikely.

Carbonates preserved in the middle Hirnantian sediments at Dob's Linn have relatively light $\delta^{13}C_{carb}$ and $\delta^{18}O_{carb}$ values suggesting that some of the carbonate formed diagenetically from respired biomass. Using average Hirnantian $\delta^{13}C_{carb}$ and $\delta^{13}C_{org}$ values from other coeval sections (0‰ to +5‰ and -28‰ respectively; , 239) and the average $\delta^{13}C_{carb}$ value from Dob's Linn, mass balance predicts ~20% to 30% of the carbon in the Dob's Linn carbonates comes from respired organic matter. This means that the carbonate may have formed during early diagenesis rather than syndepositionally. There is no correlation between carbonate abundance or $\delta^{13}C_{carb}$ and $\delta^{13}C_{org}$ values, suggesting that the $\delta^{13}C_{org}$ excursion is unlikely to be a result of carbon isotopic equilibration between organic matter and carbonate, which only occurs at higher grades above mid-greenschist facies (e.g. 165–167).

5.5.2.2 Metamorphism

The effects of sub-greenschist metamorphism on $\delta^{15}N$ values is thought to be < 2‰ (28, 29). Classic signs of metamorphic alteration include increasing $\delta^{15}N$ values correlated to increasing C/N ratios, and a divergence between $\delta^{15}N_{silicate}$ and $\delta^{15}N_{kerogen}$ values of a given sample. This is because nitrogen is more mobile than carbon and ^{14}N more mobile than ^{15}N under such conditions. There is no correlation between $\delta^{15}N$ and C/N ratios in the Dob's Linn data (Figure 5.1d and Figure 5.1f), but two samples display $\Delta^{15}N_{silicate\text{-}kerogen}$ value of greater than 4‰. In rocks of low metamorphic grade that have not undergone fluid alteration and migration of ammonium, $\delta^{15}N_{bulk}$ values are usually a good approximation for the original $\delta^{15}N$ values of deposited organic matter (29). However, the fact that all bentonite horizons are characterized by large TN [%] values, very low C/N ratios, and $\delta^{15}N_{bulk}$ values closely resembling the $\delta^{15}N_{kerogen}$ from the Lower Birkhill (Figure 5.1b) suggests that NH_4^+ may have been mobile after sediment deposition and may have homogenized silicate-bound $\delta^{15}N$ through the section (see below).

5.5.2.3 Diffusion/advection effects on $\delta^{15}N_{bulk}$

It is possible that $\delta^{15}N_{bulk}$ values through the section, particularly through the more organic-lean Upper Hartfell, do not strictly reflect the stratigraphically equivalent $\delta^{15}N$ of original organic matter. During the rapid deposition of bentonite horizons, TOC is expected to be low because the sedimentation rate greatly exceeds biomass burial. If silicate-bound nitrogen is sourced from stratigraphically equivalent organic matter, then TN in these bentonite horizons should be correspondingly low. TOC in the Dob's Linn bentonite horizons throughout the section (0.05% ± 0.02%) are indeed low (comparable to the Upper Hartfell), but TN values (0.16% ± 0.016) are triple and double those seen in Upper Hartfell and Lower Birkhill shales, respectively (Figure 5.1b and S2). This suggests that the bentonite beds were enriched in ammonium after deposition, which

is most parsimoniously explained by NH_4^+ diffusion through these sediments during illitization. The bentonite layers have higher TN values than the shale samples from the section because the bentonites have proportionally more illite. Given the consistent silicate-bound nitrogen abundances through both formations (0.053% ± 0.006, as illustrated by the linear relationship between the TOC [%] and C/N_{bulk} of samples from the Upper Hartfell and bentonite horizons shown in Figure 0.13), and the proportional increase observed in illite-rich bentonite horizons, it seems likely that the silicate-bound nitrogen fraction throughout the section was derived from fluids with similar NH_4^+ concentrations and $\delta^{15}N$ values.

A plausible source for this NH_4^+ may have been the organic-rich Birkhill Shale, where NH_4^+ may have been mobilized during diagenetic degradation of organic matter as is commonly observed in modern organic-rich sediments (e.g. 250, 251). In principle, NH_4^+ can also be sourced from the overlying water column in areas where deep waters are dominated by euxinia (252). This is because sulfate reduction cannot be thermodynamically coupled to NH_4^+ oxidation and therefore leads to accumulation of dissolved NH_4^+. However, iron speciation data from Dob's Linn record possible hints of euxinia only in the early Silurian but not during the Ordovician, *i.e.* long after the deposition of the first ash beds (Hammarlund et al. 2012). It is therefore unlikely that the NH_4^+ in the bentonites was directly absorbed from the water column during deposition. Post-depositional NH_4^+ migration as described above is more likely. Importantly, the isotopic composition of the bentonites deviates by less than 1‰ from the surrounding sediments, including the Birkhill Shale, suggesting that NH_4^+ mobility and assimilation into secondary illite does not impart a significant isotopic fractionation.

We can estimate the percent of nitrogen in Upper Hartfell samples that is authigenic vs. derived from the Lower Birkhill using the following equation, if we assume the Upper Hartfell had a similar C/N [%] ratio to the Lower Birkhill before the addition of allogenic nitrogen:

$$TN_{auth.hartfell} = \frac{TOC_{hartfell}}{TOC_{birkhill} \div TN_{birkhill}} \qquad (5.1)$$

where $TN_{auth.hartfell}$ is the nitrogen percent of the bulk sample that is estimated to be indigenous in an Upper Hartfell sample, $TOC_{hartfell}$ is the total organic carbon percent of an Upper Hartfell sample, and $TOC_{birkhill}$ and $TN_{birkhill}$ are the average organic carbon percent and average total nitrogen percent of Lower Birkhill shale samples respectively. Knowing the total nitrogen percent of the bulk sample ($TN_{bulk.hartfell}$) we can then calculate the fractions of authigenic and allogenic nitrogen in Upper Hartfell samples:

$$\frac{TN_{auth.hartfell}}{TN_{bulk.hartfell}} = F_{N.hartfell} = 1 - F_{N.birkhill} \qquad (5.2)$$

Using these calculations on all Upper Hartfell samples, we see that 93% ± 3 of the nitrogen is likely allogenic, derived from then Lower Birkhill. We can explore estimates for the original nitrogen isotopic composition of both these fractions using the following equations:

$$\delta^{15}N_{birkhill} = \frac{[\delta^{15}N_{bulk.hartfell} - (F_{N.hartfell} * \delta^{15}N_{original.hartfell})]}{F_{N.birkhill}} \qquad (5.3)$$

$$\delta^{15}N_{hartfell} = \frac{[\delta^{15}N_{bulk.hartfell} - (F_{N.birkhill} * \delta^{15}N_{estimated.brikhill})]}{F_{N.hartfell}} \qquad (5.4)$$

where $\delta^{15}N_{birkhill}$ and $\delta^{15}N_{hartfell}$ are the nitrogen isotopic compositions of the allogenic (derived from the Lower Birkhill) and authigenic fractions respectively, $\delta^{15}N_{bulk.hartfell}$ is the bulk nitrogen isotopic value of an Upper Hartfell sample, $\delta^{15}N_{original.hartfell}$ is an estimate of the authigenic nitrogen isotope composition, and $\delta^{15}N_{estimated.birkhill}$ is an estimate of the nitrogen isotopic composition of mobile NH_4^+ derived from the Lower Birkhill.

If we assume $\delta^{15}N_{original.hartfell}$ is best approximated by the $\delta^{15}N_{kerogen}$ values from the Upper Hartfell (ranging from -6.0‰ to +1.3‰), then using equation 5.3 would yield $\delta^{15}N_{birkhill}$ values ranging from 0.35‰ to 1.0‰, which is exactly the range of measured Lower Birkhill $\delta^{15}N_{silicate}$ values. However, $\delta^{15}N_{birkhill}$ is so insensitive to $\delta^{15}N_{original.hartfell}$ that when using average $\delta^{15}N_{bulk.hartfell}$, $F_{N.birkhill}$, and $F_{N.hartfell}$ from the Upper Hartfell, $\delta^{15}N_{original.hartfell}$ values ranging from -10‰ to +35‰ would yield $\delta^{15}N_{birkhill}$ values within the range of all $\delta^{15}N$ values measured from the Lower Birkhill (from -2‰ to +1‰). Because of this, it is less informative to guess at authigenic Upper Hartfell $\delta^{15}N$ values in order to estimate the $\delta^{15}N$ value of NH_4^+ exported from the Lower Birkhill to the Upper Hartfell.

Perhaps the best approximation of these fractional $\delta^{15}N$ values is to calculate $\delta^{15}N_{hartfell}$ (equation 5.4) by using the average $\delta^{15}N_{silicate}$ of the Lower Birkhill as $\delta^{15}N_{estimated.birkhill}$. This is because the $\delta^{15}N_{silicate}$ of the Lower Birkhill most likely represents the mobile NH_4^+ in pore fluids that was incorporated into the Lower Birkhill silicates, and that eventually diffused down into the Upper Hartfell. Doing this yields $\delta^{15}N_{hartfell}$ values between -2.5‰ and +1.0‰. Importantly, this range encompasses almost all $\delta^{15}N$ values measured from the Upper Hartfell (bulk and kerogen). If instead average $\delta^{15}N_{bulk}$ and $\delta^{15}N_{kerogen}$ from the Lower Birkhill are used as $\delta^{15}N_{estimated.birkhill}$, the estimated $\delta^{15}N_{hartfell}$ ranges widen to +2.6‰ to +12.8‰ and +11.7‰ to +45.5‰ respectively. Most of these values are unfeasibly high compared to the rest of the Paleozoic, and so the average $\delta^{15}N_{silicate}$ of the Lower Birkhill appears to be the best estimate of mobile NH_4^+, and so also the allogenic nitrogen component in the Upper Hartfell.

5.5.3 *Interpretation of nitrogen isotopes*

It is clear from mass-balance calculations that most of the nitrogen within Upper Hartfell samples are derived from the organic-rich Lower Birkhill where NH_4^+ was mobilized in pore fluids and permeated the rest of the section. Using the range of $\delta^{15}N_{silicate}$ values measured from the Lower Birkhill to estimate the $\delta^{15}N$ values of permeating NH_4^+ yields calculated $\delta^{15}N$ values of indigenous Upper Hartfell nitrogen ranging from -2.5‰ to +1.0‰. Most $\delta^{15}N_{kerogen}$ values from the Upper Hartfell, another estimation of indigenous $\delta^{15}N$ values, fall within this range. Using this range of values as characteristic of the Upper Hartfell, it seems almost all nitrogen isotope values (both bulk and kerogen measurements) from the Dob's Linn section fall within the window attributed to nitrogen fixation by the Mo-nitrogenase (-2‰ to +1‰).

This precludes the presence of a large nitrate pool because coupled nitrification and partial water column denitrification produce isotopically light N_2 and isotopically heavy residual nitrogen (e.g. NH_4^+, NO_3^-), so long as these metabolisms do not fully convert the bioavailable nitrogen to N_2. The isotopically heavy residual is reflected in biomass as $\delta^{15}N$ values greater than +1‰; e.g. the modern ocean nitrate average is +5‰ (76). So the measured values between -2‰ to +1‰ at Dob's Linn suggests that bioavailable nitrogen may have been persistently limited in this offshore environment across the O-S boundary. This limitation was likely due to (i) rapid conversion of NH_4^+ to NO_3^- in the photic zone, and (ii) rapid rates of denitrification that quantitatively converted all NO_3^- to N_2, depleting bioavailable nitrogen and giving nitrogen fixers an ecological advantage (237).

The same nitrogen isotope trend is observed across the O-S boundary at Vinini Creek (Nevada, USA), which was also deposited beyond the continental shelf (199). The addition of the Dob's Linn nitrogen data highlights the spatial-temporal trends in nitrogen cycling presented in

Luo et al., (2016). Though the scarcity of sections measured for nitrogen isotopes across the O-S boundary prohibits confident reconstructions of the global ocean at that time, it appears that within each age (Katian, Hirnantian, and Rhuddanian) there are statistically significant differences in $\delta^{15}N$ values between sections at different latitudes and depositional environments (Table 5.5, Figure 5.4).

This perhaps is not surprising, because latitudinal trends in marine nitrogen cycling are observed in the modern ocean. Higher oxygen concentrations in high-latitude waters on the modern Earth inhibits water column denitrification (a reaction requiring suboxic-anoxic waters), resulting in higher nitrate concentrations (31). These latitudinal trends are primarily driven by physical oceanographic processes that should have operated ~425 My ago; colder polar and subpolar waters have higher oxygen solubilities and stronger high-latitude winds drive more vigorous vertical water column mixing (253). It should then be expected that higher-latitude waters in the Ordovician ocean were more nitrate-rich. To continue with the analogy of global oceanic nitrogen cycling trends between the modern and Ordovician, the apparent diametric response in nitrogen isotopes must be addressed.

In the modern ocean there is a negative correlation between nitrate concentration and the $\delta^{15}N$ of suspended and sedimentary particulate nitrogen (PN) (31). The increased oxygen concentration near the poles makes it so water column denitrification is inhibited, resulting in less nitrate ^{15}N enrichment as there is little preferential loss of the light isotope through the partial conversion of nitrate to ^{15}N-depleted N_2. As waters move towards the equator, oxygen minimum zones form where O_2 demand outpaces O_2 supply. It is in these zones where nitrate is partially converted into ^{15}N-depleted N_2, depleting the nitrate while raising its $\delta^{15}N$ value. These oxygen minimum zones make up a relatively small portion of the modern ocean, and there are few

instances of quantitative denitrification that allow for nitrogen fixation to dominate. Because of this, water column denitrification and nitrogen fixation are often decoupled in the modern ocean (31, 253). What results are areas with the lowest nitrate concentrations in the modern ocean tend to have the largest $\delta^{15}N$ values.

During the Ordovician, however, the pO_2 in the atmosphere and dissolved oxygen concentrations in the ocean were likely lower than modern (100, 254). Suboxic and anoxic waters made up a larger portion of the ocean and as a result water column denitrification was likely more vigorous in oxygen minimum zones, leading to more areas of quantitative denitrification. $\delta^{15}N$ values in this instance likely had a positive rather than negative correlation with nitrate concentrations because zones of intense water column denitrification would have been coupled to zones of nitrogen limitation and nitrogen fixation. Outside these areas of quantitative denitrification, which likely occurred in upwelling zones, open ocean PN $\delta^{15}N$ values depended on local areas of partial water column denitrification, and more restricted shallow-marine basin PN $\delta^{15}N$ values depended on the N:P ratios of advected marine waters (253). The N:P ratio of advected seawater controlled which nutrient was limiting, and so whether nitrogen fixation could dominate.

High-latitude sections across the O-S boundary showing consistent $\delta^{15}N$ values averaging +3‰ suggest either (i) persistent local partial water column denitrification, or (ii) high oxygen concentrations in polar/subpolar waters inhibited water column denitrification, as observed in the modern ocean, and the enriched $\delta^{15}N$ values resulted from spatially-removed zones of partial water column denitrification. The sub-tropical and equatorial records from Dob's Linn and Vinini Creek represent persistent oxygen minimum zones across the O-S boundary, locally depleting fixed nitrogen allowing for the local ecological dominance of nitrogen fixers (199). This is consistent

with recent evidence that suggests ocean anoxia through this period was focused in these more offshore environments (228).

But what specifically drove the temporal changes in $\delta^{15}N$ values from equatorial shallow-marine environments across the O-S boundary? To address this, we can look toward how nitrogen cycling in the modern ocean responded to climate change over the last 300 kyrs. A first order control on the extent of global denitrification is high-latitude O_2 supply to the global thermocline, which is again controlled by oxygen solubility and wind-controlled rates of thermocline circulation (253). During glacial periods, colder, more oxygenated waters entered a more rapidly circulating thermocline driven by stronger winds. The increased O_2 supply from these waters towards the equator diminished oxygen minimum zones and global rates of denitrification. What resulted were waters with relatively higher average N:P ratios that when supplied to equatorial shallow-marine basins would (i) limit nitrogen fixation as primary productivity was instead limited by phosphorus, (ii) favor a significant steady-state nitrate pool, and (iii) yield more positive $\delta^{15}N$ values through either local partial water column denitrification or a higher average $\delta^{15}N$ value of the advected nitrogen. This response has been observed in the eastern Mediterranean, where $\delta^{15}N$ records indicate more nitrogen replete conditions during glacial periods, and nitrogen limitation with significant contribution from nitrogen fixers in interglacial periods (253). The eastern Mediterranean is ultimately supplied by water from the Atlantic Ocean. In coeval $\delta^{15}N$ records from deeper non-restricted Atlantic Ocean sections, $\delta^{15}N$ values were higher due to enhanced - but non-quantitative – local water column denitrification during interglacial periods, suggesting lower N:P ratio waters from the Atlantic were being fed into the eastern Mediterranean, causing nitrogen limitation and spurring nitrogen fixation (253). The opposite relationship is recorded in glacial periods.

It is important to note two mechanisms that superimpose spatial heterogeneity on nitrogen cycling/isotopes in the global ocean: (i) local primary productivity (oxidant demand), and (ii) proximity to zones of denitrification and fixation. Locations in the ocean removed from zones of denitrification and fixation do not necessarily record any $\delta^{15}N$ fluctuations during glacial-interglacial cycles over the last 300 kyrs and would not necessarily fluctuate across the Hirnantian glaciation.

In summary, the positive nitrogen isotope excursions in shallow equatorial records indicate that ocean waters in general were more nitrogen rich in the Hirnantian than during the Katian and Rhuddanian due to the climatically-driven reduction in oxygen minimum zones and rates of denitrification as described above. Introduction of waters with relatively higher N:P ratios into more restricted shallow-marine basins created a nitrogen excess that is reflected as positive $\delta^{15}N$ excursions in these sections. Either fixed nitrogen $\delta^{15}N$ values were on average globally higher due to increased *partial* water column denitrification during the Hirnantian, or shallow-water marine environments hosted local partial water column denitrification leading to the more positive Hirnantian $\delta^{15}N$ values. Either way, these data support climatically-driven changes to the global oceanic nitrogen cycle. If these changes do in fact represent major perturbations to global rates of denitrification, transiently low denitrification rates and accompanying low N_2O fluxes (a potent greenhouse gas) during the Hirnantian could have acted as a positive feedback for global cooling (237).

It is worth noting that depositional environment trends in $\delta^{15}N$ values within these ages are reminiscent of basinal gradients detected at other times in Earth's history that are characterized by large ocean redox heterogeneity, such as in the Mesoproterozoic (23, 24). Statistical consideration of iron speciation data from mid-Proterozoic to Paleozoic outer shelf/basinal samples suggests no

difference in the proportion of anoxic bottom waters through this time, and also similarities between the Mesoproterozoic and Paleozoic in the proportion of anoxic bottom waters that were sulfidic (100). Because redox state - the extent and vigor of oxygen minimum zones - seems to exert a primary control on spatial-temporal trends in nitrogen cycling, it may not be surprising that the two periods have closely related $\delta^{15}N$ values (Figure 5.5). Relatively low $\delta^{15}N$ values in the Mesoproterozoic, when compared to the Neo- and Paleoproterozoic, have previously been interpreted as reflecting a temporal minimum in oceanic nitrate concentrations. It is possible that periods in the Paleozoic like the O-S boundary are similarly characterized by low oceanic nitrate, even when nitrate concentrations should be at a maximum during the Hirnantian glaciation.

5.5.4 *Carbon cycling*

The trend in deep-sea carbonate deposition at Dob's Linn mirrors trends observed in the Pacific Ocean during glacial-interglacial cycles over the past 300 kyrs. As originally recognized in the Pacific ocean (255), it is evident that the marine carbonate compensation depth[8] (CCD) responds to changes in global climate (e.g. 256–258). Such responses have been extensively documented through the Cenozoic, particularly during the Quaternary where proxies from deep sea sediment cores record changes in carbonate preservation (259, 260), CO_3^{2-} concentrations (261), and carbonate dissolution rates (262, 263) that correlate to climate proxies. The timing of these correlations is well known: carbonate accumulation in sediments is at a maximum during late glacial periods and early deglaciation (262, 264).

[8] The carbonate compensation depth is the depth in the water column where carbonate dissolution balances carbonate production, such that no carbonate accumulates in sediments below this depth.

There has been contention, however, regarding the mechanisms that drive these observed changes in deep-water carbonate accumulation (e.g. 265); is the dominating control changes to $CaCO_3$ biogenic sources, or changes to carbonate preservation (i.e carbonate dissolution/sinks)? Recently evidence has been piling up in support of preservation control on deep-sea $CaCO_3$ accumulation (265). $CaCO_3$ preservation is dominantly controlled by the saturation state of CO_3^{2-}, where the degree of over/under-saturation controls the degree of preservation/dissolution. During glacial periods over the past 300 kyrs, increased CO_3^{2-} concentrations in mid to deep waters slowed carbonate dissolution, resulting in more carbonate accumulation in deep-sea sediments (265–268). Increases in CO_3^{2-} were driven by increases in the ratio of alkalinity to the dissolved inorganic carbon pool. Specifically, lower sea-levels during glacial periods (i) reduced the area of continental shelves and associated neritic carbonate deposition and (ii) induced weathering of emergent marine carbonates, both of which raised CO_3^{2-} concentrations and favored carbonate preservation at greater depths. Carbonate compensation also had a part in controlling carbonate preservation and accumulation: The transfer of CO_2 from the surface ocean to the atmosphere during glacial atmospheric pCO_2 lows increases CO_3^{2-} concentrations favoring carbonate accumulation, whereas the opposite is true during interglacial atmospheric pCO_2 highs.

A secondary influence on carbonate preservation is CO_2 accumulation in sediment pore waters and ocean bottom waters through the remineralization of organic matter. Deep waters that contain higher concentrations of CO_2, whether from higher rates of aerobic respiration and/or longer deep-water residence times, are more corrosive and result in a shallower CCD. Faster thermocline circulation and venting of deep water CO_2 to the atmosphere during glacial times would increase CO_3^{2-} concentrations, lower the CCD, and favor carbonate accumulation in deep-sea sediments. However, because of this dependence on primary productivity, as well as the vigor

and path of ocean circulation, it is important to note the relationship between the CCD and climate change is spatially heterogeneous; e.g. the CCD in the Pacific Ocean responded differently to the Last Glacial Maximum than the CCD in the Atlantic Ocean (e.g. 269). In the equatorial and NE Pacific, data over the last 45 ka show the CCD fluctuated a maximum of 1800 m, with maximum deepening associated with glacial periods and maximum shallowing associated with interglacial periods (259).

Carbonate data from Dob's Linn suggest that these mechanisms may have been operating across the Hirnantian. The data presented here show no carbonate accumulation in Katian and Rhuddanian sediments, but substantially increased carbonate accumulation (up to ~23%) during the Hirnantian glaciation. Importantly, none of the carbonate preserved in these sediments are biogenic; the disseminated carbonate indicates early authigenic formation from sediment pore waters. The fact that planktonic foraminifera and coccolithophores had not evolved and proliferated by the early Paleozoic and that the $\delta^{13}C_{carb}$ values are fairly negative further support the authigenic nature of the Hirnantian carbonates. Because the $\delta^{13}C_{carb}$ values indicate that only a fraction of the carbonate carbon was derived from respiration and the majority from seawater DIC, local processes such as anaerobic oxidation of organic matter that promote carbonate precipitation likely had limited influence. This means that during the Hirnantian, deep waters above Dob's Linn sediments were near or over-saturated with respect to the solid carbonate phase such that only minor increases in the saturation state in pore waters caused by anaerobic respiration would yield carbonate accumulation. Carbonate preservation in this section is also consistent with enhance thermocline circulation as suggested by nitrogen isotopes, as ventilation of deep water CO_2 would lessen the corrosiveness of bottom waters.

Table 5.5. **Table showing average $\delta^{15}N$ values in age and depositional bins.** Standard deviations are 1σ. Data are from this study, Luo et al., (270), Melchin et al., (239), and Laporte et al., (199). Parenthetical numbers represent number of units analyzed in each bin.

	Katian	**Hirnantian**	**Rhuddanian**
Shallow Tropics	1.1 ± 0.5‰ (3)	2.0 ± 1.0‰ (3)	1.1 ± 0.5‰ (2)
Deep Tropics	0.2 ± 0.4‰ (2)	0.6 ± 0.3‰ (2)	0.1 ± 0.3‰ (1)
Deep Subtropics	-0.4 ± 2.4‰ (1)	0.1 ± 0.8‰ (1)	-0.1 ± 0.6‰ (1)
Shallow Polar	3.0 ± 0.2‰ (2)	3.1 ± 0.4‰ (2)	N/A

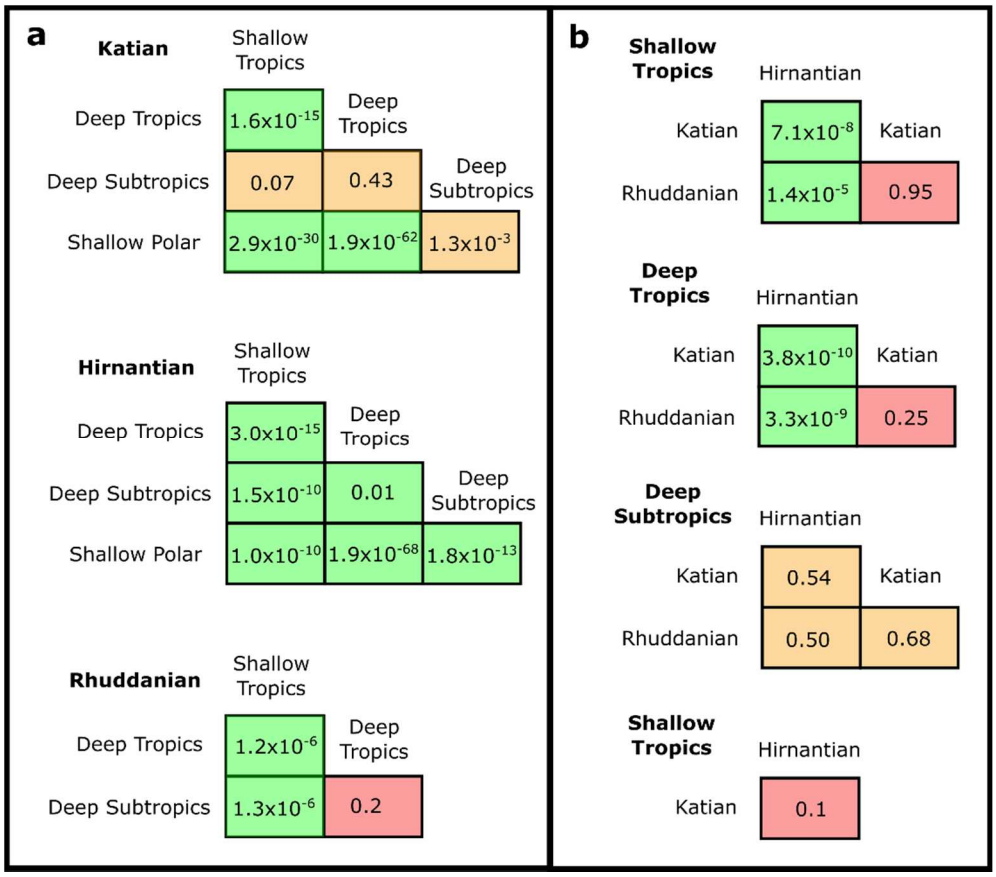

Figure 5.4**. P-value relationships comparing $\delta^{15}N$ populations between (a) depositional environments within each period, and (b) periods for each depositional environment.** Green boxes represent a statistically significant rejection of the null hypothesis that the population data from the compared parameters are equal. Red boxes represent a failure to reject the null hypothesis. Orange boxes represent a limited number of locations/samples, such that any rejection or acceptance of the null hypothesis should be questioned. All statistical tests were two-tailed T-tests with an $\alpha = 0.05$.

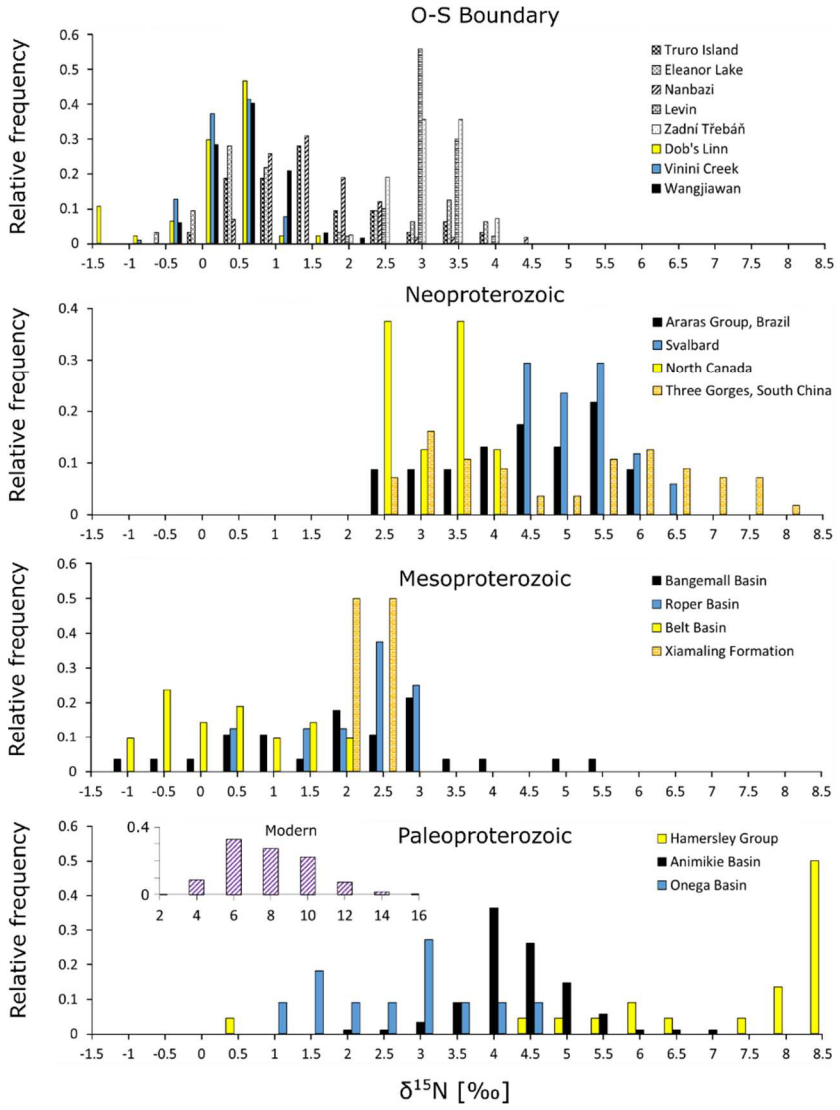

Figure 5.5**. Comparison of outer shelf and basinal $\delta^{15}N$ values between the eras of the Proterozoic and data from the O-S boundary.** The colored bars in the O-S panel are from outer shelf-basinal depositional environments. The rest of the shallower data are included in black and white for further comparison. Notice the similarities between the Mesoproterozoic and O-S nitrogen data. Figure modified from Koehler et al., (2017), and the included/excluded Proterozoic data are as in figure 6 of that reference. More recent Proterozoic nitrogen data from Canfield et al., (2018) and Zerkle et al., (2017) are also excluded due to their shallower depositional environments.

Lowering of the CCD below Dob's Linn sediments deposited in a continental slope – abyssal plain depositional environment only hints at the potential magnitude of changes to the global carbonate cycle across the Hirnantian glaciation. Carbonate records from other sections can qualitatively add to this story, but only limited interpretations can be made because there are few sections and their paleogeography's were separated. Both deep and shallow South China sections (the Wangjiawan and Nanbazi respectively) show a similar pattern of shale deposition during the Katian and Rhuddanian, and carbonaceous shale/argillaceous limestone deposition during the Hirnantian (271, 272). Deposition at the basinal to continental rise Vinini Creek (USA) section (273) is complicated by significant sediment contributions from platform carbonates and silicates. Changes in carbonate abundance at Vinini Creek, often in the form of skeletal fragments and peloids, has been attributed to the relative productivity of a "carbonate factory" on a nearby subtidal platform. There, the Katian *D. ornatus* zone contains sediments that have up to 90% carbonate by weight (199), but the subsequent Katian zones leading up to the Hirnantian (*P. pacificus* and *D. mirus*) are notably more carbonate poor, dominated by organic-rich shales with subordinate lime mudstones. Hirnantian sediments at Vinini Creek comprise lime mudstones and thickening limestone beds (199). Cessation and resumption of carbonate production has been qualitatively linked to changes in sea level, but it is possible that platform carbonate productivity and export to the Vinini Creek basin was influenced by a fluctuating CCD. The carbonate poor *P. pacificus* and *D. mirus* zones would thus represent a period of CCD shallowing where corrosive bottom waters prohibited allochthonous carbonate accumulation. The differences between deep-water carbonate deposition at Vinini Creek and deposition at Dob's Linn and the two South China sections could reflect paleo-CCD spatial heterogeneity (between the western Panthalassic, Iapetus, and paleo-Tethys Oceans), or instead the unusual periplatform depositional setting at Vinini Creek.

Other sections across the O-S seem to have never been below the CCD (e.g. 239). This finding supports the importance of deep-sea authigenic carbonate in the global carbon cycle (274, 275), particularly before the evolution of planktonic foraminifera and coccolithophores, and extends the relationship observed between deep-sea carbonate cycling and climate in the Pacific Ocean during the Quaternary back to the Ordovician.

5.6 *Conclusion*

In agreement with Luo et al., (2016), we find that the Katian is characterized by $\delta^{15}N$ values consistent with nitrogen limitation at Dob's Linn and in all other studied sections save for the two polar sections (239). This is suggestive of widespread anoxia and high rates of denitrification. The CCD in the paleo-Tethys and Iapetus oceans may have been fairly shallow at this time, potentially above the inner-shelf Nanbazi sediments and seemingly above the Wangjiawan (276) and Dob's Linn sediments. An increase in tropical $\delta^{15}N$ values (Table 5.5) and deep-sea carbonate deposition during the Hirnantian supports diminishing oxygen minimum zones and global rates of denitrification, as well as more vigorous thermocline circulation. Suppressed denitrification and N_2O production could have acted as a positive feedback for climate cooling. Distal slope and rise environments at Dob's Linn and Vinini Creek were persistent oxygen minimum zones and $\delta^{15}N$ values suggest they remained nitrogen limited due to high denitrification rates, suggesting that areas of deeper-water anoxia persisted (228). Importantly, this relationship between deep-sea carbonate deposition and climate change is an O-S example of the Quaternary Pacific-style climatically induced CCD oscillations. The nitrogen cycle and carbonate deposition landscape returned to Katian averages with the termination of the Hirnantian glaciation.

5.7 *Acknowledgements*

This study was funded by University of Washington Department of Earth and Space Sciences Harry Wheeler Scholarship and Jody Bourgeois Graduate Student Support Fund granted to MCK. We thank the U.W. Isolab and Andy Schauer for technical support, and Roger Buick for helpful discussions and comments. We also thank Sebastian Fischer and Kärt Üpraus for help in the field.

Chapter 6: CONCLUSION

Nitrogen isotopes from the geologic record are a window into how the abundance and speciation of nitrogen, oxygenation, and life co-evolved through time. This work contributes to our understanding of how biogeochemical cycles evolved on Earth and informs our understanding of how these cycles may evolve on other worlds that are fundamentally different (e.g. no plate tectonics, never accumulate surface oxygen, etc). The interactions between life and dynamic changes in these Earth systems helps provide a rough framework for how these relationships could occur on other inhabited worlds, and how they might be expressed in the atmosphere for detection. This dissertation focuses on key periods in Earth's redox and biosphere evolution to explore the timing and conditions that led to environmental and metabolic diversity. A summary of the chapters follows:

Chapter 2: Recent evidence suggests that oxygenated environments in the Mesoarchean were limited to the shallowest marine and fluvio-lacustrine settings. It is becoming increasingly clear that during the Neoarchean oxidizing conditions spread to the photic zone of deeper shelf and basinal depositional environments. Here we present nitrogen and carbon isotope ratios from the Mosquito Creek Formation of the Nullagine Group (~2.9 Ga) to further explore the Mesoarchean redox landscape. The $\delta^{15}N$ and $\delta^{13}C_{org}$ values are invariant and suggest an ecosystem dominated by nitrogen fixers (anaerobic nitrogen cycling) and CO_2 fixation by the Calvin Cycle. These data (i) support the apparent Mesoarchean trends of decreasing oxidant availability and methane cycling from onshore to offshore depositional environments, (ii) provide further evidence that the Mosquito Creek Formation was deposited in a deep marine setting, and (iii) contain $\delta^{15}N$ values that highlight the persistence of nitrogen fixation by Mo-nitrogenase and the dearth of aerobic nitrogen metabolisms in the Mesoarchean.

Chapter 3: Many paleoredox proxies indicate low-level and dynamic incipient oxygenation of Earth's surface environments during the Neoarchean (2.8-2.5 Ga) prior to the Great Oxidation Event (GOE) at ~2.4 Ga. The mode, tempo, and scale of these redox changes are poorly understood because data from various locations and ages suggest both protracted and transient oxygenation. Here we present bulk-rock and kerogen-bound nitrogen isotope ratios as well as bulk-rock selenium abundances and isotope ratios from drill-cores sampled at high stratigraphic resolution through the Jeerinah Formation (~2.66 Ga; Fortescue Group, Western Australia) to test for changes

in the redox state of the surface environment. We find that both shallow and deep depositional facies in the Jeerinah Fm display episodes of positive primary $\delta^{15}N$ values ranging from +4 to +6‰, recording aerobic nitrogen cycling that requires free O_2 in the upper water column. Moderate selenium enrichments up to 5.4 ppm in the nearer-shore core may indicate coincident oxidative weathering of sulfide minerals on land, though not to the extent seen in the younger Mt. McRae Shale that records a well-documented 'whiff' of atmospheric oxygen at 2.5 Ga. Unlike the Mt. McRae Shale, Jeerinah selenium isotopes do not show a significant excursion concurrent with the positive $\delta^{15}N$ values. Our data are thus most parsimoniously interpreted as evidence for transient surface ocean oxygenation lasting less than 50 Myr, extending over hundreds of kilometers, and occuring well before the GOE. The nitrogen isotope data clearly record nitrification and denitrification, providing the oldest firm evidence for these microbial metabolisms.

Chapter 4: Fixed nitrogen is an essential nutrient for eukaryotes. As N_2 fixation and assimilation of nitrate are catalyzed by metalloenzymes, it has been hypothesized that in Mesoproterozoic oceans nitrate was limited in offshore environments by low trace metal concentrations and high rates of denitrification in anoxic and episodically euxinic deep water masses, restricting eukaryotes to near-shore environments and limiting their evolutionary innovation. To date this hypothesis has only been tested in the Belt Supergroup (~1.4 Ga), with results that support an onshore-offshore nitrate gradient as a potential control on eukaryote ecology. Here we present bulk nitrogen and organic carbon isotopic data from non-isochronous cross-basinal facies across the Bangemall (~1.5 Ga) and the Roper (~1.4-1.5 Ga) basins to better understand the extent and variability of onshore-offshore nitrogen isotope gradients in the Mesoproterozoic. Both basins show an average ~1-2‰ enrichment in $\delta^{15}N_{bulk}$ from deep to shallow facies, with a maximum range from -1‰ offshore to +7.5‰ onshore. Unlike the Belt basin, the Bangemall and Roper basins show some offshore $\delta^{15}N_{bulk}$ values that are enriched beyond the isotopic range induced by biological N_2 fixation alone. This suggests a mixture of aerobic and anaerobic metabolisms offshore. In shallow waters, where $\delta^{15}N_{bulk}$ enrichment peaks, an aerobic nitrogen cycle was evidently operating vigorously. Even though isotopic signatures of aerobic nitrogen cycling are seen in all parts of the Bangemall and Roper basins, our data are consistent with a lateral gradient in nitrate availability within the photic zone, with higher concentrations in near-shore environments than offshore. The variability in $\delta^{15}N_{bulk}$ values in each depositional environment and the consistently low $\delta^{15}N$ values from Mesoproterozoic units compared to the

Paleoproterozoic and Neoproterozoic suggest that nitrate concentrations in the global ocean were likely low. This trend is now seen in all three Mesoproterozoic basins so far examined, and contrasts with the Paleoproterozoic and Neoproterozoic where nearly all $\delta^{15}N_{bulk}$ data plot above the N_2 fixation window. Thus, we propose that the Mesoproterozoic ocean was characterized by a nitrate minimum between the Paleo- and Neoproterozoic, with the lowest concentrations in offshore environments. This inference is consistent with a Mesoproterozoic O_2 decline following a temporary Paleoproterozoic O_2 peak, and it further supports the idea that nitrate limitation offshore may have contributed to the restriction of photosynthetic eukaryotes to near-shore environments, delaying their rise to ecological dominance until the Neoproterozoic Era.

Chapter 5: Marine ecology co-evolved with dramatic environmental change across the Ordovician-Silurian boundary. In particular, apparent trends in nitrogen cycling, both latitudinal and with respect to depositional environment, suggest extreme spatial-temporal heterogeneity in the availability of dissolved-nitrogen species associated with global climate change and mass extinction. Missing from these trends are analyses from the paleo-mid-latitudes and facies that represent the most distal continental margin. Here we present nitrogen and carbon isotope/abundance data from the O-S Global Boundary Stratotype Section and Point at Dob's Linn, Scotland. Nitrogen isotope and abundance data from bulk rock shale and bentonite samples, as well as kerogen extractions indicate that unlike in tropical shallow-water sections, the sub-tropical locale at Dob's Linn shows no changes in nitrogen cycling associated with the Hirnantian glaciation, which suggests persistent nitrogen limitation. Diminishing anoxia caused by increased ocean ventilation towards the end of the Ordovician was apparently biased towards shallow water tropical settings. If perturbations to the nitrogen cycle in part *caused* the mass extinction and changes in climate, then these results highlight the importance of the tropical inner-shelf marine biosphere in regulating the global environment. Carbonate data from this and other sections suggest a deepening of the carbonate compensation depth during the Hirnantian also consistent with increased ocean ventilation. This indicates Pacific-style responses of the CCD to glacial/interglacial periods were operational across the O-S boundary, and that an expansion of deep-sea carbonate deposition/preservation could have constituted a large reactive reservoir for surface CO_2 during these extreme changes in climate.

BIBLIOGRAPHY

1. Ohmoto H, Watanabe Y, Ikemi H, Poulson SR, Taylor BE (2006) Sulphur isotope evidence for an oxic Archaean atmosphere. *Nature* 442(7105):908–911.

2. Kaufman AJ, et al. (2007) Late Archean biospheric oxygenation and atmospheric evolution. *Science* 317(5846):1900–1903.

3. Garvin J, Buick R, Anbar AD, Arnold GL, Kaufman AJ (2009) Isotopic Evidence for an Aerobic Nitrogen Cycle in the Latest Archean. *Science* 323(5917):1045–1048.

4. Godfrey LV, Falkowski PG (2009) The cycling and redox state of nitrogen in the Archaean ocean. *Nat Geosci* 2(10):725–729.

5. Stüeken EE, Buick R, Anbar AD (2015) Selenium isotopes support free O-2 in the latest Archean. *Geology* 43(3):259–262.

6. Anbar AD, et al. (2007) A Whiff of Oxygen Before the Great Oxidation Event? *Science* 317(5846):1903–1906.

7. Duan Y, et al. (2010) Molybdenum isotope evidence for mild environmental oxygenation before the Great Oxidation Event. *Geochim Cosmochim Acta* 74(23):6655–6668.

8. Kendall B, Creaser RA, Reinhard CT, Lyons TW, Anbar AD (2015) Transient episodes of mild environmental oxygenation and oxidative continental weathering during the late Archean. *Sci Adv* 1(10):e1500777.

9. Kendall B, Brennecka GA, Weyer S, Anbar AD (2013) Uranium isotope fractionation suggests oxidative uranium mobilization at 2.50 Ga. *Chem Geol* 362:105–114.

10. Kendall B, et al. (2010) Pervasive oxygenation along late Archaean ocean margins. *Nat Geosci* 3(9):647–652.

11. Raiswell R, et al. (2011) Formation of syngenetic and early diagenetic iron minerals in the late Archean Mt. McRae Shale, Hamersley Basin, Australia: New insights on the patterns, controls and paleoenvironmental implications of authigenic mineral formation. *Geochim Cosmochim Acta* 75(4):1072–1087.

12. Eickmann B, et al. (2018) Isotopic evidence for oxygenated Mesoarchaean shallow oceans. *Nat Geosci* 11:133–138.

13. Homann M, Heubeck C, Airo A, Tice MM (2015) Morphological adaptations of 3.22 Ga-old tufted microbial mats to Archean coastal habitats (Moodies Group, Barberton Greenstone Belt, South Africa). *Precambrian Res* 266:47–64.

14. Planavsky NJ, et al. (2014) Evidence for oxygenic photosynthesis half a billion years before the Great Oxidation Event. *Nat Geosci* 7(4):283–286.

15. Riding R, Fralick P, Liang L (2014) Identification of an Archean marine oxygen oasis. *Precambrian Res* 251:232–237.

16. Crowe SA, et al. (2013) Atmospheric oxygenation three billion years ago. *Nature* 501(7468):535-+.

17. Stüeken EE, Buick R (2018) Environmental control on microbial diversification and methane production in the Mesoarchean. *Precambrian Res* 304:64–72.

18. Wille M, et al. (2013) Mo-Cr isotope evidence for a reducing Archean atmosphere in 3.46-2.76 Ga black shales from the Pilbara, Western Australia. *Chem Geol* 340:68–76.

19. Eriksson K, Krapez B, Fralick P (1994) Sedimentology of Archean Greenstone Belts - Signatures of Tectonic Evolution. *Earth-Sci Rev* 37(1–2):1–88.

20. Nijman W, Clevis Q, de Vries ST (2010) The waning stage of a greenstone belt: The Mesoarchaean Mosquito Creek Basin of the East Pilbara, Western Australia. *Precambrian Res* 180(3–4):251–271.

21. Bagas L, Bierlein FP, Bodorkos S, Nelson DR (2008) Tectonic setting, evolution and orogenic gold potential of the late Mesoarchaean Mosquito Creek Basin, North Pilbara Craton, Western Australia. *Precambrian Res* 160(3–4):227–244.

22. Kisch HJ, Nijman W (2010) Metamorphic grade and gradient from white K-micas of Na-mica bearing sedimentary rocks in the Mosquito Creek Basin, East Pilbara Craton, Western Australia. *Precambrian Res* 176(1–4):11–26.

23. Koehler MC, Stueeken EE, Kipp MA, Buick R, Knoll AH (2017) Spatial and temporal trends in Precambrian nitrogen cycling: A Mesoproterozoic offshore nitrate minimum. *Geochim Cosmochim Acta* 198:315–337.

24. Stüeken EE (2013) A test of the nitrogen-limitation hypothesis for retarded eukaryote radiation: Nitrogen isotopes across a Mesoproterozoic basinal profile. *Geochim Cosmochim Acta* 120:121–139.

25. Robl TL, Davis BH (1993) Comparison of the HF-HCl and HF-BF3 maceration techniques and the chemistry of resultant organic concentrates. *Org Geochem* 20(2):249–255.

26. Qi H, Coplen TB, Geilmann H, Brand WA, Böhlke JK (2003) Two new organic reference materials for δ13C and δ15N measurements and a new value for the δ13C of NBS 22 oil. *Rapid Commun Mass Spectrom* 17(22):2483–2487.

27. Qi H, Coplen TB, Geilmann H, Brand WA, Böhlke JK (2003) Two new organic reference materials for δ13C and δ15N measurements and a new value for the δ13C of NBS 22 oil. *Rapid Commun Mass Spectrom* 17(22):2483–2487.

28. Ader M, et al. (2016) Interpretation of the nitrogen isotopic composition of Precambrian sedimentary rocks: Assumptions and perspectives. *Chem Geol* 429:93–110.

29. Stüeken EE, Zaloumis J, Meixnerova J, Buick R (2017) Differential metamorphic effects on nitrogen isotopes in kerogen extracts and bulk rocks. *Geochim Cosmochim Acta* 217:80–94.

30. Thomazo C, Papineau D (2013) Biogeochemical Cycling of Nitrogen on the Early Earth. *Elements* 9(5):345–351.

31. Altabet MA, Francois R (1994) Sedimentary nitrogen isotopic ratio as a recorder for surface ocean nitrate utilization. *Glob Biogeochem Cycles* 8(1):103–116.

32. Lehmann MF, Bernasconi SM, Barbieri A, McKenzie JA (2002) Preservation of organic matter and alteration of its carbon and nitrogen isotope composition during simulated and in situ early sedimentary diagenesis. *Geochim Cosmochim Acta* 66(20):3573–3584.

33. Möbius J (2013) Isotope fractionation during nitrogen remineralization (ammonification): Implications for nitrogen isotope biogeochemistry. *Geochim Cosmochim Acta* 105:422–432.

34. Thunell RC, Sigman Daniel M., Muller-Karger Frank, Astor Yrene, Varela Ramon (2004) Nitrogen isotope dynamics of the Cariaco Basin, Venezuela. *Glob Biogeochem Cycles* 18(3). doi:10.1029/2003GB002185.

35. Fry B, et al. (1991) Stable Isotope Studies of the Carbon, Nitrogen and Sulfur Cycles in the Black-Sea and the Cariaco Trench. *Deep-Sea Res Part -Oceanogr Res Pap* 38:S1003–S1019.

36. Libes S, Deuser W (1988) The Isotope Geochemistry of Particulate Nitrogen in the Peru Upwelling Area and the Gulf of Maine. *Deep-Sea Res Part -Oceanogr Res Pap* 35(4):517–533.

37. Zhang X, Sigman DM, Morel FMM, Kraepiel AML (2014) Nitrogen isotope fractionation by alternative nitrogenases and past ocean anoxia. *Proc Natl Acad Sci U S A* 111(13):4782–4787.

38. Stüeken EE, Kipp MA, Koehler MC, Buick R (2016) The evolution of Earth's biogeochemical nitrogen cycle. *Earth-Sci Rev* 160:220–239.

39. Teutsong T, et al. (2017) Petrography and geochemistry of the Mesoarchean Bikoula banded iron formation in the Ntem complex (Congo craton), Southern Cameroon: Implications for its origin. *Ore Geol Rev* 80:267–288.

40. Guy BM, et al. (2012) A multiple sulfur and organic carbon isotope record from non-conglomeratic sedimentary rocks of the Mesoarchean Witwatersrand Supergroup, South Africa. *Precambrian Res* 216:208–231.

41. Stüeken EE, Buick R, Guy BM, Koehler MC (2015) Isotopic evidence for biological nitrogen fixation by molybdenum-nitrogenase from 3.2 Gyr. *Nature* 520(7549):666-U178.

42. Flannery DT, Allwood AC, Van Kranendonk MJ (2016) Lacustrine facies dependence of highly 13C-depleted organic matter during the global age of methanotrophy. *Precambrian Res* 285:216–241.

43. Izon G, et al. (2015) Multiple oscillations in Neoarchaean atmospheric chemistry. *Earth Planet Sci Lett* 431:264–273.

44. Zerkle AL, Claire MW, Domagal-Goldman SD, Farquhar J, Poulton SW (2012) A bistable organic-rich atmosphere on the Neoarchaean Earth. *Nat Geosci* 5(5):359–363.

45. Stüeken EE, et al. (2017) Environmental niches and metabolic diversity in Neoarchean lakes. *Geobiology* 15(6):767–783.

46. Lyons TW, Reinhard CT, Planavsky NJ (2014) The rise of oxygen in Earth's early ocean and atmosphere. *Nature* 506(7488):307–315.

47. Bekker A, et al. (2004) Dating the rise of atmospheric oxygen. *Nature* 427(6970):117–120.

48. Gumsley AP, et al. (2017) Timing and tempo of the Great Oxidation Event. *Proc Natl Acad Sci U S A* 114(8):1811–1816.

49. Eigenbrode JL, Freeman KH (2006) Late Archean rise of aerobic microbial ecosystems. *Proc Natl Acad Sci* 103(43):15759–15764.

50. Gregory DD, et al. (2015) The chemical conditions of the late Archean Hamersley basin inferred from whole rock and pyrite geochemistry with Delta S-33 and delta S-34 isotope analyses. *Geochim Cosmochim Acta* 149:223–250.

51. Kurzweil F, Wille M, Schoenberg R, Taubald H, Van Kranendonk MJ (2015) Continuously increasing δ98Mo values in Neoarchean black shales and iron formations from the Hamersley Basin. *Geochim Cosmochim Acta* 164:523–542.

52. Kurzweil F, et al. (2013) Atmospheric sulfur rearrangement 2.7 billion years ago: Evidence for oxygenic photosynthesis. *Earth Planet Sci Lett* 366:17–26.

53. Siebert C, Kramers JD, Meisel T, Morel P, Nagler TF (2005) PGE, Re-Os, and Mo isotope systematics in Archean and early Proterozoic sedimentary systems as proxies for redox conditions of the early Earth. *Geochim Cosmochim Acta* 69(7):1787–1801.

54. Stüeken EE, Catling DC, Buick R (2012) Contributions to late Archaean sulphur cycling by life on land. *Nat Geosci* 5(10):722–725.

55. Wille M, et al. (2007) Evidence for a gradual rise of oxygen between 2.6 and 2.5Ga from Mo isotopes and Re-PGE signatures in shales. *Geochim Cosmochim Acta* 71(10):2417–2435.

56. Bristow LA, et al. (2016) Ammonium and nitrite oxidation at nanomolar oxygen concentrations in oxygen minimum zone waters. *Proc Natl Acad Sci U S A* 113(38):10601–10606.

57. Bristow LA, et al. (2017) N-2 production rates limited by nitrite availability in the Bay of Bengal oxygen minimum zone. *Nat Geosci* 10(1):24–29.

58. Casciotti KL (2009) Inverse kinetic isotope fractionation during bacterial nitrite oxidation. *Geochim Cosmochim Acta* 73(7):2061–2076.

59. Robinson D (2001) δ15N as an integrator of the nitrogen cycle. *Trends Ecol Evol* 16(3):153–162.

60. Stüeken EE, et al. (2015) The evolution of the global selenium cycle: Secular trends in Se isotopes and abundances. *Geochim Cosmochim Acta* 162:109–125.

61. Johnson TM, Herbel MJ, Bullen TD, Zawislanski PT (1999) Selenium isotope ratios as indicators of selenium sources and oxyanion reduction. *Geochim Cosmochim Acta* 63(18):2775–2783.

62. Murphy MA, Sumner DY (2008) Tube structures of probable microbial origin in the Neoarchean Carawine Dolomite, Hamersley Basin, Western Australia. *Geobiology* 6(1):83–93.

63. Nishizawa M, et al. (2010) Grain-scale iron isotopic distribution of pyrite from Precambrian shallow marine carbonate revealed by a femtosecond laser ablation multicollector ICP-MS technique: Possible proxy for the redox state of ancient seawater. *Geochim Cosmochim Acta* 74(9):2760–2778.

64. Rasmussen B, Blake TS, Fletcher IR (2005) U-Pb zircon age constraints on the Hamersley spherule beds: Evidence for a single 2.63 Ga Jeerinah-Carawine impact ejecta layer. *Geology* 33(9):725–728.

65. French KL, et al. (2015) Reappraisal of hydrocarbon biomarkers in Archean rocks. *Proc Natl Acad Sci U S A* 112(19):5915–5920.

66. Peters CA, Piazolo S, Webb GE, Dutkiewicz A, George SC (2016) In search of early life: Carbonate veins in Archean metamorphic rocks as potential hosts of biomarkers. *Earth Planet Sci Lett* 453:44–55.

67. Lanari P, Wagner T, Vidal O (2014) A thermodynamic model for di-trioctahedral chlorite from experimental and natural data in the system MgO–FeO–Al 2 O 3–SiO 2–H 2 O: applications to P–T sections and geothermometry. *Contrib Mineral Petrol* 167(2):968.

68. Vidal O, Lanari P, Munoz M, Bourdelle F, De Andrade V (2016) Deciphering temperature, pressure and oxygen-activity conditions of chlorite formation. *Clay Miner* 51(4):615–633.

69. Large RR, et al. (2014) Trace element content of sedimentary pyrite as a new proxy for deep-time ocean-atmosphere evolution. *Earth Planet Sci Lett* 389:209–220.

70. Haendel D, Muhle K, Nitzsche H, Stiehl G, Wand U (1986) Isotopic Variations of the Fixed Nitrogen in Metamorphic Rocks. *Geochim Cosmochim Acta* 50(5):749–758.

71. Jia Y (2006) Nitrogen isotope fractionations during progressive metamorphism: A case study from the Paleozoic Cooma metasedimentary complex, southeastern Australia. *Geochim Cosmochim Acta* 70(20):5201–5214.

72. Godfrey LV, Poulton SW, Bebout GE, Fralick PW (2013) Stability of the nitrogen cycle during development of sulfidic water in the redox-stratified late Paleoproterozoic Ocean. *Geology* 41(6):655–658.

73. Teitler Y, et al. (2015) Ubiquitous occurrence of basaltic-derived paleosols in the Late Archean Fortescue Group, Western Australia. *Precambrian Res* 267:1–27.

74. Papineau D, et al. (2009) High primary productivity and nitrogen cycling after the Paleoproterozoic phosphogenic event in the Aravalli Supergroup, India. *Precambrian Res* 171(1–4):37–56.

75. Thomazo C, Ader M, Philippot P Extreme 15N-enrichments in 2.72-Gyr-old sediments: evidence for a turning point in the nitrogen cycle. *Geobiology* 9(2):107–120.

76. Sigman DM, Karsh KL, Casciotti KL (2009) Nitrogen Isotopes in the Ocean. *Encyclopedia of Ocean Sciences (Second Edition)*, ed Steele JH (Academic Press, Oxford), pp 40–54.

77. Rouxel O, Ludden J, Carignan J, Marin L, Fouquet Y (2002) Natural variations of Se isotopic composition determined by hydride generation multiple collector inductively coupled plasma mass spectrometry. *Geochim Cosmochim Acta* 66(18):3191–3199.

78. Olson SL, Kump LR, Kasting JF (2013) Quantifying the areal extent and dissolved oxygen concentrations of Archean oxygen oases. *Chem Geol* 362:35–43.

79. Lalonde SV, Konhauser KO (2015) Benthic perspective on Earth's oldest evidence for oxygenic photosynthesis. *Proc Natl Acad Sci* 112(4):995–1000.

80. Merchant SS, Helmann JD (2012) Elemental Economy: Microbial Strategies for Optimizing Growth in the Face of Nutrient Limitation. *Advances in Microbial Physiology, Vol 60*, ed Poole RK (Academic Press Ltd-Elsevier Science Ltd, London), pp 91–210.

81. Huertas MJ, López-Maury L, Giner-Lamia J, Sánchez-Riego AM, Florencio FJ (2014) Metals in Cyanobacteria: Analysis of the Copper, Nickel, Cobalt and Arsenic Homeostasis Mechanisms. *Life* 4(4):865–886.

82. Pavlov AA, Kasting JF, Eigenbrode JL, Freeman KH (2001) Organic haze in Earth's early atmosphere: Source of low-C-13 Late Archean kerogens? *Geology* 29(11):1003–1006.

83. Arney G, et al. (2016) The Pale Orange Dot: The Spectrum and Habitability of Hazy Archean Earth. *Astrobiology* 16(11):873–899.

84. Ono S, et al. (2003) New insights into Archean sulfur cycle from mass-independent sulfur isotope records from the Hamersley Basin, Australia. *Earth Planet Sci Lett* 213(1–2):15–30.

85. Scott CT, et al. (2011) Late Archean euxinic conditions before the rise of atmospheric oxygen. *Geology* 39(2):119–122.

86. Nelson DR, Trendall AF, Altermann W (1999) Chronological correlations between the Pilbara and Kaapvaal cratons. *Precambrian Res* 97(3–4):165–189.

87. Arndt N, Nelson D, Compston W, Trendall A, Thorne A (1991) The Age of the Fortescue Group, Hamersley Basin, Western-Australia, from Ion Microprobe Zircon U-Pb Results. *Aust J Earth Sci* 38(3):261–281.

88. van Kessel MAHJ, et al. (2015) Complete nitrification by a single microorganism. *Nature* 528(7583):555-+.

89. Daims H, et al. (2015) Complete nitrification by Nitrospira bacteria. *Nature* 528(7583):504-+.

90. Stüeken EE, Foriel J, Nelson BK, Buick R, Catling DC (2013) Selenium isotope analysis of organic-rich shales: advances in sample preparation and isobaric interference correction. *J Anal At Spectrom* 28(11):1734–1749.

91. WAIS Divide Project Members, et al. (2013) Onset of deglacial warming in West Antarctica driven by local orbital forcing. *Nature* 500(7463):440–444.

92. Anbar AD, Knoll AH (2002) Proterozoic ocean chemistry and evolution: A bioinorganic bridge? *Science* 297(5584):1137–1142.

93. Javaux EJ, Knoll AH, Walter MR (2001) Morphological and ecological complexity in early eukaryotic ecosystems. *Nature* 412(6842):66–69.

94. Buick R, Knoll AH (1999) Acritarchs and microfossils from the Mesoproterozoic Bangemall Group, northwestern Australia. *J Paleontol* 73(5):744–764.

95. Arnold GL, Anbar AD, Barling J, Lyons TW (2004) Molybdenum isotope evidence for widespread anoxia in mid-proterozoic oceans. *Science* 304(5667):87–90.

96. Canfield DE (1998) A new model for Proterozoic ocean chemistry. *Nature* 396(6710):450–453.

97. Planavsky NJ, et al. (2014) Low Mid-Proterozoic atmospheric oxygen levels and the delayed rise of animals. *Science* 346(6209):635–638.

98. Reinhard CT, et al. (2013) Proterozoic ocean redox and biogeochemical stasis. *Proc Natl Acad Sci U S A* 110(14):5357–5362.

99. Shen Y, Knoll AH, Walter MR (2003) Evidence for low sulphate and anoxia in a mid-Proterozoic marine basin. *Nature* 423(6940):632–635.

100. Sperling EA, et al. (2015) Statistical analysis of iron geochemical data suggests limited late Proterozoic oxygenation. *Nature* 523(7561):451–454.

101. Godfrey LV, Glass JB (2011) Chapter twenty-two - The Geochemical Record of the Ancient Nitrogen Cycle, Nitrogen Isotopes, and Metal Cofactors. *Methods in Enzymology*, Research on Nitrification and Related Processes, Part A., ed Klotz MG (Academic Press), pp 483–506.

102. Fuchsman CA, Murray JW, Konovalov SK (2008) Concentration and natural stable isotope profiles of nitrogen species in the Black Sea. *Mar Chem* 111(1–2):90–105.

103. Lindell D, Post A (1995) Ultraphytoplankton Succession Is Triggered by Deep Winter Mixing in the Gulf-of-Aqaba (eilat), Red-Sea. *Limnol Oceanogr* 40(6):1130–1141.

104. Latasa M, Bidigare RR (1998) A comparison of phytoplankton populations of the Arabian Sea during the Spring Intermonsoon and Southwest Monsoon of 1995 as described by HPLC-analyzed pigments. *Deep-Sea Res Part Ii-Top Stud Oceanogr* 45(10–11):2133–2170.

105. Karl DM, Bidigare RR, Letelier RM (2001) Long-term changes in plankton community structure and productivity in the North Pacific Subtropical Gyre: The domain shift hypothesis. *Deep-Sea Res Part Ii-Top Stud Oceanogr* 48(8–9):1449–1470.

106. Bouman HA, et al. (2011) Water-column stratification governs the community structure of subtropical marine picophytoplankton. *Environ Microbiol Rep* 3(4):473–482.

107. Fawcett SE, Lomas M, Casey JR, Ward BB, Sigman DM (2011) Assimilation of upwelled nitrate by small eukaryotes in the Sargasso Sea. *Nat Geosci* 4(10):717–722.

108. Poulin FJ, Franks PJS (2010) Size-structured planktonic ecosystems: constraints, controls and assembly instructions. *J Plankton Res* 32(8):1121–1130.

109. Farquhar J, Zerkle AL, Bekker A (2011) Geological constraints on the origin of oxygenic photosynthesis. *Photosynth Res* 107(1):11–36.

110. Czaja AD, et al. (2010) Iron and carbon isotope evidence for ecosystem and environmental diversity in the similar to 2.7 to 2.5 Ga Hamersley Province, Western Australia. *Earth Planet Sci Lett* 292(1–2):170–180.

111. Reinhard CT, Raiswell R, Scott C, Anbar AD, Lyons TW (2009) A Late Archean Sulfidic Sea Stimulated by Early Oxidative Weathering of the Continents. *Science* 326(5953):713–716.

112. Buick R (2007) Did the Proterozoic “Canfield Ocean” cause a laughing gas greenhouse? *Geobiology* 5(2):97–100.

113. Busigny V, Lebeau O, Ader M, Krapez B, Bekker A (2013) Nitrogen cycle in the Late Archean ferruginous ocean. *Chem Geol* 362:115–130.

114. Yamaguchi KE (2002) Geochemistry of Archean-Paleoproterozoic black shales: the early evolution of the atmosphere, oceans, and biosphere. *PhD Diss Pa State Univ*:485 pp.

115. Kump LR, et al. (2011) Isotopic Evidence for Massive Oxidation of Organic Matter Following the Great Oxidation Event. *Science* 334(6063):1694–1696.

116. Bekker A, Holland HD (2012) Oxygen overshoot and recovery during the early Paleoproterozoic. *Earth Planet Sci Lett* 317:295–304.

117. Planavsky NJ, Bekker A, Hofmann A, Owens JD, Lyons TW (2012) Sulfur record of rising and falling marine oxygen and sulfate levels during the Lomagundi event. *Proc Natl Acad Sci U S A* 109(45):18300–18305.

118. Hardisty DS, et al. (2014) An iodine record of Paleoproterozoic surface ocean oxygenation. *Geology* 42(7):619–622.

119. Scott C, et al. (2014) Pyrite multiple-sulfur isotope evidence for rapid expansion and contraction of the early Paleoproterozoic seawater sulfate reservoir. *Earth Planet Sci Lett* 389:95–104.

120. Frey C, Hietanen S, Juergens K, Labrenz M, Voss M (2014) N and O Isotope Fractionation in Nitrate during Chemolithoautotrophic Denitrification by Sulfurimonas gotlandica. *Environ Sci Technol* 48(22):13229–13237.

121. Brunner B, et al. (2013) Nitrogen isotope effects induced by anammox bacteria. *Proc Natl Acad Sci* 110(47):18994–18999.

122. Fulton JM, Arthur MA, Freeman KH (2012) Black Sea nitrogen cycling and the preservation of phytoplankton delta N-15 signals during the Holocene. *Glob Biogeochem Cycles* 26:GB2030.

123. Kessler AJ, et al. (2014) The isotope effect of denitrification in permeable sediments. *Geochim Cosmochim Acta* 133:156–167.

124. Sigman DM, et al. (2009) The dual isotopes of deep nitrate as a constraint on the cycle and budget of oceanic fixed nitrogen. *Deep-Sea Res Part -Oceanogr Res Pap* 56(9):1419–1439.

125. Ader M, et al. (2014) Ocean redox structure across the Late Neoproterozoic Oxygenation Event: A nitrogen isotope perspective. *Earth Planet Sci Lett* 396:1–13.

126. Saito MA, Sigman DM, Morel FMM (2003) The bioinorganic chemistry of the ancient ocean: the co-evolution of cyanobacterial metal requirements and biogeochemical cycles at the Archean-Proterozoic boundary? *Inorganica Chim Acta* 356:308–318.

127. Zerkle AL, House CH, Cox RP, Canfield DE (2006) Metal limitation of cyanobacterial N-2 fixation and implications for the Precambrian nitrogen cycle. *Geobiology* 4(4):285–297.

128. Glass JB, Axler RP, Chandra S, Goldman CR (2012) Molybdenum limitation of microbial nitrogen assimilation in aquatic ecosystems and pure cultures. *Front Microbiol* 3:331.

129. Boyle RA, et al. (2013) Nitrogen cycle feedbacks as a control on euxinia in the mid-Proterozoic ocean. *Nat Commun* 4:1533.

130. Canfield DE, Teske A (1996) Late Proterozoic rise in atmospheric oxygen concentration inferred from phylogenetic and sulphur-isotope studies. *Nature* 382(6587):127–132.

131. Thomson D, Rainbird RH, Planavsky N, Lyons TW, Bekker A (2015) Chemostratigraphy of the Shaler Supergroup, Victoria Island, NW Canada: A record of ocean composition prior to the Cryogenian glaciations. *Precambrian Res* 263:232–245.

132. Martin DM, Thorne AM (2004) Tectonic setting and basin evolution of the Bangemall Supergroup in the northwestern Capricorn Orogen. *Precambrian Res* 128(3):385–409.

133. Martin DM, Sircombe KN, Thorne AM, Cawood PA, Nemchin AA (2008) Provenance history of the Bangemall Supergroup and implications for the Mesoproterozoic paleogeography of the West Australian Craton. *Precambrian Res* 166(1):93–110.

134. Zi J-W, et al. (2015) In situ U–Pb geochronology of xenotime and monazite from the Abra polymetallic deposit in the Capricorn Orogen, Australia: Dating hydrothermal mineralization and fluid flow in a long-lived crustal structure. *Precambrian Res* 260:91–112.

135. Buick R, Des Marais DJ, Knoll AH (1995) Stable isotopic compositions of carbonates from the Mesoproterozoic Bangemall group, northwestern Australia. *Chem Geol* 123(1):153–171.

136. Martin D (2004) Peperite in the Backdoor Formation and its significance to the age and tectonic evolution of the Bangemall Supergroup, pp 53–59.

137. Wingate M (2002) *Age and palaeomagnetism of dolerite sills intruded into the Bangemall Supergroup on the Edmund 1:250 000 map sheet, Western Australia* (Geological Survey of Western Australia) Available at: http://research-repository.uwa.edu.au/en/publications/age-and-palaeomagnetism-of-dolerite-sills-intruded-into-the-bangemall-supergroup-on-the-edmund-1250-000-map-sheet-western-australia(cb47aeb7-4016-4d3e-a479-4838d657db91).html [Accessed June 13, 2018].

138. Page RW, Jackson MJ, Krassay AA (2000) Constraining sequence stratigraphy in north Australian basins: SHRIMP U–Pb zircon geochronology between Mt Isa and McArthur River*. *Aust J Earth Sci* 47(3):431–459.

139. Kendall B, Creaser RA, Gordon GW, Anbar AD (2009) Re-Os and Mo isotope systematics of black shales from the Middle Proterozoic Velkerri and Wollogorang Formations, McArthur Basin, northern Australia. *Geochim Cosmochim Acta* 73(9):2534–2558.

140. Kralik M (1982) Rb□Sb age determinations on Precambrian carbonate rocks of the Carpentarian McArthur basin, Northern Territories, Australia. *Precambrian Res* 18(1):157–170.

141. Jackson MJ, Raiswell R (1991) Sedimentology and carbon-sulphur geochemistry of the Velkerri Formation, a mid-Proterozoic potential oil source in northern Australia. *Precambrian Res* 54(1):81–108.

142. Abbott ST, Sweet IP (2000) Tectonic control on third-order sequences in a siliciclastic ramp-style basin: an example from the Roper Superbasin (Mesoproterozoic), northern Australia. *Aust J Earth Sci* 47(3):637–657.

143. Johnston DT, et al. (2008) Sulfur isotope biogeochemistry of the Proterozoic McArthur Basin. *Geochim Cosmochim Acta* 72(17):4278–4290.

144. Cox GM, et al. (2016) Basin redox and primary productivity within the Mesoproterozoic Roper Seaway. *Chem Geol* 440:101–114.

145. Jackson J-, Sweet IP, Powell TG (1988) STUDIES ON PETROLEUM GEOLOGY AND GEOCHEMISTRY, MIDDLE PROTEROZOIC, McARTHUR BASIN NORTHERN AUSTRALIA I: PETROLEUM POTENTIAL. *APPEA J* 28(1):283–302.

146. Peat CJ, Muir MD, Plumb KA, McKirdy DM, Norvick MS (1978) Proterozoic microfossils from the Roper Group, Northern Territory, Australia. 17.

147. Javaux EJ, Knoll AH, Walter MR (2004) TEM evidence for eukaryotic diversity in mid-Proterozoic oceans. *Geobiology* 2(3):121–132.

148. Summons RE, Powell TG, Boreham CJ (1988) Petroleum geology and geochemistry of the Middle Proterozoic McArthur Basin, Northern Australia: III. Composition of extractable hydrocarbons. *Geochim Cosmochim Acta* 52(7):1747–1763.

149. Dutkiewicz A, Volk H, Ridley J, George S (2003) Biomarkers, brines, and oil in the Mesoproterozoic, Roper Superbasin, Australia. *Geology* 31(11):981.

150. Dutkiewicz A, Volk H, Ridley J, George SC (2004) Geochemistry of oil in fluid inclusions in a middle Proterozoic igneous intrusion: implications for the source of hydrocarbons in crystalline rocks. *Org Geochem* 35(8):937–957.

151. Volk H, George SC, Dutkiewicz A, Ridley J (2005) Characterisation of fluid inclusion oil in a Mid-Proterozoic sandstone and dolerite (Roper Superbasin, Australia). *Chem Geol* 223(1):109–135.

152. Siljeström S, et al. (2013) Analysis of single oil-bearing fluid inclusions in mid-Proterozoic sandstones (Roper Group, Australia). *Geochim Cosmochim Acta* 122:448–463.

153. Flannery EN, George SC (2014) Assessing the syngeneity and indigeneity of hydrocarbons in the ~1.4Ga Velkerri Formation, McArthur Basin, using slice experiments. *Org Geochem* 77:115–125.

154. Donnelly TH, Crick IH (1988) Depositional environment of the middle proterozoic velkerri formation in Northern Australia: Geochemical evidence. *Precambrian Res* 42(1):165–172.

155. Freudenthal T, Wagner T, Wenzhöfer F, Zabel M, Wefer G (2001) Early diagenesis of organic matter from sediments of the eastern subtropical Atlantic: evidence from stable nitrogen and carbon isotopes. *Geochim Cosmochim Acta* 65(11):1795–1808.

156. Macko SA, Estep MLF (1984) Microbial alteration of stable nitrogen and carbon isotopic compositions of organic matter. *Org Geochem* 6:787–790.

157. Robinson RS, et al. (2012) A review of nitrogen isotopic alteration in marine sediments. *Paleoceanography* 27(4). doi:10.1029/2012PA002321.

158. Guo H, et al. (2013) Isotopic composition of organic and inorganic carbon from the Mesoproterozoic Jixian Group, North China: Implications for biological and oceanic evolution. *Precambrian Res* 224:169–183.

159. Macko SA, Fogel ML, Hare PE, Hoering TC (1987) Isotopic fractionation of nitrogen and carbon in the synthesis of amino acids by microorganisms. *Chem Geol Isot Geosci Sect* 65(1):79–92.

160. Freude C, Blaser M (2016) Carbon Isotope Fractionation during Catabolism and Anabolism in Acetogenic Bacteria Growing on Different Substrates. *Appl Environ Microbiol* 82(9):2728–2737.

161. Bekker A, et al. (2008) Fractionation between inorganic and organic carbon during the Lomagundi (2.22–2.1 Ga) carbon isotope excursion. *Earth Planet Sci Lett* 271(1):278–291.

162. Rivera KT, Puckette J, Quan TM (2015) Evaluation of redox versus thermal maturity controls on δ15N in organic rich shales: A case study of the Woodford Shale, Anadarko Basin, Oklahoma, USA. *Org Geochem* 83–84:127–139.

163. Bebout GE, Fogel ML (1992) Nitrogen-isotope compositions of metasedimentary rocks in the Catalina Schist, California: Implications for metamorphic devolatilization history. *Geochim Cosmochim Acta* 56(7):2839–2849.

164. Schidlowski M (1987) Application of Stable Carbon Isotopes to Early Biochemical Evolution on Earth. *Annu Rev Earth Planet Sci* 15(1):47–72.

165. Hayes J, W. Wedeking K, R. Kaplan I (1983) Precambrian organic geochemistry - Preservation of the record.

166. Hoefs J, Frey M (1976) The isotopic composition of carbonaceous matter in a metamorphic profile from the Swiss Alps. *Geochim Cosmochim Acta* 40(8):945–951.

167. McKirdy DM, Powell TG (1974) Metamorphic Alteration of Carbon Isotopic Composition in Ancient Sedimentary Organic Matter: New Evidence from Australia and South Africa. *Geology* 2(12):591.

168. Bartley JK, Kah LC (2004) Marine carbon reservoir, Corg-Ccarb coupling, and the evolution of the Proterozoic carbon cycle. *Geology* 32(2):129–132.

169. Gilleaudeau GJ, Kah LC (2013) Carbon isotope records in a Mesoproterozoic epicratonic sea: Carbon cycling in a low-oxygen world. *Precambrian Res* 228:85–101.

170. Hayes JM (2001) Fractionation of Carbon and Hydrogen Isotopes in Biosynthetic Processes. *Rev Mineral Geochem* 43(1):225–277.

171. Luo G, Hallmann C, Xie S, Ruan X, Summons RE (2015) Comparative microbial diversity and redox environments of black shale and stromatolite facies in the Mesoproterozoic Xiamaling Formation. *Geochim Cosmochim Acta* 151:150–167.

172. Nishizawa M, Miyazaki J, Makabe A, Koba K, Takai K (2014) Physiological and isotopic characteristics of nitrogen fixation by hyperthermophilic methanogens: Key insights into nitrogen anabolism of the microbial communities in Archean hydrothermal systems. *Geochim Cosmochim Acta* 138:117–135.

173. Zerkle AL, Junium CK, Canfield DE, House CH (2008) Production of 15N-depleted biomass during cyanobacterial N2-fixation at high Fe concentrations. *J Geophys Res Biogeosciences* 113(G3). doi:10.1029/2007JG000651.

174. Quan TM, Falkowski PG (2009) Redox control of N:P ratios in aquatic ecosystems. *Geobiology* 7(2):124–139.

175. Planavsky NJ, et al. (2011) Widespread iron-rich conditions in the mid-Proterozoic ocean. *Nature* 477(7365):448–451.

176. Poulton SW, Canfield DE (2011) Ferruginous Conditions: A Dominant Feature of the Ocean through Earth's History. *Elements* 7(2):107–112.

177. Morales LV, et al. (2014) Elevated 15N/14N in particulate organic matter, zooplankton, and diatom frustule-bound nitrogen in the ice-covered water column of the Bering Sea eastern shelf. *Deep Sea Res Part II Top Stud Oceanogr* 109:100–111.

178. Granger J, et al. (2011) Coupled nitrification-denitrification in sediment of the eastern Bering Sea shelf leads to 15N enrichment of fixed N in shelf waters. *J Geophys Res Oceans* 116(C11). doi:10.1029/2010JC006751.

179. Tesdal J-E, Galbraith ED, Kienast M (2013) Nitrogen isotopes in bulk marine sediment: linking seafloor observations with subseafloor records. *Biogeosciences* 10(1):101–118.

180. Haug GH, et al. (1998) Glacial/interglacial variations in production and nitrogen fixation in the Cariaco Basin during the last 580 kyr. *Paleoceanography* 13(5):427–432.

181. Tyrrell T (1999) The relative influences of nitrogen and phosphorus on oceanic primary production. *Nature* 400(6744):525–531.

182. Thamdrup B (2012) New Pathways and Processes in the Global Nitrogen Cycle. *Annu Rev Ecol Evol Syst* 43(1):407–428.

183. Martens-Habbena W, Berube PM, Urakawa H, de la Torre JR, Stahl DA (2009) Ammonia oxidation kinetics determine niche separation of nitrifying Archaea and Bacteria. *Nature* 461(7266):976–979.

184. Füssel J, et al. (2012) Nitrite oxidation in the Namibian oxygen minimum zone. *ISME J* 6(6):1200–1209.

185. Sigman DM, Altabet MA, McCorkle DC, Francois R, Fischer G (2000) The δ15N of nitrate in the Southern Ocean: Nitrogen cycling and circulation in the ocean interior. *J Geophys Res Oceans* 105(C8):19599–19614.

186. Galbraith ED, et al. (2013) The acceleration of oceanic denitrification during deglacial warming. *Nat Geosci* 6(7):579–584.

187. Algeo TJ, Meyers PA, Robinson RS, Rowe H, Jiang GQ (2014) Icehouse–greenhouse variations in marine denitrification. *Biogeosciences* 11(4):1273–1295.

188. Kah LC, Lyons TW, Frank TD (2004) Low marine sulphate and protracted oxygenation of the Proterozoic biosphere. *Nature* 431(7010):834–838.

189. Kikumoto R, et al. (2014) Nitrogen isotope chemostratigraphy of the Ediacaran and Early Cambrian platform sequence at Three Gorges, South China. *Gondwana Res* 25(3):1057–1069.

190. Papineau D, Purohit R, Fogel ML, Shields-Zhou GA (2013) High phosphate availability as a possible cause for massive cyanobacterial production of oxygen in the Paleoproterozoic atmosphere. *Earth Planet Sci Lett* 362:225–236.

191. Rooze J, Meile C (2016) The effect of redox conditions and bioirrigation on nitrogen isotope fractionation in marine sediments. *Geochim Cosmochim Acta* 184:227–239.

192. Lydon J (2007) Geology and metallogeny of the Belt-Purcell Basin. *Geol Assoc Can Miner Depos Div* 5:581–607.

193. Winston D (1990) Evidence for intracratonic, fluvial and lacustrine settings of Middle to Late Proterozoic basins of western USA. *-Proterozoic Laurentia-Balt Geol Assoc Can Spec Pap* 38:535–564.

194. Luepke JJ, Lyons TW (2001) Pre-Rodinian (Mesoproterozoic) supercontinental rifting along the western margin of Laurentia: geochemical evidence from the Belt-Purcell Supergroup. *Precambrian Res* 111(1):79–90.

195. Pratt BR (2001) Oceanography, bathymetry and syndepositional tectonics of a Precambrian intracratonic basin: integrating sediments, storms, earthquakes and tsunamis in the Belt Supergroup (Helena Formation, ca. 1.45Ga), western North America. *Sediment Geol* 141–142:371–394.

196. Pavlov AA, Kasting JF (2002) Mass-independent fractionation of sulfur isotopes in Archean sediments: strong evidence for an anoxic Archean atmosphere. *Astrobiology* 2(1):27–41.

197. Cremonese L, Shields-Zhou GA, Struck U, Ling H-F, Och LM (2014) Nitrogen and organic carbon isotope stratigraphy of the Yangtze Platform during the Ediacaran–Cambrian transition in South China. *Palaeogeogr Palaeoclimatol Palaeoecol* 398:165–186.

198. Junium CK, Arthur MA (2007) Nitrogen cycling during the Cretaceous, Cenomanian-Turonian Oceanic Anoxic Event II. *Geochem Geophys Geosystems* 8(3). doi:10.1029/2006GC001328.

199. LaPorte DF, et al. (2009) Local and global perspectives on carbon and nitrogen cycling during the Hirnantian glaciation. *Palaeogeogr Palaeoclimatol Palaeoecol* 276(1–4):182–195.

200. Ohkouchi N, Kashiyama Y, Kuroda J, Ogawa NO, Kitazato H (2006) The importance of diazotrophic cyanobacteria as primary producers during Cretaceous Oceanic Anoxic Event 2. *Biogeosciences* 3(4):467–478.

201. Rau GH, Arthur MA, Dean WE (1987) 15N/14N variations in Cretaceous Atlantic sedimentary sequences: implication for past changes in marine nitrogen biogeochemistry. *Earth Planet Sci Lett* 82(3):269–279.

202. Schoepfer SD, Henderson CM, Garrison GH, Ward PD (2012) Cessation of a productive coastal upwelling system in the Panthalassic Ocean at the Permian–Triassic Boundary. *Palaeogeogr Palaeoclimatol Palaeoecol* 313–314:181–188.

203. Sephton MA, et al. (2002) Carbon and nitrogen isotope disturbances and an end-Norian (Late Triassic) extinction event. *Geology* 30(12):1119–1122.

204. Wang X, Shi X, Tang D, Zhang W (2013) Nitrogen Isotope Evidence for Redox Variations at the Ediacaran-Cambrian Transition in South China. *J Geol* 121(5):489–502.

205. Idnurm M, Giddings JW, Plumb KA (1995) Apparent polar wander and reversal stratigraphy of the Palaeo-Mesoproterozoic southeastern McArthur Basin, Australia. *Precambrian Res* 72(1):1–41.

206. Elston DP, Enkin RJ, Baker J, Kisilevsky DK (2002) Tightening the Belt: Paleomagnetic-stratigraphic constraints on deposition, correlation, and deformation of the Middle Proterozoic (ca. 1.4 Ga) Belt-Purcell Supergroup, United States and Canada. *GSA Bull* 114(5):619–638.

207. Symons DTA (1966) A paleomagnetic study on the Gunflint, Mesabi, and Cuyuna iron ranges in the Lake Superior region. *Econ Geol* 61(8):1336–1361.

208. Canfield DE, et al. (2013) Oxygen dynamics in the aftermath of the Great Oxidation of Earth's atmosphere. *Proc Natl Acad Sci* 110(42):16736–16741.

209. Partin CA, et al. (2013) Uranium in iron formations and the rise of atmospheric oxygen. *Chem Geol* 362:82–90.

210. Zhang S, et al. (2016) Sufficient oxygen for animal respiration 1,400 million years ago. *Proc Natl Acad Sci* 113(7):1731–1736.

211. Blamey NJF, et al. (2016) Paradigm shift in determining Neoproterozoic atmospheric oxygen. *Geology* 44(8):651–654.

212. Luo G, et al. (2015) Decline in oceanic sulfate levels during the early Mesoproterozoic. *Precambrian Res* 258:36–47.

213. G. Brookins D (1988) Eh-pH Diagrams for Geochemistry, pp 66–67.

214. Blumenberg M, Thiel V, Riegel W, Kah LC, Reitner J (2012) Biomarkers of black shales formed by microbial mats, Late Mesoproterozoic (1.1Ga) Taoudeni Basin, Mauritania. *Precambrian Res* 196–197:113–127.

215. Guo H, et al. (2015) Sulfur isotope composition of carbonate-associated sulfate from the Mesoproterozoic Jixian Group, North China: Implications for the marine sulfur cycle. *Precambrian Res* 266:319–336.

216. Malone TC (1980) Size-Fractionated Primary Productivity of Marine Phytoplankton. *Primary Productivity in the Sea*, Environmental Science Research. (Springer, Boston, MA), pp 301–319.

217. Li WKW, Dickie PM, Irwin BD, Wood AM (1992) Biomass of bacteria, cyanobacteria, prochlorophytes and photosynthetic eukaryotes in the Sargasso Sea. *Deep Sea Res Part Oceanogr Res Pap* 39(3):501–519.

218. Johnston DT, Wolfe-Simon F, Pearson A, Knoll AH (2009) Anoxygenic photosynthesis modulated Proterozoic oxygen and sustained Earth's middle age. *Proc Natl Acad Sci* 106(40):16925–16929.

219. Montes E, et al. (2013) Sources of δ15N variability in sinking particulate nitrogen in the Cariaco Basin, Venezuela. *Deep Sea Res Part II Top Stud Oceanogr* 93:96–107.

220. Glass JB, Wolfe-Simon F, Anbar AD (2009) Coevolution of metal availability and nitrogen assimilation in cyanobacteria and algae. *Geobiology* 7(2):100–123.

221. Nardin E, et al. (2011) Modeling the early Paleozoic long-term climatic trend. *GSA Bull* 123(5–6):1181–1192.

222. Kah LC, Thompson CK, Henderson MA, Zhan R (2016) Behavior of marine sulfur in the Ordovician. *Palaeogeogr Palaeoclimatol Palaeoecol* 458:133–153.

223. Marenco PJ, Martin KR, Marenco KN, Barber DC (2016) Increasing global ocean oxygenation and the Ordovician Radiation: Insights from Th/U of carbonates from the Ordovician of western Utah. *Palaeogeogr Palaeoclimatol Palaeoecol* 458:77–84.

224. Gibbs MT, Barron EJ, Kump LR (1997) An atmospheric pCO2 threshold for glaciation in the Late Ordovician. *Geology* 25(5):447.

225. Herrmann AD, Patzkowsky ME, Pollard D (2004) The impact of paleogeography, pCO2, poleward ocean heat transport and sea level change on global cooling during the Late Ordovician. *Palaeogeogr Palaeoclimatol Palaeoecol* 206(1):59–74.

226. Finnegan S, et al. (2011) The Magnitude and Duration of Late Ordovician-Early Silurian Glaciation. *Science* 331(6019):903–906.

227. Jablonski D (1991) Extinctions: A Paleontological Perspective. *Science* 253(5021):754–757.

228. Bartlett R, et al. (2018) Abrupt global-ocean anoxia during the Late Ordovician–early Silurian detected using uranium isotopes of marine carbonates. *Proc Natl Acad Sci*:201802438.

229. Erlykin AD, Harper DAT, Sloan T, Wolfendale AW (2017) Mass extinctions over the last 500 myr: an astronomical cause? *Palaeontology* 60(2):159–167.

230. Rampino MR, Caldeira K (2018) Comparison of the ages of large-body impacts, flood-basalt eruptions, ocean-anoxic events and extinctions over the last 260 million years: a statistical study. *Int J Earth Sci* 107(2):601–606.

231. Ernst RE, Youbi N (2017) How Large Igneous Provinces affect global climate, sometimes cause mass extinctions, and represent natural markers in the geological record. *Palaeogeogr Palaeoclimatol Palaeoecol* 478:30–52.

232. Gong Q, et al. (2017) Mercury spikes suggest volcanic driver of the Ordovician-Silurian mass extinction. *Sci Rep* 7(1):5304.

233. Harper DA, Hammarlund EU, Rasmussen CM (2014) End Ordovician extinctions: a coincidence of causes. *Gondwana Res* 25(4):1294–1307.

234. Retallack GJ (2015) Late Ordovician Glaciation Initiated by Early Land Plant Evolution and Punctuated by Greenhouse Mass Extinctions. *J Geol* 123(6):509–538.

235. Bergström SM, Chen X, Gutiérrez-Marco JC, Dronov A (2009) The new chronostratigraphic classification of the Ordovician System and its relations to major regional series and stages and to δ13C chemostratigraphy. *Lethaia* 42(1):97–107.

236. Hammarlund EU, et al. (2012) A sulfidic driver for the end-Ordovician mass extinction. *Earth Planet Sci Lett* 331–332:128–139.

237. Luo G, et al. (2016) Perturbation of the marine nitrogen cycle during the Late Ordovician glaciation and mass extinction. *Palaeogeogr Palaeoclimatol Palaeoecol* 448:339–348.

238. Cooper RA, Rigby S, Loydell DK, Bates DEB (2012) Palaeoecology of the Graptoloidea. *Earth-Sci Rev* 112(1):23–41.

239. Melchin MJ, Mitchell CE, Holmden C, Štorch P (2013) Environmental changes in the Late Ordovician–early Silurian: Review and new insights from black shales and nitrogen isotopes. *GSA Bull* 125(11–12):1635–1670.

240. Rohrssen M, Love GD, Fischer W, Finnegan S, Fike DA (2013) Lipid biomarkers record fundamental changes in the microbial community structure of tropical seas during the Late Ordovician Hirnantian glaciation. *Geology* 41(2):127–130.

241. Armstrong HA, Coe AL (1997) Deep-sea sediments record the geophysiology of the late Ordovician glaciation. *J Geol Soc* 154(6):929–934.

242. Oliver GJH, Leggett JK (1980) Metamorphism in an accretionary prism: prehnite-pumpellyite facies metamorphism of the Southern Uplands of Scotland. *Earth Environ Sci Trans R Soc Edinb* 71(4):235–246.

243. Kiipli T, Dahlqvist P, Kallaste T, Kiipli E, NõLvak J (2015) Upper Katian (Ordovician) bentonites in the East Baltic, Scandinavia and Scotland: geochemical correlation and volcanic source interpretation. *Geol Mag* 152(04):589–602.

244. Armstrong HA, Owen AW (2002) Euconodont paleobiogeography and the closure of the Iapetus Ocean. *Geology* 30(12):1091–1094.

245. Cocks LRM, Torsvik TH (2002) Earth geography from 500 to 400 million years ago: a faunal and palaeomagnetic review. *J Geol Soc* 159(6):631–644.

246. Kim S-T, Mucci A, Taylor BE (2007) Phosphoric acid fractionation factors for calcite and aragonite between 25 and 75 °C: Revisited. *Chem Geol* 246(3–4):135–146.

247. Fernandez A, van Dijk J, A. Müller I, M. Bernasconi S (2016) Siderite acid fractionation factors for sealed and open vessel digestions at 70 °C and 100 °C. *Chem Geol* 444. doi:10.1016/j.chemgeo.2016.10.015.

248. Finlay AJ, Selby D, Gröcke DR (2010) Tracking the Hirnantian glaciation using Os isotopes. *Earth Planet Sci Lett* 293(3–4):339–348.

249. Underwood CJ, Crowley SF, Marshall JD, Brenchley PJ (1997) High-Resolution carbon isotope stratigraphy of the basal Silurian Stratotype (Dob's Linn, Scotland) and its global correlation. *J Geol Soc* 154(4):709–718.

250. Boudreau BP, Canfield DE (1988) A provisional diagenetic model for pH in anoxic porewaters: Application to the FOAM Site. doi:info:doi/10.1357/002224088785113603.

251. Rosenfeld JK (1979) Ammonium adsorption in nearshore anoxic sediments. *Limnol Oceanogr* 24(2):356–364.

252. Stueken EE, Kipp MA, Koehler MC, Buick R (2016) The evolution of Earth's biogeochemical nitrogen cycle. *Earth-Sci Rev* 160:220–239.

253. Galbraith ED, Kienast M, Pedersen TF, Calvert SE (2004) Glacial-interglacial modulation of the marine nitrogen cycle by high-latitude O2 supply to the global thermocline. *Paleoceanography* 19(4). doi:10.1029/2003PA001000.

254. Berner RA, Beerling DJ, Dudley R, Robinson JM, Wildman RA (2003) Phanerozoic Atmospheric Oxygen. *Annu Rev Earth Planet Sci* 31(1):105–134.

255. Arrhenius G (1953) Sediment Cores from the East Pacific. *Geol Fören Stockh Förh* 75(1):115–118.

256. Hays JD, Saito T, Opdyke ND, Burckle LH (1969) Pliocene-Pleistocene Sediments of the Equatorial Pacific: Their Paleomagnetic, Biostratigraphic, and Climatic Record. *GSA Bull* 80(8):1481–1514.

257. Shackleton NJ, Opdyke ND (1977) Oxygen isotope and palaeomagnetic evidence for early Northern Hemisphere glaciation. *Nature* 270(5634):216–219.

258. Shackleton NJ, Opdyke ND (1976) Oxygen-Isotope and Paleomagnetic Stratigraphy of Pacific Core V28-239 Late Pliocene to Latest Pleistocene. *EPIC3Bremerhaven GSA*. Available at: http://epic.awi.de/35544/ [Accessed May 16, 2018].

259. Karlin R, Lyle M, Zahn R (1992) Carbonate Variations in the Northeast Pacific during the Late Quaternary. *Paleoceanography* 7(1):43–61.

260. Lee GH, Park SC, Kim DC (2000) Fluctuations of the calcite compensation depth (CCD) in the East Sea (Sea of Japan). *Geo-Mar Lett* 20(1):20–26.

261. Broecker WS, Clark E (2001) Glacial-to-Holocene Redistribution of Carbonate Ion in the Deep Sea. *Science* 294(5549):2152–2155.

262. Lalicata JJ, Lea DW (2011) Pleistocene carbonate dissolution fluctuations in the eastern equatorial Pacific on glacial timescales: Evidence from ODP Hole 1241. *Mar Micropaleontol* 79(1):41–51.

263. Wang N, Huang B-Q, Li H (2016) Deep-water carbonate dissolution in the northern South China Sea during Marine Isotope Stage 3. *J Palaeogeogr* 5(1):100–107.

264. Sun H, et al. (2017) Deep-sea carbonate preservation in the western Philippine Sea over the past 1Ma. *Quat Int* 459:101–115.

265. Anderson RF, Fleisher MQ, Lao Y, Winckler G (2008) Modern CaCO3 preservation in equatorial Pacific sediments in the context of late-Pleistocene glacial cycles. *Mar Chem* 111(1):30–46.

266. Yu J, et al. (2010) Loss of Carbon from the Deep Sea Since the Last Glacial Maximum. *Science* 330(6007):1084–1087.

267. Yu J, et al. (2013) Responses of the deep ocean carbonate system to carbon reorganization during the Last Glacial–interglacial cycle. *Quat Sci Rev* 76:39–52.

268. Kerr J, Rickaby R, Yu J, Elderfield H, Sadekov AY (2017) The effect of ocean alkalinity and carbon transfer on deep-sea carbonate ion concentration during the past five glacial cycles. *Earth Planet Sci Lett* 471:42–53.

269. Crowley TJ (1985) Late Quaternary Carbonate Changes in the North Atlantic and Atlantic/Pacific Comparisons. *Geophysical Monograph Series*, eds Sundquist ET, Broecker WS (American Geophysical Union, Washington, D. C.), pp 271–284.

270. Luo G, et al. (2016) Perturbation of the marine nitrogen cycle during the Late Ordovician glaciation and mass extinction. *Palaeogeogr Palaeoclimatol Palaeoecol* 448:339–348.

271. Chen X, et al. (1999) Stratigraphy of the Hirnantian substage from Wangjiawan, Yichang, W. Hubei and Honghuayuan, Tongzi, N. Guizhou, China. *Acta Univ Carol Geol* (43):233–236.

272. Yan D, Chen D, Wang Q, Wang J, Wang Z (2009) Carbon and sulfur isotopic anomalies across the Ordovician–Silurian boundary on the Yangtze Platform, South China. *Palaeogeogr Palaeoclimatol Palaeoecol* 274(1):32–39.

273. Finney S, Berry William B. N., Cooper John D. (2007) The influence of denitrifying seawater on graptolite extinction and diversification during the Hirnantian (latest Ordovician) mass extinction event. *Lethaia* 40(3):281–291.

274. Schrag DP, Higgins JA, Macdonald FA, Johnston DT (2013) Authigenic Carbonate and the History of the Global Carbon Cycle. *Science* 339(6119):540–543.

275. Sun X, Turchyn AV (2014) Significant contribution of authigenic carbonate to marine carbon burial. *Nat Geosci* 7(3):201–204.

276. Gorjan P, Kaiho K, Fike D, Xu C (2012) Carbon- and sulfur-isotope geochemistry of the Hirnantian (Late Ordovician) Wangjiawan (Riverside) section, South China: Global correlation and environmental event interpretation. *Palaeogeogr Palaeoclimatol Palaeoecol* s 337–338:14–22.

277. Mitchell K, et al. (2012) Selenium as paleo-oceanographic proxy: A first assessment. *Geochim Cosmochim Acta* 89:302–317.

278. Cole DB, Zhang S, Planavsky NJ (2017) A new estimate of detrital redox-sensitive metal concentrations and variability in fluxes to marine sediments. *Geochim Cosmochim Acta* 215:337–353.

279. Stüeken EE (2017) Selenium Isotopes as a Biogeochemical Proxy in Deep Time. *Non-Traditional Stable Isotopes*, eds Teng FZ, Watkins J, Dauphas N (Mineralogical Soc Amer & Geochemical Soc, Chantilly), pp 657–682.

280. Taylor S, Mclennan S (1995) The Geochemical Evolution of the Continental-Crust. *Rev Geophys* 33(2):241–265.

281. Li YH, Schoonmaker JE (2003) *Chemical composition and mineralogy of marine sediments* (na).

282. Rudnick RL, Gao S (2014) 4.1 - Composition of the Continental Crust. *Treatise on Geochemistry (Second Edition)*, eds Holland HD, Turekian KK (Elsevier, Oxford), pp 1–51.

283. Smith R, Perdrix J, Parks T (1982) Burial Metamorphism in the Hamersley Basin, Western Australia. *J Petrol* 23(1):75–102.

284. White AJR, Legras M, Smith RE, Nadoll P (2014) Deformation-driven, regional-scale metasomatism in the Hamersley Basin, Western Australia. *J Metamorph Geol* 32(4):417–433.

285. White AJR, Smith RE, Nadoll P, Legras M (2014) Regional-scale Metasomatism in the Fortescue Group Volcanics, Hamersley Basin, Western Australia: Implications for Hydrothermal Ore Systems. *J Petrol* 55(5):977–1009.

286. Frey M, Robinson D (2009) *Low-grade metamorphism* (John Wiley & Sons).

287. Zerkle AL, et al. (2017) Onset of the aerobic nitrogen cycle during the Great Oxidation Event. *Nature* 542(7642):465.

Appendix

7.1 *Chapter 2*

Supplementary figures and tables for "Nitrogen isotope evidence for anoxic deep marine environments from the Mesoarchean Mosquito Creek Formation, Australia"

Authors:
Matthew C. Koehler, Roger Buick & Mark E. Barley

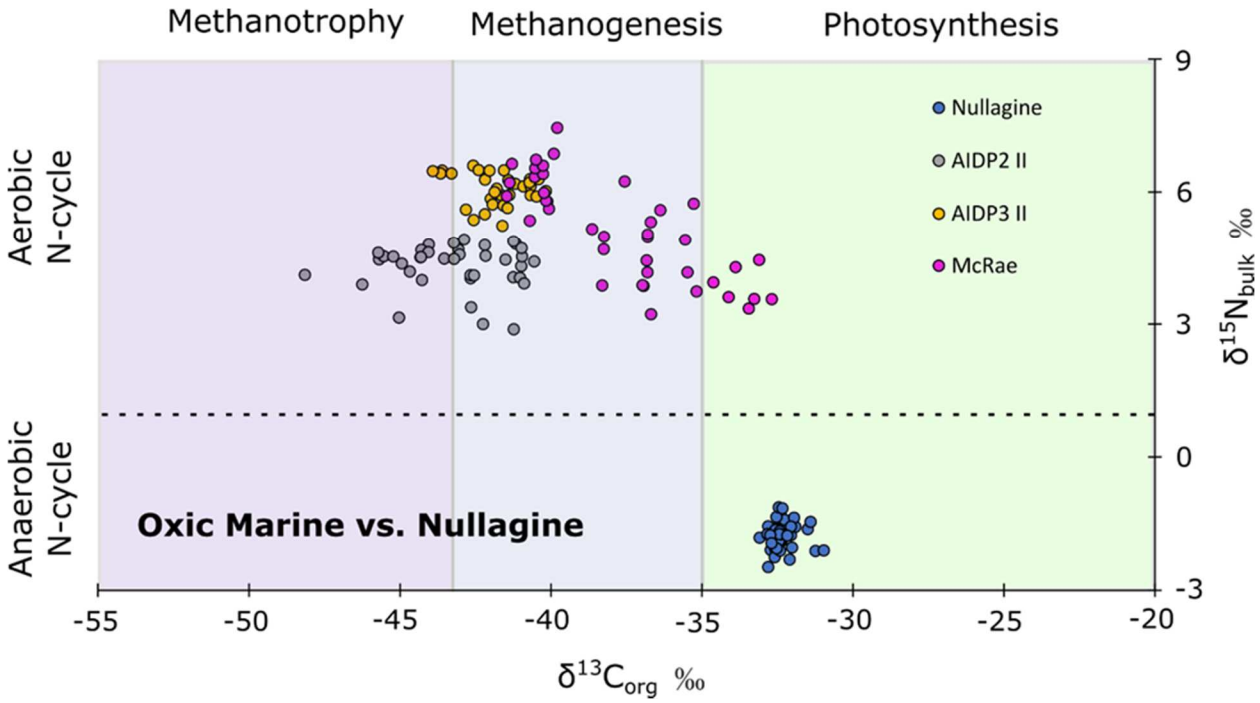

Figure 0.1**. Cross-plots of $\delta^{13}C_{org}$ vs. $\delta^{15}N_{bulk}$ comparing sections with known oxygenation events to the data from this study**. AIDP labels refer to data from the Jeerinah Formation (Koehler et al., in review). McRae labels refer to data from the Mt. McRae Shale (Garvin et al., 2009).

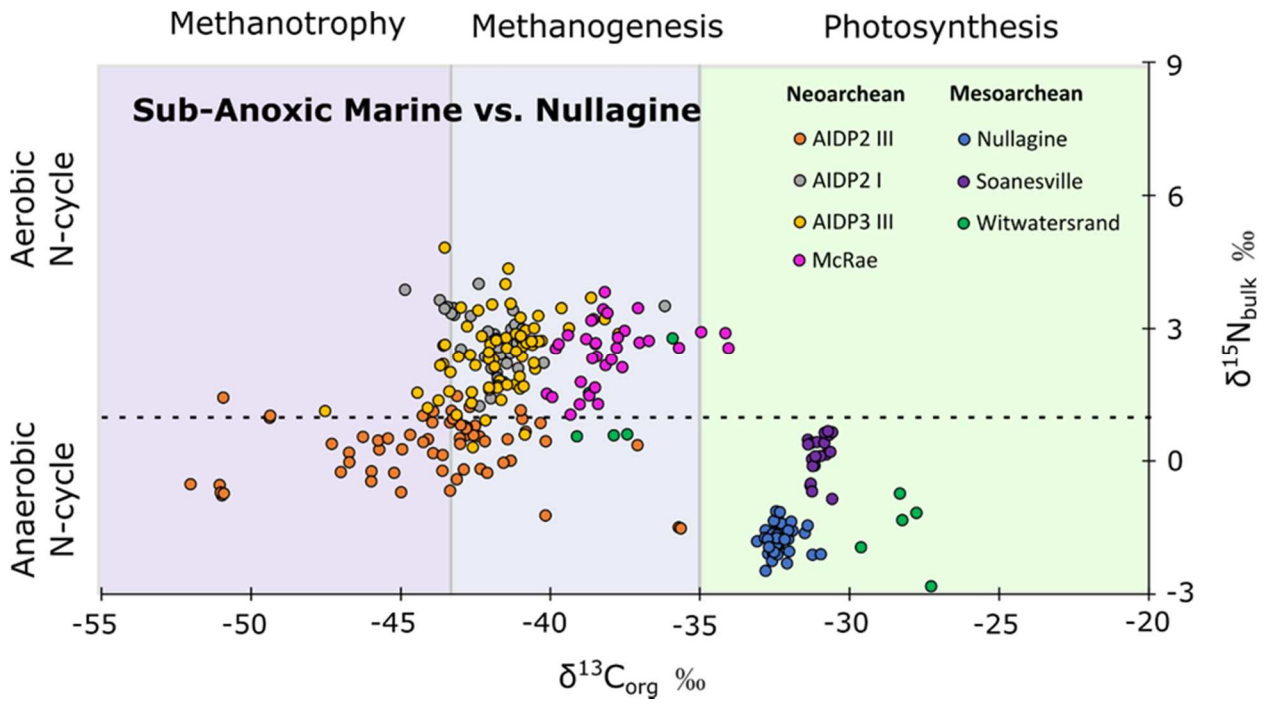

Figure 0.2**. Cross-plots of $\delta^{13}C_{org}$ vs. $\delta^{15}N_{bulk}$ comparing sub-anoxic marine section to the data from this study**. AIDP and McRae labels are as in **Error! Reference source not found.**. oanesville and Witwatersrand data are from Stüeken et al., (2015).

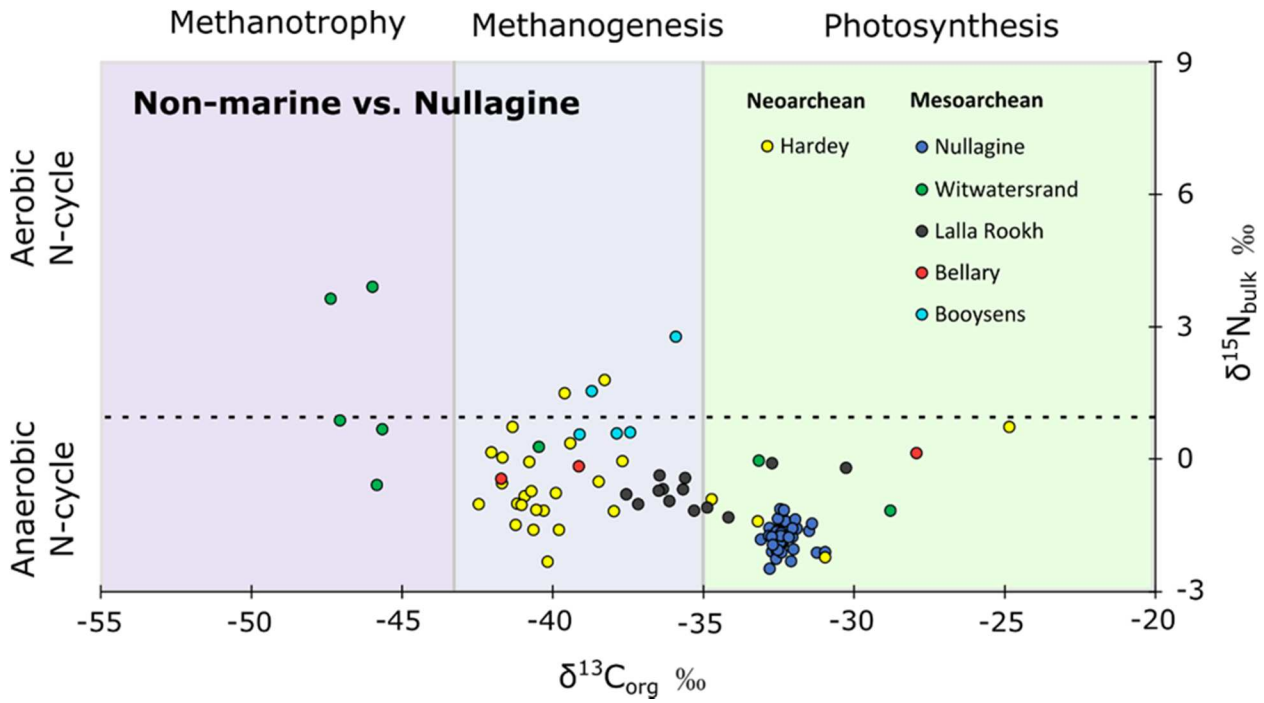

Figure 0.3**. Cross-plots of $\delta^{13}C_{org}$ vs. $\delta^{15}N_{bulk}$ comparing non-marine data from the Mesoarchean and Neoarchean to the data in this study**. Hardey and Bellary data are from Stüeken et al., (2017). Witwatersrand (including the Booysens data) are from Stüeken et al., (2015). Booysens points that are distinguished from the rest of the Witwatersrand data were deposited in brackish water – marine environment with a noticeable fluvial contribution. Lalla Rookh data come from Stüeken and Buick (2018).

References

Garvin, J., Buick, R., Anbar, A.D., Arnold, G.L., Kaufman, A.J., 2009. Isotopic Evidence for an Aerobic Nitrogen Cycle in the Latest Archean. Science 323, 1045–1048. https://doi.org/10.1126/science.1165675

Koehler, M.C., Buick, R., Kipp, M.A., Stüeken, E.E., Zaloumis, J., *in review*. A transient Archean oxygen oasis recorded in the ~2.66 Ga Jeerinah Formation, Australia.

Stüeken, E.E., Buick, R., Guy, B.M., Koehler, M.C., 2015. Isotopic evidence for biological nitrogen fixation by molybdenum-nitrogenase from 3.2 Gyr. Nature 520, 666-U178. https://doi.org/10.1038/nature14180

Stüeken, E.E., Buick, R., Anderson, R.E., Baross, J.A., Planavsky, N.J., Lyons, T.W., 2017. Environmental niches and metabolic diversity in Neoarchean lakes. Geobiology 15, 767–783. https://doi.org/10.1111/gbi.12251

Stüeken, E.E., Buick, R., 2018. Environmental control on microbial diversification and methane production in the Mesoarchean. Precambrian Res. 304, 64–72.

Stratigraphy [m]	$\delta^{15}N_{bulk}$ [‰]	1σ	$\delta^{13}C_{org}$ [‰]	1σ	TN [%]	TOC [%]	C/N [atomic]	TIC [%]
69.65	-2.1	0.37	-32.7	0.06	0.009	0.34	46	22
71.25	-2.5	0.71	-32.8	0.28	0.007	0.26	44	32
72.05	-1.7	0.22	-32.8	0.10	0.010	0.38	43	21
73.3	-1.8	0.17	-33.1	0.01	0.009	0.31	39	25
74.65	-1.7	0.30	-32.5	0.04	0.011	0.40	41	21
75.65	-2.1	0.24	-32.6	0.04	0.010	0.35	43	22
76.6	-1.9	0.17	-32.4	0.01	0.009	0.33	41	25
77.45	-1.9	0.27	-32.4	0.10	0.009	0.36	46	24
78.6	-1.5	0.08	-32.2	0.02	0.009	0.40	53	26
79.6	-1.9	0.34	-32.5	0.08	0.009	0.37	46	24
80.45	-1.4	0.02	-32.5	0.02	0.010	0.38	43	22
81.25	-1.7	0.20	-32.5	0.08	0.010	0.37	44	24
82.25	-1.9	0.22	-32.6	0.04	0.010	0.38	43	23
83.05	-1.8	0.25	-32.4	0.01	0.010	0.37	43	23
84.5	-1.6	0.17	-32.6	0.01	0.010	0.38	45	24
85.5	-1.8	0.34	-32.5	0.01	0.010	0.35	42	24
86.7	-1.8	0.17	-32.0	0.09	0.011	0.42	44	25
87.8	-1.9	0.15	-32.4	0.03	0.009	0.35	44	26
89.05	-2.0	0.24	-32.0	0.03	0.008	0.45	63	24
90	-1.6	0.20	-32.8	0.17	0.012	0.34	34	22
94.8	-1.6	0.41	-31.5	0.40	0.002	0.07	48	16
97.45	-1.5	0.83	-31.4	0.30	0.002	0.07	47	14
98.5	-2.3	0.54	-32.6	0.13	0.008	0.26	40	27
99.5	-1.7	0.09	-32.5	0.01	0.010	0.32	39	23
102.5	-2.1	0.50	-31.2	0.15	0.003	0.06	20	16
104.8	-2.1	0.25	-31.0	0.59	0.003	0.05	16	22
105.75	-1.7	0.51	-32.8	0.02	0.011	0.31	31	20
110.7	-1.3	0.16	-32.4	0.05	0.011	0.32	35	25
113.85	-1.4	0.30	-32.3	0.06	0.011	0.38	41	23
114.85	-1.6	0.71	-31.9	0.15	0.008	0.46	64	30
115.7	-1.4	0.44	-32.0	0.10	0.010	0.43	49	27
116.75	-1.7	0.11	-32.2	0.03	0.010	0.41	48	26
117.65	-1.6	0.37	-32.2	0.04	0.010	0.40	48	25

121.85	-1.6	0.20	-32.6	0.00	0.010	0.38	46	26
122.35	-1.7	0.23	-32.4	0.03	0.009	0.40	51	29
124.65	-1.4	0.15	-32.5	0.01	0.012	0.40	40	25
125.45	-1.1	0.05	-32.5	0.02	0.011	0.36	37	21
127.7	-1.2	0.53	-32.3	0.03	0.010	0.37	43	25
129	-1.7	0.59	-32.4	0.04	0.007	0.26	40	32
130	-2.3	0.23	-32.1	0.12	0.009	0.40	60	21
131.05	-1.6	0.42	-32.1	0.08	0.010	0.31	36	26
132.2	-1.7	0.68	-32.4	0.11	0.010	0.37	44	27
133.2	-1.8	0.45	-32.2	0.09	0.011	0.37	41	25
134.15	-2.1	0.41	-32.4	0.06	0.009	0.25	32	31
136.45	-2.1	0.35	-32.5	0.08	0.013	0.37	34	22
137.05	-1.8	0.55	-32.7	0.09	0.014	0.33	28	23
138.05	-1.9	0.38	-32.7	0.09	0.013	0.33	30	22
Average	**-1.8**	**0.33**	**-32.3**	**0.09**	**0.009**	**0.34**	**42**	**24**
1σ	**0.29**		**0.41**		**0.002**	**0.10**	**8.9**	**3.6**

Table 0.6. **Bulk measurements from the Mesoarchean Mosquito Creek Formation, Chapter 2**.

Table 0.7. **Kerogen measurements from the Mesoarchean Mosquito Creek Formation, Chapter 2**.

Stratigraphy [m]	$\delta^{15}N_{kerogen}$ [‰]	1σ	$\delta^{15}N_{bulk}$ [‰]	$\delta^{13}C_{org}$ [‰]	1σ	TN [%]	TOC [%]	C/N [atomic]	$F_{kerogen}$
74.65	-3.2	0.03	-1.7	-32.8	0.01	0.055	20.2	417	0.10
80.45	-3.0	0.09	-1.4	-32.5	0.08	0.065	21.9	389	0.11
86.7	-2.5	0.36	-1.8	-32.1	0.03	0.037	12.1	367	0.12
90	-2.6	0.46	-1.6	-32.7	0.15	0.054	18.3	382	0.09
105.75	-3.0	0.15	-1.7	-32.9	0.09	0.053	16.8	352	0.09
115.7	-2.5	0.17	-1.4	-32.1	0.04	0.061	21.1	392	0.12
124.65	-1.6	0.43	-1.4	-32.5	0.01	0.073	18.9	307	0.13
137.05	-1.6	0.43	-1.8	-32.8	0.00	0.069	16.5	278	0.10
Average	**-2.5**	**0.26**		**-32.6**	**0.05**	**0.058**	**18.2**	**360**	**0.11**
1σ	**0.59**			**0.31**		**0.01**	**3.1**	**46.5**	**0.02**

7.2 *Chapter 3*

Supplementary materials for "Transient surface ocean oxygenation recorded in the ~2.66 Ga Jeerinah Formation, Australia"

Authors:
Matthew C. Koehler, Roger Buick, Michael A. Kipp, Eva E. Stüeken, and Jon Zalousmis

7.2.1 *Methods*

Sample Preparation

Sample preparation for bulk rock analyses followed the methodology outlined in (24) and all reagents were reagent grade. Cleanly crushed sample powders were decarbonated with 6N HCl at 60^0C in three iterations of ~24 hours. The powders were then thoroughly rinsed three times with 18MΩ milli-Q water and left to dry for at least two days in a ventilated drying oven at 60^0C.

Kerogen was extracted from a subset of samples, following the method of (25, 41). For each sample 1-2 grams of powder were weighed out into a 250ml Teflon bottle and treated with 100ml of 50% v/v HF in a shaking water bath at 60ºC overnight to dissolve the silicate matrix. Residual fluoride precipitates were removed with 100 ml of saturated boric acid in 50% v/v HF. The samples were washed thoroughly three times with 200ml 18MΩ milli-Q deionized water. The remaining kerogen was then poured into pre-combusted scintillation vials with ~10ml of water and then freeze-dried for two days.

Samples were prepared for selenium analysis following published methods (90). Bulk rock powders were digested with HF, HNO_3 and $HClO_4$ at 130°C in closed Teflon beakers, and the selenium was isolated using filtration columns packed with thiol-cotton fiber. The samples were further purified with aqua regia, evaporated to incipient dryness and redissolved in 0.6N HCl for analyses.

Analytical methods

Total organic carbon (TOC), $\delta^{13}C_{org}$, total nitrogen (TN), $\delta^{15}N_{bulk}$, and $\delta^{15}N_{kerogen}$ values were measured using a Costech ECS 4010 Elemental Analyzer coupled to a Thermo Finnigan MAT253 continuous-flow isotope-ratio mass spectrometer. Three in-house standards ("GA1", "GA2", and "SA") calibrated with reference materials USGS40 and USGS41 (26) were used to calibrate isotope measurements and monitor accuracy, while a rock standard ("UW McRae") was used to test long term precision. For $\delta^{15}N$, the average analytical accuracy (based on GA1) and the average analytical precision (based on UW McRae) was 0.12 ± 1.0‰, and 0.13‰ respectively. The average standard deviation of $\delta^{15}N_{bulk}$ values for sample replicates was 0.3‰, with most of the imprecision occurring towards the bottom of the cores where total nitrogen values are lowest (Table 3.1).

Selenium analyses were carried out on a multicollector inductively-coupled-plasma mass spectrometer (Nu Instruments) coupled to a hydride-generator, using standard-sample bracketing to correct for instrument drift and mass bias. Correction for isobaric interferences followed the method of (90). Data are expressed as $\delta^{82/78}Se$ relative to NIST SRM 3149. The average precision (1σ) for samples was 0.07‰ for $\delta^{82/78}Se$ values and 0.01 ppm for Se concentrations. $\delta^{82/78}Se$ values for international reference material SGR-1 and in-house standard UW-McRae were -0.01 ± 0.10‰ (1σ, n = 4) and +0.87 ± 0.12‰ (1σ, n = 7), respectively, which agree well with published values (5, 277).

Linear Regression Model

A linear regression model was used to identify stratigraphic locations associated with statistically significant shifts in $\delta^{15}N_{bulk}$ throughout the drill cores. The model follows that described by (91), which was developed to identify stratigraphic changes in ice core geochemistry. This model divides the core into stratigraphically ordered sub-blocks and uses linear regression to address the null hypothesis that the slope through the $\delta^{15}N_{bulk}$ values is 0. We used a range of sub-block sizes from 9 to 16 samples to rigorously identify stratigraphic changes in $\delta^{15}N_{bulk}$, as the regression is sensitive to block size. For each size, the block is moved along the core in intervals of 1 sample. The output is a matrix that identifies block sizes coupled to average stratigraphic position where the probability value (p) < α; i.e. where the slope of the linear regression is non-zero. α is calculated based on the number of realizations (r) that the model produces (how many regressions are performed), to minimize type I error:

$\alpha = 0.05^{(1/r)}$

We did not apply this model to the Se data because of the much smaller number of data points.

7.2.2 *Identifying authigenic Se enrichments*

In light of recent work that has shown that small apparent authigenic trace metal enrichments can instead be explained via lithological variability (278), we attempted to more robustly verify the reality of Se enrichments in both cores. Due to insufficient sensitivity, the USGS database utilized in (278) to derive confidence intervals for other trace metal enrichment factors cannot statistically be applied to the Se system. However, the range of observed [Se] values in topsoils falls squarely within the most recently published range of estimates for the Se concentrations of average upper crust (18-196 ppb; *ref.* (279). For our data, we have calculated Se

enrichment factor (EF) following the protocol of (5), which used a crustal Al concentration of 8.04 wt. % (280) and a crustal Se concentration of 140 ppb (281). While more recent estimates have been published (282), we adopted these values so that the data can be compared to the previously published Se results from the Mt McRae shale. In order to account for potential variability in crustal Se sources, we use the range of 18-196 ppb Se divided by the crustal Al value of 8.04 wt. % in order to determine a "confidence interval" of EF values in which authigenic enrichment cannot be unambiguously distinguished. This calculation reveals that EF values ranging from 0.1 to 3.2 can potentially derive from solely detrital Se input. The increase to Se EF values of ~40 in AIDP-2 are thus confidently interpreted to represent true authigenic Se enrichment. Likewise, samples near the top of AIDP-3 are slightly enriched in Se as well, revealing that some Se oxyanions were still be sourced to the basin via oxidative weathering at this time.

7.2.3 *Correlating the cores*

An impact spherule layer found towards the bottom of the Carawine Dolomite in AIDP-2 and at the top of the Jeerinah Formation in AIDP-3 is the primary correlation point between the two cores (Figure 0.5). The stratigraphy from the bottom of the spherule layer to the $\delta^{15}N$ value increase at the stage *II-III* boundary in each core is as follows:

AIDP-2 (shallower): ~60 meters of calc/dolarenite and black dolosiltite

~45 meters of black shale

AIDP-3 (deeper): ~60 meters of black shale/pyritic black shale

It is not unreasonable to suggest that the deposition of these parts of the stratigraphy from each core were synchronous, given the potential for much faster sedimentation rates of arenites and siltites compared to black shale. Indeed, it is very unlikely that the positive Stage *II* $\delta^{15}N$ values in AIDP-3 correlate to any part of the Carawine Dolomite. If other redox-sensitive trace metals (e.g. Mo, Cr, Ni) are enriched in both cores in phase with the nitrogen isotope excursions, then the evidence for our correlation between the two cores would be even more compelling.

7.2.4 *Metamorphism*

Numerous studies of basalts immediately underlying the Jeerinah Formation in the vicinity of AIDP-2 and -3 have identified mafic mineral assemblages clearly indicative of prehnite-pumpellyite facies metamorphism (283–285). This classical method of determining metamorphic grade has recently been questioned (66) based on pelitic mineral assemblages and chlorite geothermometry in AIDP-2, arguing instead for upper greenschist facies metamorphism at temperatures as high as ~420°C. However, there are several reasons for thinking that this interpretation is invalid. Firstly, it is hard to conceive of circumstances whereby every basalt sample in 3 large regional studies was retrogressed to prehnite-pumpellyite grade after peak greenschist metamorphism leaving no palimpsests of the precursor greenschist amphiboles. Secondly, the mineralogy of the AIDP-2 and AIDP-3 shales themselves contradicts greenschist peak metamorphism, as the key pelitic minerals of upper greenschist facies: biotite, garnet, andalusite, pyrophyllite and chloritoid, are nowhere evident (Figure 0.8) and the key mineralogical events that are evident: stilpnomelane-in, rutile-in and illite→muscovite all occur in the anchizone (286) which is equivalent to the mafic prehnite-pumpellyite facies. Moreover, the overlying Carawine Dolomite in AIDP-2 has no talc or tremolite, typical minerals in siliceous dolomites

metamorphosed to upper greenschist facies. Lastly, the chlorite geothermometer used by Peters and colleagues (equation Chl(2) of (67) assumes that all iron present in chlorite is Fe^{2+}, an assumption that is unlikely to be valid in the Jeerinah Formation which is conformably overlain by the magnetitic Marra Mamba Iron Formation (AIDP-3) and the BIF-bearing Carawine Dolomite (AIDP-2). This approach has been shown to yield temperatures up to 200°C too high for chlorites known to have crystallized at ~300°C when there is some Fe^{3+} in the system (68). Moreover, the temperature ranges obtained with this geothermometer are infeasibly broad, from 309°C to 498°C over 160 m in AIDP-2 and 354°C to 497°C over 45 m in AIDP-3 (assuming 2 kbar pressure). Rocks in such stratigraphic proximity should have undergone very similar metamorphic conditions. Thus we conclude that the prehnite-pumpellyite grade determined from the underlying mafic rocks is more likely representative of the true metamorphic conditions experienced by the Jeerinah shales of AIDP-2 and AIDP-3 than the apparently erroneous upper greenschist temperatures calculated from an unreliable chlorite geothermometer.

7.2.5 *Figures*

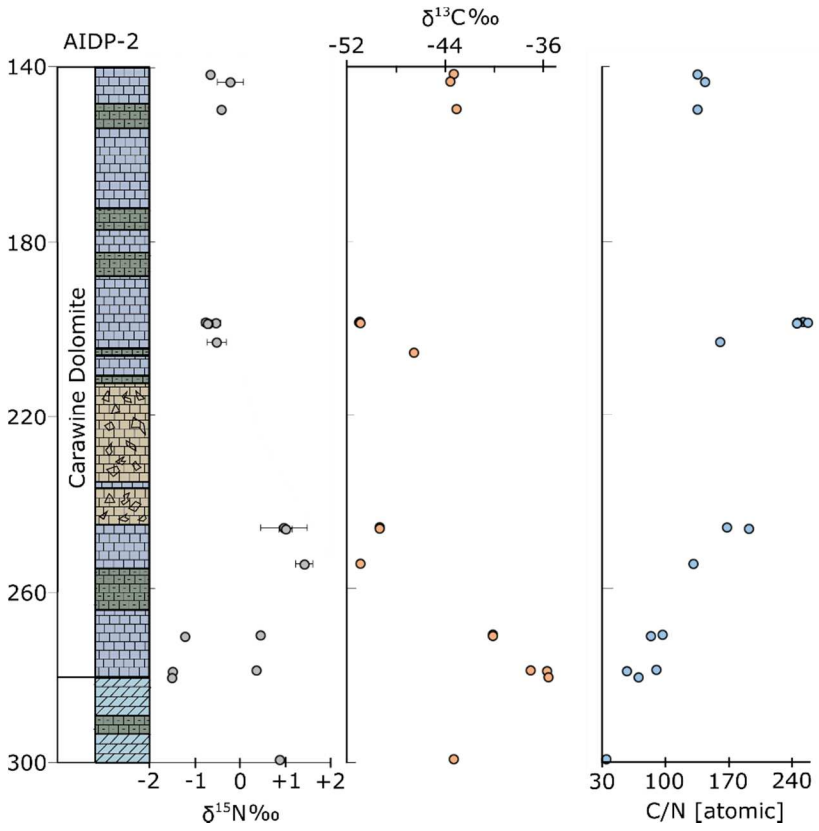

Figure 0.4**. Chemostratigraphy of the Carawine Dolomite from AIDP-2 showing $\delta^{15}N_{bulk}$, $\delta^{13}C$, and C/N ratios.** Down-core depth is given in meters. The $\delta^{15}N_{bulk}$ values are similar to the underlying stage *III* in AIDP-2.

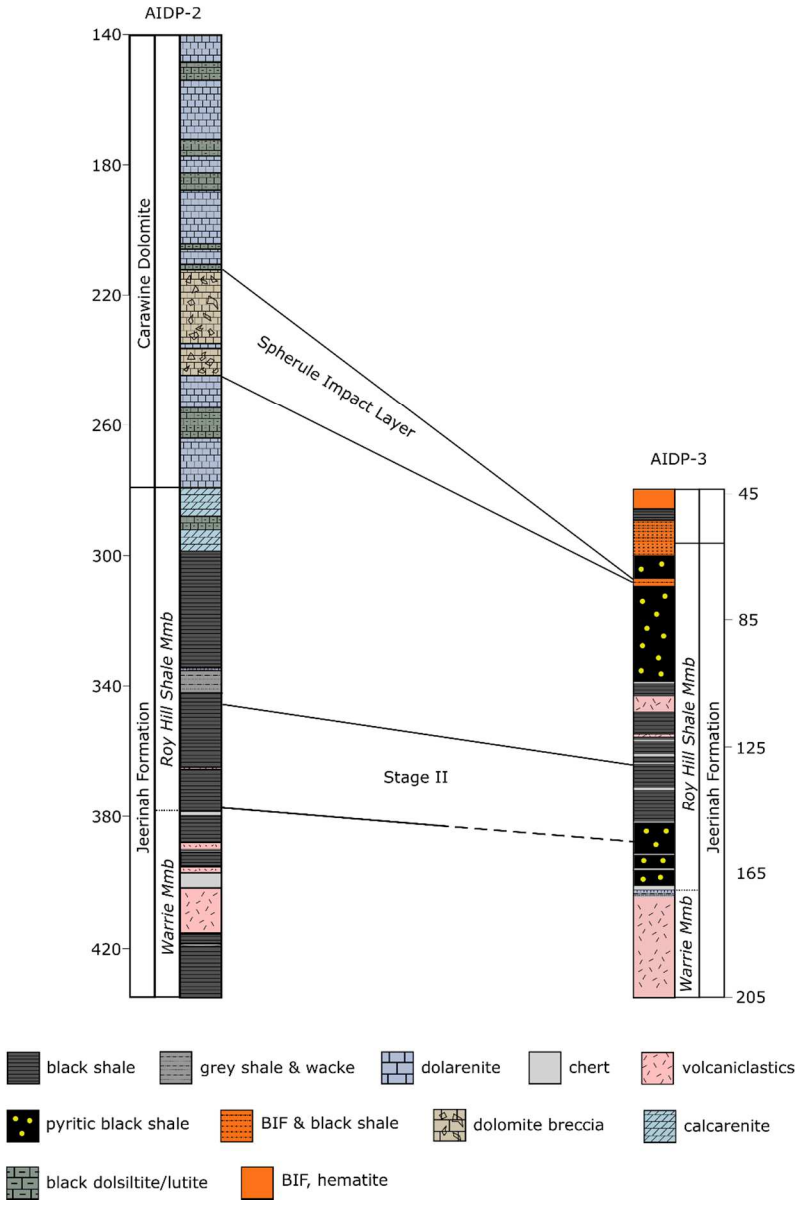

Figure 0.5**. Drill cores AIDP-2 and AIDP-3 correlated using the impact spherule layer and nitrogen isotope Stage *II* as described in the main text.** The dashed line for the lower Stage *II* boundary as it approaches AIDP-3 indicates that the precise stratigraphic extent of elevated $\delta^{15}N$ values that defines Stage *II* is unknown for AIDP-3. This is because Stage *I* in AIDP-3 hosts altered $\delta^{15}N$ values.

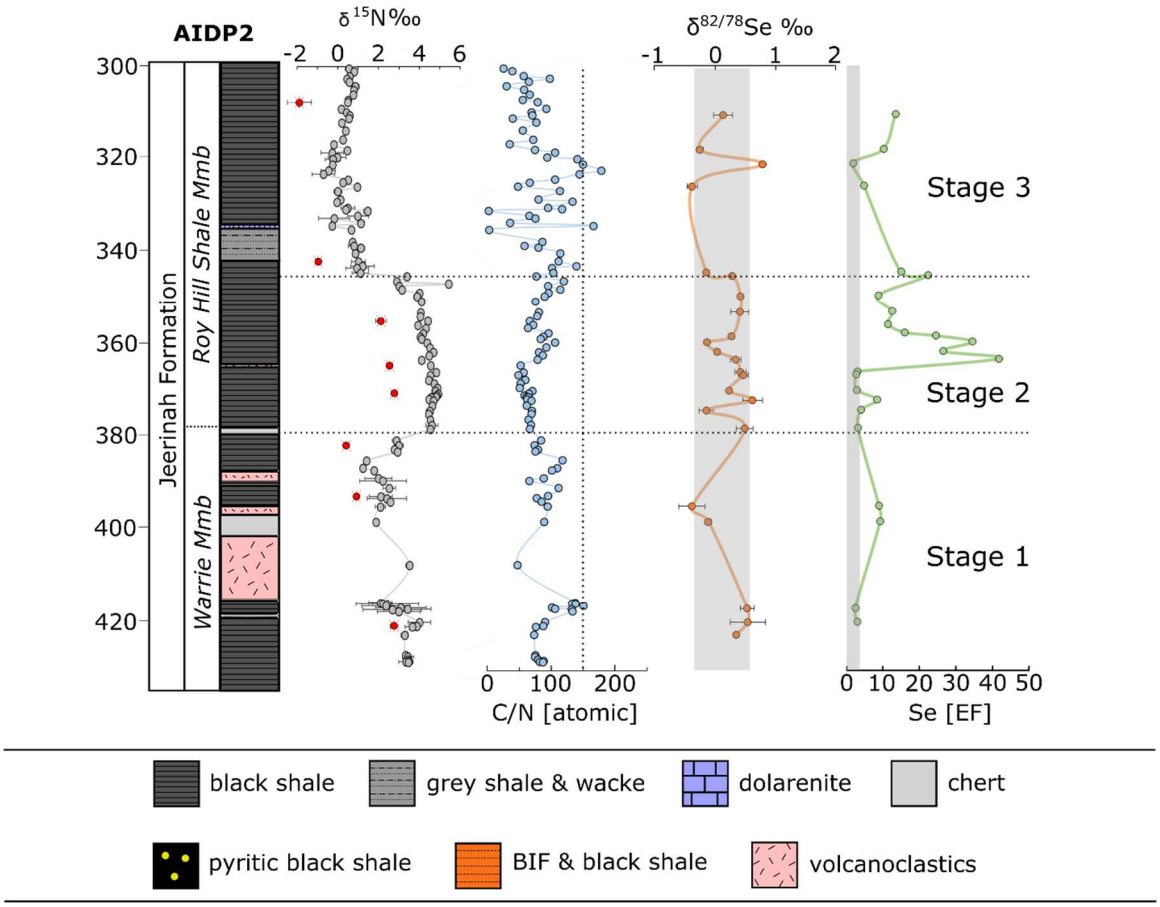

Figure 0.6**. Same as Figure 3.2 in text, but shows selenium EF (normalized to aluminum) instead of selenium ppm.** This, coupled with Figure 3.1C and Figure 3.1D, demonstrates that the increase in Se during Stage *II* of AIDP-2 is likely not due to lithological changes. For comparison, the Se EF enrichment in the McRae shale is over 3 times greater than the enrichment found here. Grey vertical bars represent crustal values.

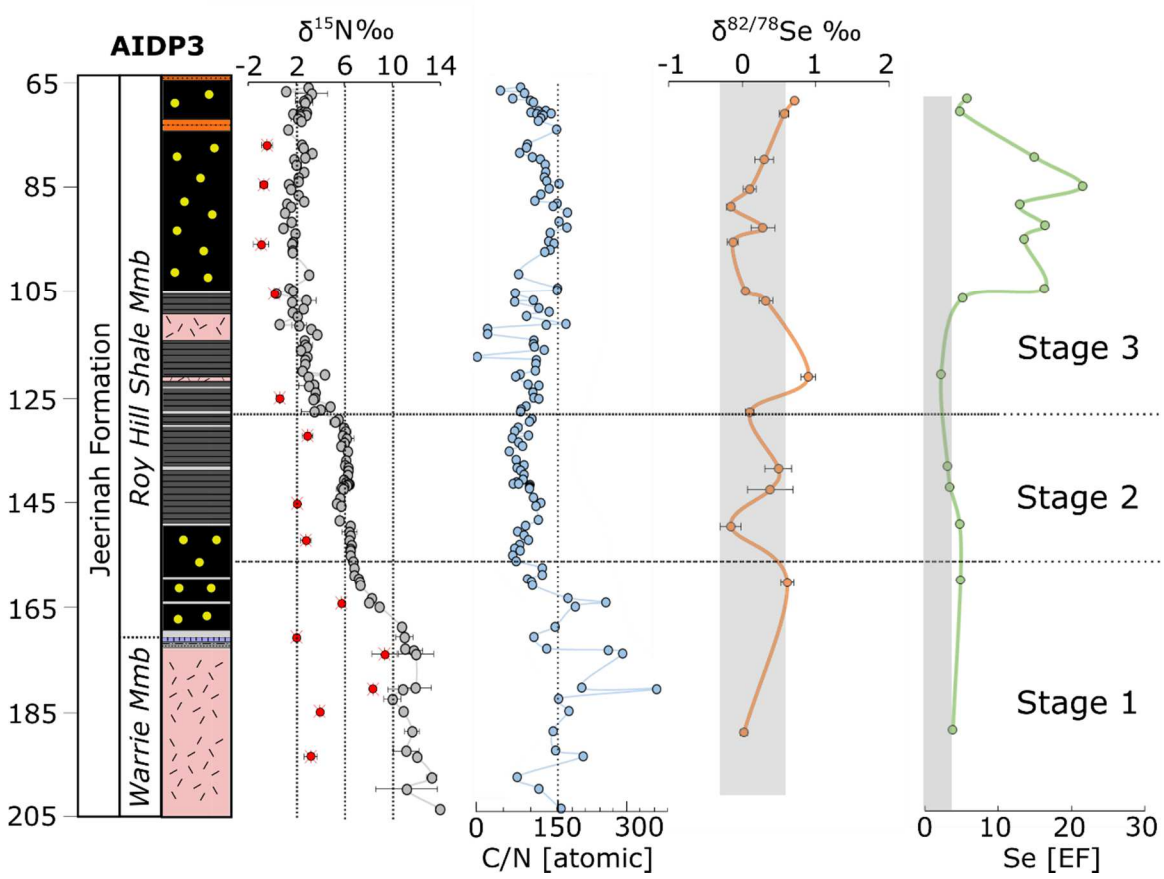

Figure 0.7**. Same as Figure 3.3 in text, but shows selenium EF (normalized to aluminum) instead of selenium ppm.** Note the different x-axis scale from Figure 0.6. Grey vertical bars represent crustal values.

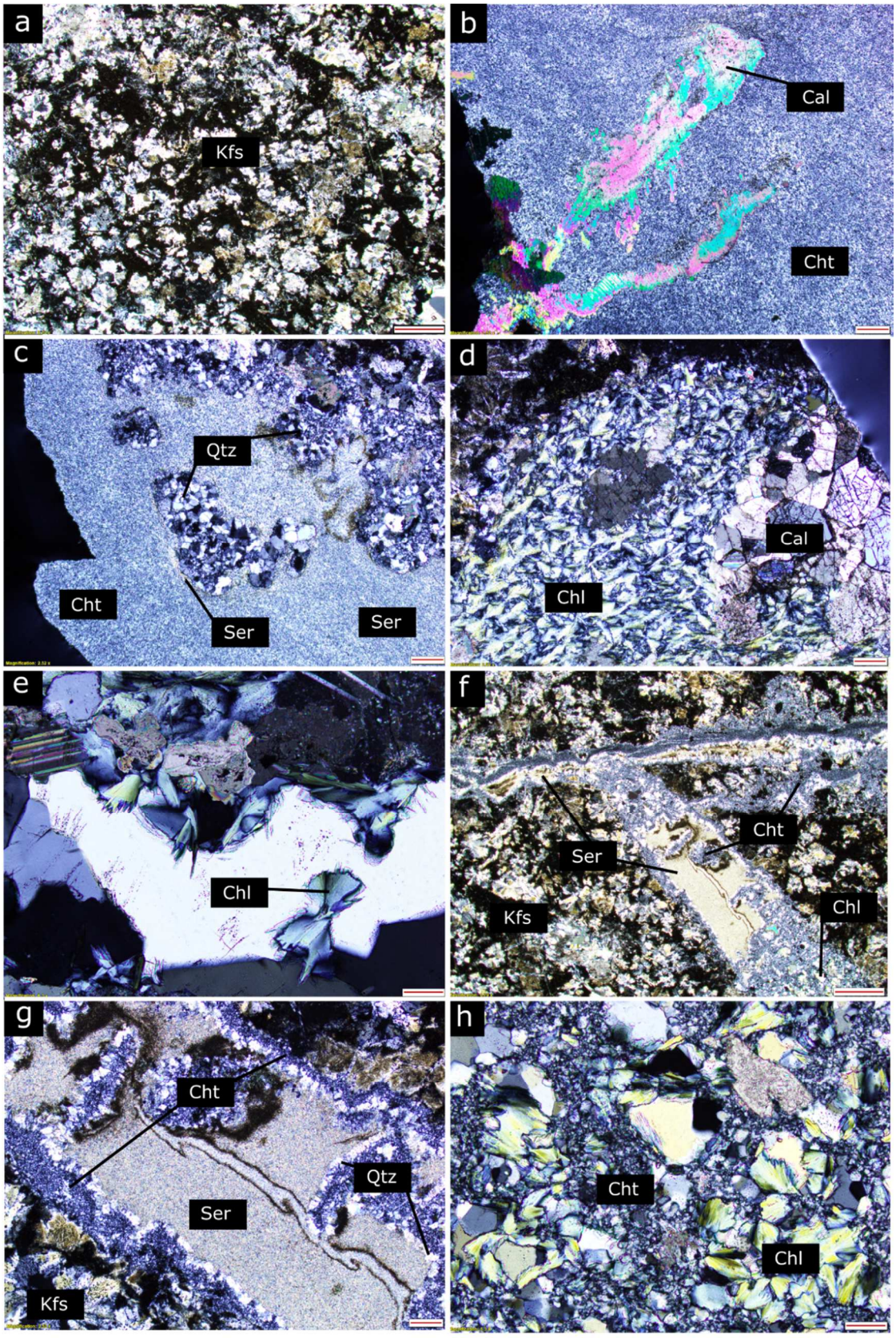
a
Kfs
b
Cal
Cht
c
Qtz
Cht
Ser
Ser
d
Cal
Chl
e
Chl
f
Cht
Ser
Kfs
Chl
g
Cht
Qtz
Ser
Kfs
h
Cht
Chl

Figure 0.8**. Thin section images from the basalt underlying the Jeerinah Fm at 252.72m stratigraphic depth, containing characteristics of multiple metasomatic episodes.** Panel “a” is groundmass comprising K-feldspar spherulites (Kfs). Panels “b-e” are of amygdales. “b” and “c” are of the same large amygdale, filled with chert (Cht) and sericite (Ser) with calcite (Cal) veins, and blocky quartz (Qtz). “d” and “e” are of different amygdales with abundant chlorite (Chl), chlorite overgrowths, and larger calcite crystals. “f” is a large chert vein with sericite intraveins surrounded by blocky quartz crystals, and with abundant chlorite in some regions. “g” and “h” are zoomed-in images of “f”. Scale bars are 1mm for panels “a” and “f”, 200µm for panels “b”, “c”, “d”, and “g”, and 100µm for panels “e”, and “h”.

How to get elevated primary $\delta^{15}N$ values > ~ +1‰

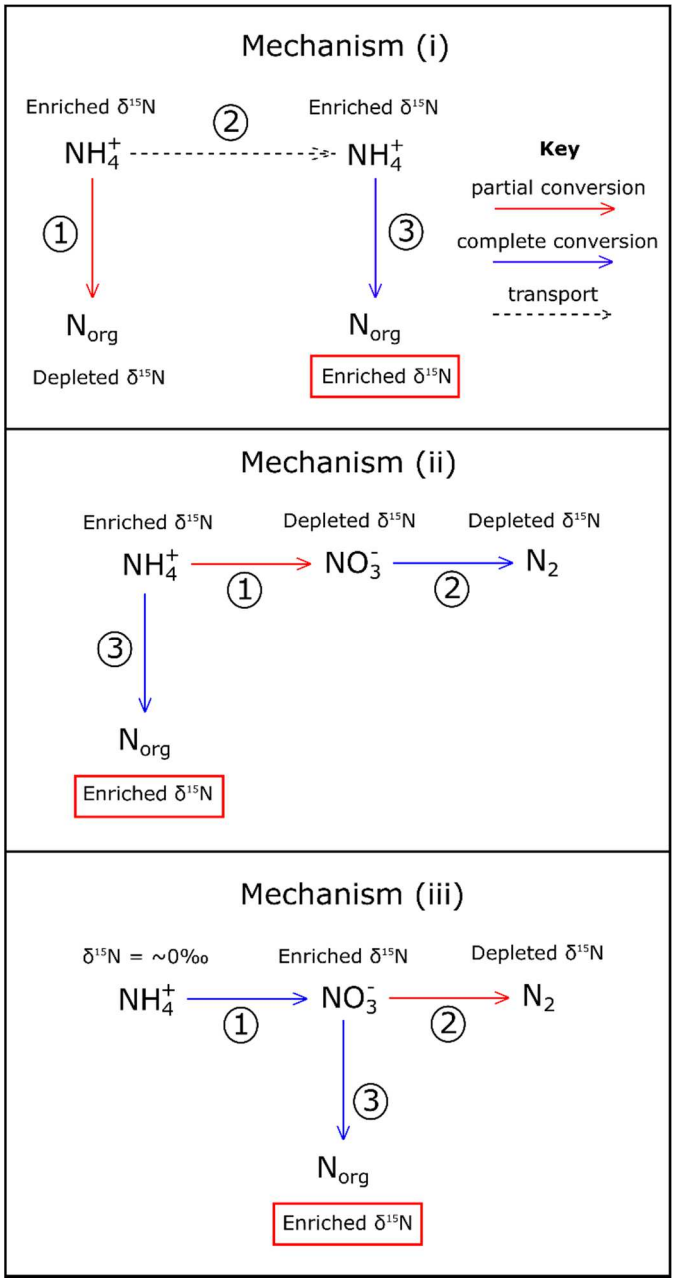

Schematic representation of mechanism (i) described in the text: (1) An ammonium pool is partially assimilated into biomass**.** The biomass preserved in sediments at this location in the basin records a depleted $\delta^{15}N$ value. This leaves the residual NH_4^+ pool enriched in $\delta^{15}N$. (2) The enriched residual NH_4^+ pool is transported to another part of the basin. (3) The enriched NH_4^+ pool is assimilated into biomass, resulting in elevated $\delta^{15}N$ values recorded in the sediments.

Schematic representation of mechanism (ii) described in the text: (1) An ammonium pool is partially nitrified to NO_3^-. This results in a residual NH_4^+ pool enriched in $\delta^{15}N$ and a NO_3^- pool depleted in $\delta^{15}N$. (2) The nitrate is completely denitrified, removing the depleted $\delta^{15}N$ from the system by conversion to N_2 gas. (3) The enriched NH_4^+ pool is assimilated into biomass, resulting in elevated $\delta^{15}N$ values recorded in the sediments.

Schematic representation of mechanism (iii) described in the text: (1) An ammonium pool is completely nitrified to NO_3^-, with no isotopic change between the reactant NH_4^+ pool and product NO_3^- pool. (2) The nitrate pool is partially denitrified to N_2, resulting in depleted $\delta^{15}N$ lost as N_2, and a residual $\delta^{15}N$-enriched nitrate pool. (3) The enriched NO_3^- pool is assimilated into biomass, resulting in elevated $\delta^{15}N$ values recorded in the sediments.

Figure 0.9**. Schematic representation of the mechanisms that result in elevated $\delta^{15}N$ values as described in the text.** Note that all pathways (denoted by the red and blue arrows) have a net isotopic preference for the light isotope ^{14}N. That preference is expressed in instances of partial conversion (red arrows), but not in instances of complete conversion (blue arrows). The starting $\delta^{15}N$ value for the initial NH_4^+ in each case is ~0‰, consistent with nitrogen fixation by the Mo-nitrogenase. Note that the only mechanism that incorporates a spatial component is mechanism (i). For a full schematic of the nitrogen cycle, including fractionation factors and oxidation state for each reaction/species, see Figure 4 of (38).

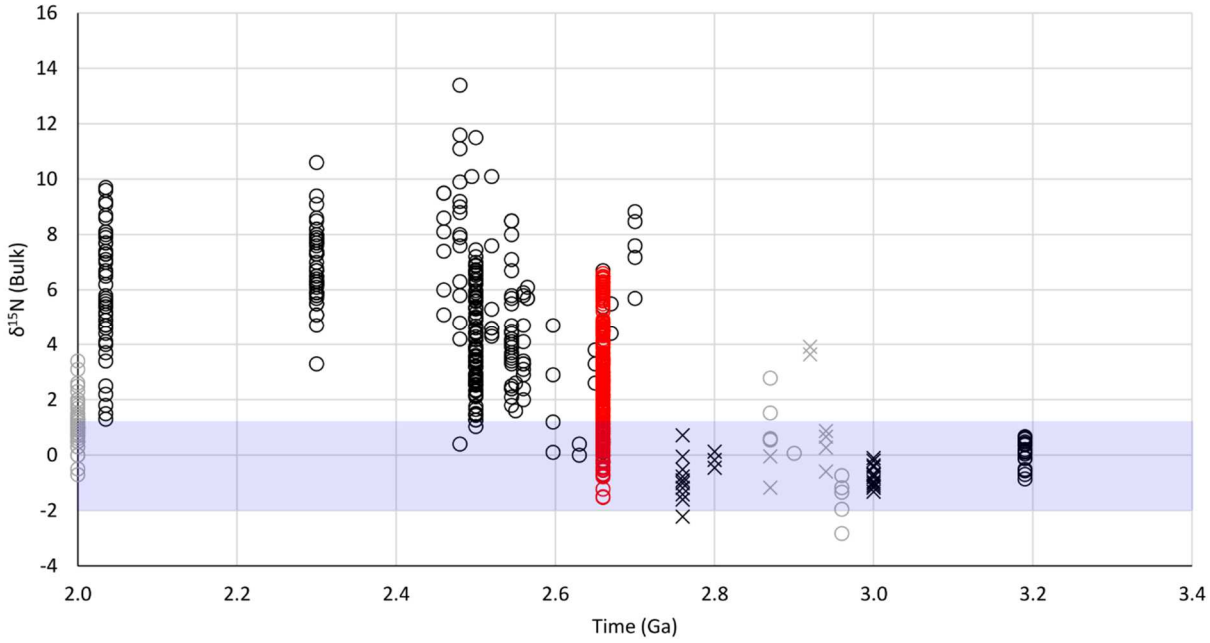

Figure 0.10**. Least-altered $\delta^{15}N$ values from 3.4 Ga to 2.0 Ga.** Circles are marine data points, X's are non-marine data points. Black points are lower- sub greenschist samples, grey points are greenschist samples, and red points are from this study. Blue shaded area covers $\delta^{15}N$ values consistent with nitrogen fixation by the Mo-nitrogenase. Data taken from a compilation in (38), with added data from (17, 45, 287). While there are more $\delta^{15}N$ values from the Archean not shown here, the fidelity of the measurements based on potential alteration and/or large analytical uncertainly (see supplementary materials of (41) have been excluded.

7.3 *Chapter 4*

Supplementary tables for "Spatial and temporal trends in Precambrian nitrogen cycling: a Mesoproterozoic offshore nitrate minimum"

Authors:
Matthew C. Koehler, Eva E. Stüeken, Michael A. Kipp, Roger Buick, and Andrew H. Knoll

Table 0.8. **Kerogen data. Included are data from both the Roper and the Bangemall groups, Chapter 4**.

Sample ID	$\delta^{15}N_{kerogen}$ [‰]	1σ [‰]	C/N_{ker} [atomic]	F (N_{ker}) [%]	F (N_{sil}) [%] *
Bangemall:					
90050	2.73		126		
90079	5.87	0.30	39.1	71	29
89138	4.38	0.06	103.2		
89094	2.16	0.20	70.2	40	60
89036	3.22		81.1	44	56
89028	1.27	0.30	97.4	86	14
Roper:					
A391.0	4.57	0.55	80.1	24	76
BR1 23.4	2.55		89.8	2	98
BR1 244.7	2.63		110.1	4	96
GG1 53.2	2.86		46.9	18	82
U4 33.2	5.34	0.12	61.0	66	34
U4 82.25	3.55	0.42	68.5	23	77

**To calculate the fraction (F) of silicate and kerogen bound nitrogen:*

$$\left(\frac{N\ [\%]}{C\ [\%]}\right)_{kerogen} * TOC[\%]_{bulk} = N[\%]_{kerogen}$$

$$\frac{N[\%]_{kerogen}}{N[\%]_{bulk}} = F_{kerogen}$$

$$1 - F_{kerogen} = F_{Silicate}$$

Table 0.9. **New data from the Bangemall Group, Chapter 4**.

Sample ID	Position [m]	Facies	TN [ppm]	$\delta^{15}N_{bulk}$ [‰]	1σ $\delta^{15}N$ [‰]	TOC [ppm]	$\delta^{13}C_{org}$ [‰]	1σ $\delta^{13}C$ [‰]	C/N [atomic]	$\delta^{13}C_{carb}$ [‰]	Carb [%]
Fords Creek											
89023	73.95	peritidal	46	4.1	0.30	299	-31.8	0.00	7.6	0.8	72.3
89025	95.7	peritidal	1719	5.4		4249	-29.6		2.9	0.4	89.1
89028	112.5	peritidal	50	0.3	0.57	3454	-31.2	0.11	81.0		
89029	122.7	peritidal	582	3.9		1226	-29.6		2.5	1.2	79.1
89036	160.1	peritidal	661	3.4		2028	-26.8		3.6	-0.3	89.7
89064	207.63	shallow	10	2.9	0.15	415	-28.4	0.00	50.9	-0.1	90.9
89071	418.32	shallow	244	3.7	0.03	7100	-20.8	0.05	34.0	-0.9	86.9
89072	419.34	shallow	127	3.8	0.22	5005	-26.0	0.17	45.9	-0.5	32.2
89074	431.39	shallow	64	3.5	0.25	1705	-30.1	0.03	30.9	-1.2	22.8
89075	449.08	shallow	22	3.5	0.15	291	-27.7	0.13	15.7	-0.6	84.2
89081	511.94	shallow	217	5.6		7094	-28.5		38.2	-1	95.4
89083	519.53	shallow	3390	6.7		17847	-28.6		6.1	-0.7	
89086	578.71	shallow	81	3.3	0.66	850	-28.6	0.13	12.2	0.4	96.7
89090	642.17	deep	58	2.6	0.53	1705	-30.8	0.05	34.6	0.1	77.6
89091	653.91	deep	66	4.0	0.81	213	-29.3	0.27	3.8	-0.7	81.5
89093	671.66	deep	124	2.5		3261	-28.9		30.7	-0.8	97.0
89094	683.4	deep	94	1.6	0.24	2134	-32.7	0.05	26.5	-1.1	
89095	702.15	deep	47	5.3	0.26	377	-28.9	0.27	9.3	-1.1	82.3
89097	722.85	deep	57	3.0	0.11	459	-31.4	0.14	9.4	-1	75.9
89098	733.77	deep	68	2.8	0.00	447	-30.3	0.11	7.7	-0.8	71.6
89100	753.72	deep	48	4.9	1.32	701	-29.6	0.15	17.0	-1.2	91.2
89102	764.08	deep	66	3.1	0.04	414	-30.1	0.08	7.3	-1.3	86.1
89106	873	deep	64	0.9	0.15	4107	-33.5	0.01	74.6	0.2	57.9
89107	882.4	deep	21	-0.9	0.93	999	-35.3	0.02	55.1	0.1	63.2
89108	892.79	deep	90	2.6	0.16	9569	-34.5	0.02	123.6	1.1	46.0

89110	906.7	deep	19	2.1	0.31	127	-27.8	0.08	7.8	-0.8	
89122	587.2	shallow	46	1.9	0.32	1963	-30.0	0.04	49.4	-0.6	
89123	538.5	shallow	35	2.1	0.55	3654	-33.5	0.03	122.7	-1.1	59.5
89125	458.2	shallow	265	5.5	0.43	456	-27.9	0.65	2.0	0.3	84.6
89127	141.3	peritidal	86	3.9		2157	-27.9		29.3	0.4	94.4
89130	65.4	peritidal	78	2.7		1908	-28.5		28.7	0.8	97.5
90049	534.15	shallow	804	3.7		3639	-32.8		5.3	-0.5	85.5
89028A	112.5	peritidal	1164	2.8		3058	-28.3		3.1	0.8	
89030D	127.9	peritidal	52	1.4	0.46	3273	-29.9	0.08	73.9	0.4	92.6
Irregully											
89165	254.91	peritidal	430	4.2	0.39	2190	-26.7	0.23	5.9	-0.7	88.1
89166	265.24	peritidal	88	5.0		2749	-25.1		36.6	-0.2	95.8
89174	308.06	peritidal	66	-0.2	0.07	1176	-26.0	0.12	20.8	0	96.8
89178	317.94	peritidal	89	3.4		3905	-26.4		51.0	0.2	96.8
89197	369.81	peritidal	58	3.8	0.02	2348	-25.9	0.05	47.1	-0.3	90.5
89222	1190.9	shallow	69	3.8	0.00	1413	-29.0		23.9	-2.1	73.7
89225	1211.94	shallow	54	3.5	0.01	688	-27.4	0.21	14.8	0.6	56.0
89226	1220.24	shallow	49	2.7	0.38	664	-30.0	0.05	15.7	0.2	
89231	1243.19	shallow	905	3.1		953	-31.1		1.2	-0.7	69.8
89232	1252.45	shallow	72	3.7	0.15	1467	-31.2	0.02	23.9	-0.8	
90010	1914.35	shallow	374	3.3		23856	-28.3		74.5	-3.9	99.4
90017	1982.17	deep	104	0.4	0.20	292	-25.2	0.10	3.3	-0.3	46.8
90018	1983.53	deep	272	1.0	0.15	259	-27.3	0.04	1.1	-1.3	
90019	1993.14	deep	389	1.0	0.19	2654	-29.8	0.08	8.0	1.6	
90020	2003.25	deep	244	0.3	0.11	498	-27.1	0.26	2.4	-0.7	52.5
90032	2496.22	deep	398	2.9	0.44	2008	-32.5	0.18	5.9	-2.8	68.5
Wandarry											
90062	61.64	peritidal	61	2.6	0.04	1346	-26.8	0.01	25.8	-0.7	94.6

90088	77.72	peritidal	495	7.5	0.89	2604	-25.0	0.05	6.1	0	77.9
89138	143.9	peritidal	8	2.3	0.20	507	-22.1	0.65	73.9	0.5	38.5
90070	267.17	peritidal	5	2.6	0.40	432	-18.7	0.03	105.5	-0.4	13.1
90080	507	shallow	35	3.6	0.11	423	-28.7	0.01	13.9	-1.1	89.1
90078	519.45	shallow	33	3.2	0.29	741	-29.8	0.03	26.2	-1.4	89.9
90081	524	shallow	39	4.0		586	-28.8		17.7	-1.2	94.4
90079	525.25	shallow	4187	5.4	0.40	9907	-29.6	0.11	2.8	-1.1	93.8
90086	1006.4	shallow	20	1.2	0.43	304	-28.2	0.21	17.5	0.5	89.9
90087	1018.45	shallow	671	3.7	0.38	5767	-29.1	0.08	10.0	1.3	92.5
90085	1037.75	deep	690	0.7	0.30	1015	-31.3	0.10	1.7	1.2	70.3
90084	1038.8	deep	116	2.1	0.47	537	-32.6	0.06	5.4	-0.6	57.0
90082	1042.75	deep	94	1.8	0.14	442	-31.9	0.01	5.5	-0.1	46.4
90083	1050	deep	527	2.9	0.32	648	-31.2	0.05	1.4	-0.7	63.3
Other											
90074		shallow	41	0.1	0.22	5272	-33.8	0.03	150.4		
89063		deep	71	0.1		4433	-32.0		72.4		7.1
89066		deep	52	-1.3		26252	-33.1				6.9
89067		deep	90	0.0		9119	-31.4		118.8		7.7
90016		deep	139	1.8	0.04	7342	-30.6	0.05	61.7		
89050		deep	95	1.7	0.31	306	-23.6	0.07	3.7	-1.8	42.2
89051		deep	80	1.9	0.27	277	-23.8	0.17	4.0	-2.2	57.3

Table 0.10. **New data from the Roper Group**. Facies abbreviations: t.d shoreline = tide-dominated shoreline; sand.d shelf = sand-dominated shelf; s.d shelf = storm-dominated shelf; c.s platform = coastal sand platform. Chapter 4.

Sample ID	Position [m]	Facies	TN [ppm]	$\delta^{15}N_{bulk}$ [‰]	1σ $\delta^{15}N$ [‰]	TOC [ppm]	$\delta^{13}C_{org}$ [‰]	1σ $\delta^{13}C$ [‰]	C/N [atomic]	Carb (%)	Formation
Amoco 82/3											
A101.5	101.5	t.d shoreline	173	2.7	0.48	5002	-31.9	0.05	33.7	8.5	Bessie Creek
A178.0	178	sand.d shelf	36	4.9	0.61	768	-30.8	0.14	25.0	37.1	Jalboi
A311.3	311.3	s.d shelf	47	-1.0	0.11	978	-30.6	0.01	24.2	20.8	Crawford
A331.8	331.8	s.d shelf	165	2.6	0.39	1434	-29.7	0.05	10.1	21.5	Crawford
A375.1	375.1	s.d shelf	199	2.8	0.36	2369	-30.9	0.03	13.9	28.2	Crawford
A391.0	391	s.d shelf	225	3.8	0.41	3992	-30.8	0.01	20.7	15.1	Crawford
A407.65	407.65	s.d shelf	24	-0.9	1.95	336	-28.4	0.23	16.2	18.1	Crawford
A544.1	544.1	s.d shelf	315	2.7	0.31	2593	-30.2	0.07	9.6	27.7	Maironu
A549.25	549.25	s.d shelf	250	3.6	0.43	1191	-29.8	0.17	5.6	27.1	Maironu
A561.05	561.05	s.d shelf	214	2.7	0.46	596	-28.7	0.03	3.2	29.2	Maironu
Broughton 1											
BR1 23.4	23.4	s.d shelf	429	2.1	0.30	794	-30.3	0.10	2.2	21.0	Corcoran
BR1 34.5	34.5	s.d shelf	222	2.3	0.24	686	-30.4	0.03	3.6	12.6	Corcoran
BR1 42.3	42.3	s.d shelf	253	2.3	0.45	1006	-30.9	0.11	4.6	15.9	Corcoran
BR1 52.35	52.35	s.d shelf	179	1.6	0.27	1023	-30.8	0.08	6.7	30.4	Corcoran
BR1 69.0	69	s.d shelf	289	2.7	0.22	774	-29.8	0.13	3.1	21.4	Corcoran
BR1 122.4	122.4	c.s platform	518	3.3	0.27	1041	-30.0	0.09	2.3	33.5	Hodgsen ss
BR1 136.8	136.8	c.s platform	99	4.0	0.42	2122	-31.7	0.07	24.9	14.4	Hodgsen ss
BR1 150.45	150.45	s.d shelf	217	1.8	0.50	1328	-30.7	0.05	7.1	18.9	Crawford
BR1 244.7	244.7	s.d shelf	227	3.7	0.10	914	-29.5	0.02	4.7	18.7	Maironu
Golden Grove 1											
GG1 48.75	48.75	basinal	160	0.5	0.66	3300	-32.0	0.04	24.1	25.9	Velkerri

GG1 53.2	53.2	basinal	326	1.4	0.10	2373	-31.7	0.07	8.5	19.9	Velkerri
GG1 229.50	229.5	s.d shelf	435	2.9	0.08	1620	-32.3	0.01	4.3	16.1	Corcoran
GG1 370.70	370.7	s.d shelf	346	3.4	0.25	978	-30.5	0.02	3.3	8.9	Corcoran
Urapunga 4											
U4 26.4	26.4	c.s platform	544	3.6	0.42	13617	-32.5	0.07	29.2	31.2	McMinn
U4 33.2	33.2	c.s platform	79	3.9	0.43	3779	-32.1	0.00	56.0	44.2	McMinn
U4 82.25	82.25	basinal	375	2.9	0.32	5092	-32.0	0.10	15.9	19.8	Velkerri
U4 124.0	124	basinal	475	2.6	0.14	23859	-33.8	0.21	58.6	22.2	Velkerri
U4 421.5	421.5	s.d shelf	266	1.7	0.46	1908	-32.4	0.05	8.4	25.5	Corcoran
U4 431.0	431	s.d shelf	432	2.5	0.15	3450	-32.5	0.06	9.3	14.5	Corcoran
U4 440.95	440.95	s.d shelf	285	2.8	0.26	1768	-32.6	0.04	7.2	16.9	Corcoran
U4 485.1	485.1	basinal	227	1.9	0.30	1418	-31.2	0.01	7.3	36.8	Corcoran
Other											
Velkerri_CS11		basinal	1409	2.2	0.13	52629	-34.3	0.01	43.6		Velkerri
Velkerri_CS17		basinal	1287	2.3	0.03	62685	-35.8	0.01	56.8		Velkerri
Velkerri_CS9		basinal	1531	2.2	0.23	42574	-32.7	0.03	32.4		Velkerri

7.4 *Chapter 5*

Supplementary figures for "Nitrogen and carbon biogeochemistry across the Ordovician-Silurian boundary at Dob's Linn, Scotland"

Authors:
Matthew C. Koehler, Eva E. Stüeken, and Tony Prave

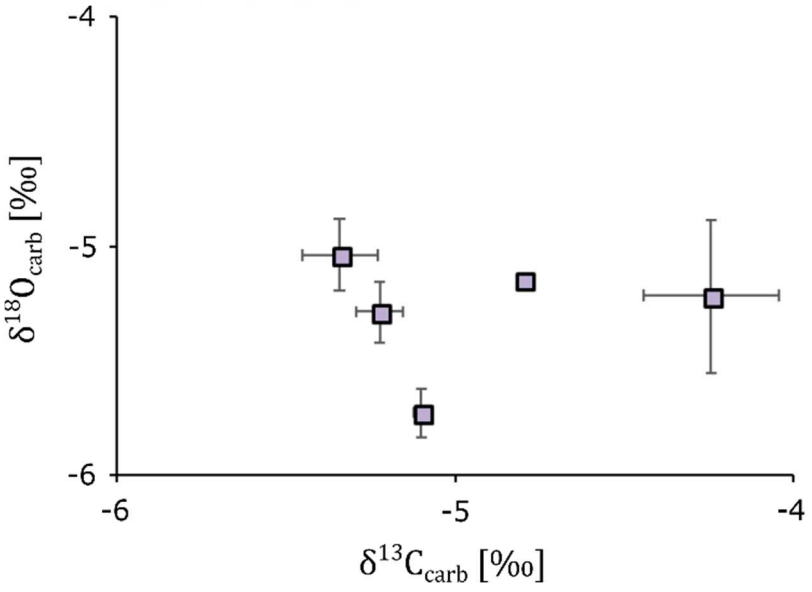

Figure 0.11**. Cross-plot between $\delta^{13}C_{carb}$ and $\delta^{18}O_{carb}$ for carbonates detected during the Hirnantian at Dob's Linn.**

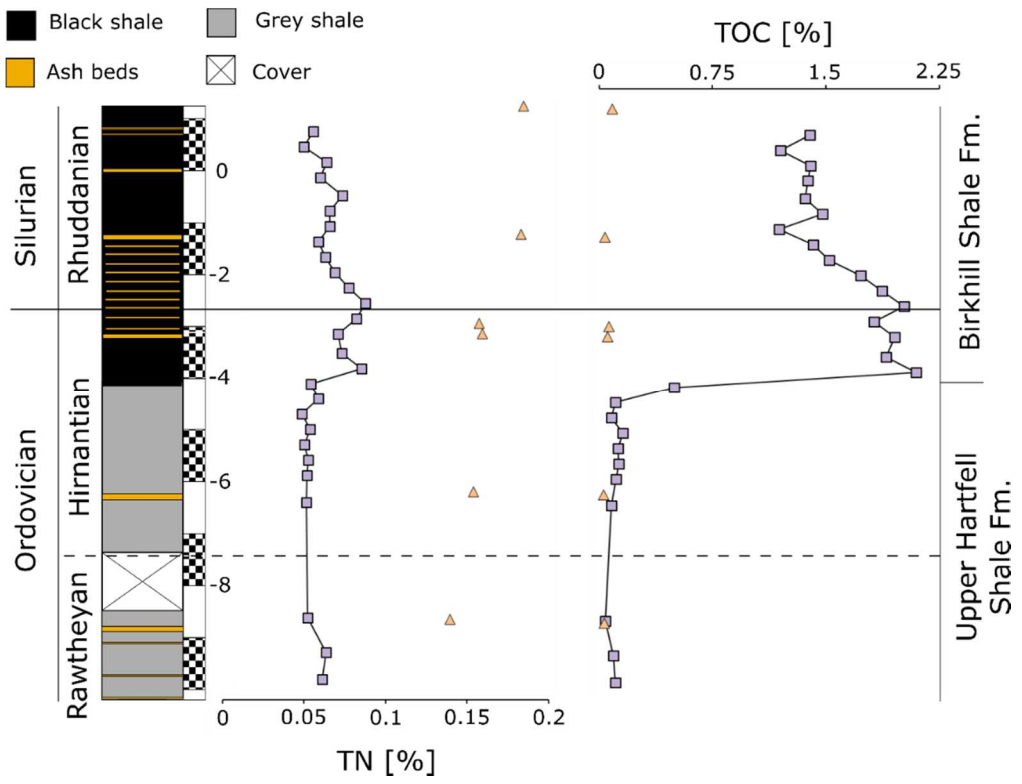

Figure 0.12**. Total nitrogen and organic carbon abundances through the Dob's Linn section.**

Symbols are as in Figure 5.1 of the main text.

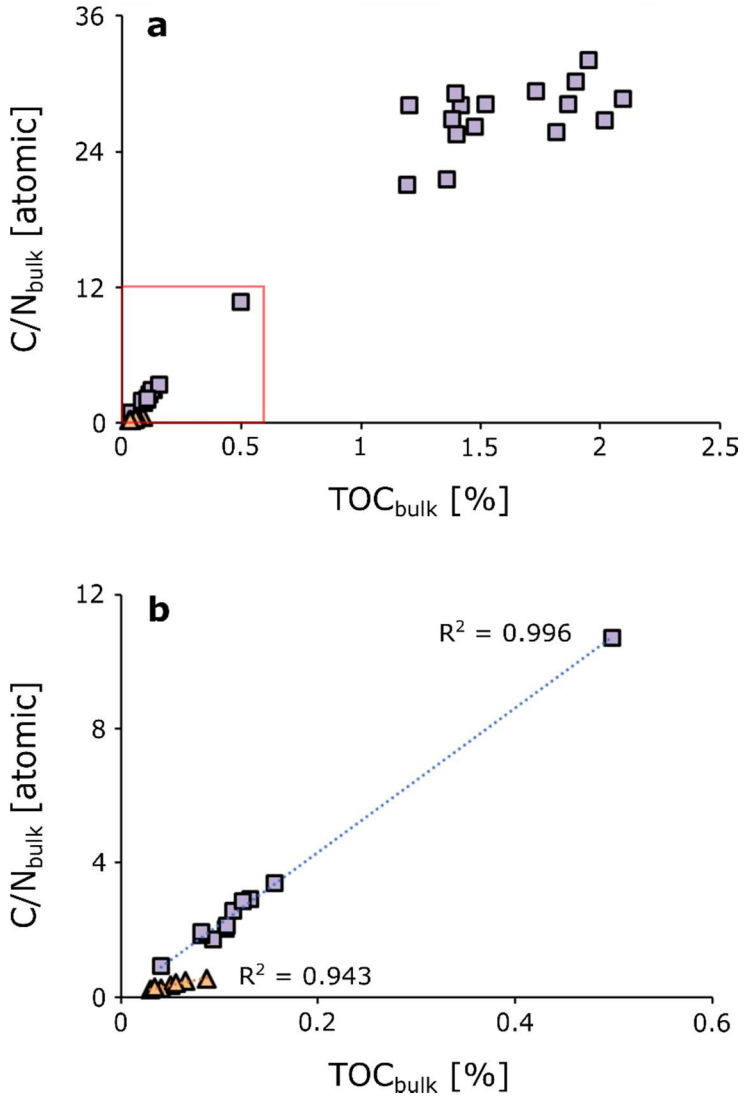

Figure 0.13**. Relationship between bulk C_{org}/N ratios and total organic carbon abundances for shales and bentonites (a) through the sampled Dob's Linn section and (b) zoomed in on shales from the Upper Hartfell Shale.** Bentonites in (b) are from all parts of the section. Symbols are as in Figure 5.1 of the main text.

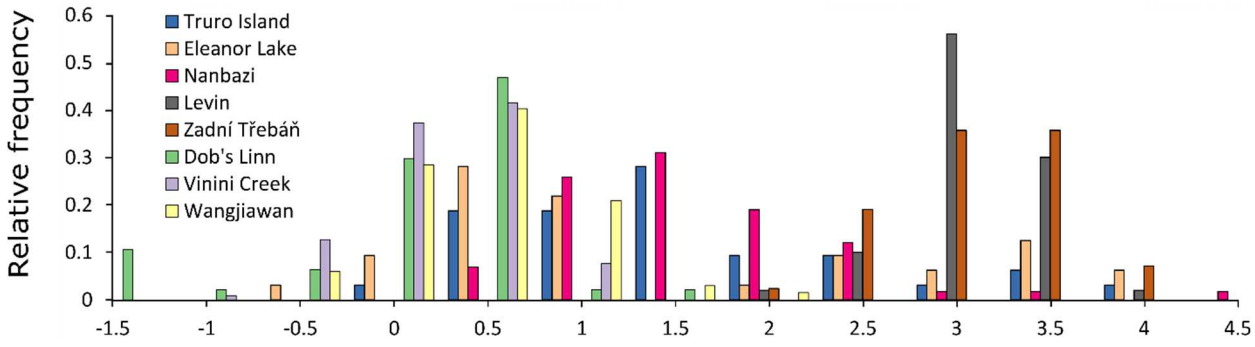

Figure 0.14**. Histogram of $\delta^{15}N$ values across the O-S boundary.** Notice how data from shallower depositional environments are on-average more positive, regardless of latitude.